Numerical and experimental analysis of Wetumpka impact crater, Alabama.

by

Leticia Pacetta De Marchi

A dissertation submitted to the Graduate Faculty of
Auburn University
in partial fulfillment of the
requirements for the Degree of
Doctor of Philosophy

Auburn, Alabama
August 7, 2021

Keywords: Impact cratering, numerical simulation, modeling, hydrocode, Wetumpka, marine-target impacts

Approved by

Vinamra Agrawal, Chair, Associate Professor of Aerospace Engineering
David T. King Jr, Chair, Professor of Geology
Willis E. Hames, Professor of Geology
Jens Ormö, Research Scientist

Abstract

Impacts are the most crucial process in the formation of the solar system, since planets and other bodies are considered to have formed by accretion of small objects through collisional processes. By studying craters on Earth, we can have a better understanding on how this process works on other planetary surfaces and thus improve our knowledge on the formation of our solar system. The process of impact cratering in marine target settings, which is the focus of this project, has been a topic of significant interest because of its connections to ancient oceans on other planetary bodies such as Mars. The Wetumpka impact crater, located in central Alabama, is a good candidate for this study, since it was formed in a shallow sea environment, approximately 85 million years ago, during the late Cretaceous. The impact structure has been studied previously through field studies and core drilling. This study is built on the field and drill-core studies and performed hydrocode modeling using iSALE-2D to analyze the transient crater evolution and crater filling sequence with emphasis on the collapsed, southern, seaward section of the rim because that part of the rim is considered to have had the greatest influence on the crater fill sequence. With the intention to acquire experimentally based values for material input parameters, especially in the crystalline rim terrain, we collected, prepared, and submitted samples from that terrain for tensile and compressive tests, which used to estimate values of cohesion and friction angle. These values were included in the iSALE-2D damage model for simulations with different water depth, impact velocity and sediment thickness scenarios. The best fit model considers the impactor as a granitic sphere of 400m in diameter traveling at 12km/sec, striking a three-layered target: a) crystalline basement; b) 200 meters of sediments, and c) the uppermost sea water layer with 62.5 m of depth. Modeling results confirm field observations in relation to crater dimensions.

The crater filling sequence predicted by iSALE-2D matches the drill-core observations. Finally, the pressures predicted by iSALE-2D are consistent with shock petrography observations.

Acknowledgments

I would like to thank my two advisors Dr. King and Dr. Agrawal, for their guidance through my Ph.D. program and for the opportunity to be part of this project. I am really grateful for all things that I have learned from both of you, not just about science but all aspects of being part of an academic project. Thanks for the patience and for providing me everything I needed to do my research. I am also very grateful for the exceptional support when going through personal challenges, especially being far away from home. Both of you were the base for my performance and made me feel confident, encouraging me to keep going. Special thanks to Dr. King's wife, Lucille, for her caring touch (and best food ever!) and for making me feel I have a second family here. I also want to acknowledge all my committee members. Dr. Ormö, for his endless support in acquiring, reviewing, and interpreting data since the beginning of this project. Dr. Hames for his valuable reviews, feedback, and pleasant discussions throughout my time at AU. Also, Dr. Medina, a former committee member, for his help with literature review and for inspiring everyone with his passionate way of seeing science. I feel lucky for the opportunity to work and learn with you all. Thanks to all colleagues, staff, and faculty members from both Geosciences and Aerospace Engineering departments. Thanks to all the special people I found in Auburn and now are part of my foreign family. Also, thanks to friends back home for, even physically far away, staying close. I am grateful for the support from all collaborators, faculty members, and funding sources that made this project possible: Dr. Brian Anderson from Civil Engineering for helping with technical equipment and for being my outside reader; Dr. Asha-Dee Celestine, from Aerospace Engineering, for her help and monitoring during experiments; Rob Crosby, from the civil engineering concrete materials laboratory, for his help on preparing all rock samples; landowners at Wetumpka for their kind consideration in granting access to their private properties; Auburn University Intramural

Grants Program for iSALE digital modeling; Auburn University's Hopper high performance computing cluster; and all financial support, through travel and research grants, from internal and external sources (Geosciences department, COSAM, Lunar & Planetary Institute, NASA Astrobiology, and Meteoritical Society).

Finally, I dedicate this work to my loved family. Even thousands of miles away, and facing their own challenges, they always made sure I felt loved and supported, encouraging me to follow my dreams.

Thanks!

"The first sign of ignorance is assuming we know."

Baltasar Gracián

Table of Contents

List of Tables

List of Figures

List of Abbreviations

ASTM	American Society for Testing and Materials

Chapter 1. Introduction

Cosmic impacts

The impact of extraterrestrial objects on Earth, which was not considered a significant field of study until the 1960s, has been recognized as a major factor in the formation and evolution of the Earth, from both a geological and biological perspective (Melosh, 1989; Marvin, 1990; Grieve, 1991; Grieve and Shoemaker, 1994; French, 1998; Marvin, 1999; Grieve, 2001; Reimold, 2003; French, 2004; Reimold and Koeberl, 2008, French and Koeberl, 2010). Impacts were responsible for at least one great mass extinction, produced large volumes of melt and fragmental rocks, created crustal disturbances, and sometimes generated important ore deposits (French, 1998). Impacts can be 'game-changers,' for example, the great Chicxulub impact (Hildebrand et al., 1991), around 66 million years ago, was responsible for re-defining the course of biological evolution on the Earth. And a large impact between a Mars-sized object and the Earth, around 4.5 billion years ago, is now thought to have generated the accretionary formation of the Moon. Moreover, impacts can also generate economic products, for instance within the Sudbury impact crater, there are the largest nickel-copper sulfides deposits on Earth, and within the Red Wing Creek structure (Koeberl et al., 1996), there are significant traps for oil and gas. Further, the Popigai impact structure is known for its diamond deposits, which formed from the high pressure produced by the impact (Masaitis, 1998).

From a planetary perspective, the study of impact cratering on the Earth's surface provides a better understanding of solar system formation because planets and other solid bodies are considered to have formed by the accretion of small objects through collisional processes. Spatial exploration revealed that craters are a very common feature in our solar system, evidencing that

most solid bodies had their surface features strongly shaped by impacts and evolved with the contribution of external mass and chemical elements, including chemical building blocks necessary for life. Impact craters are the most common landform on our Moon, and on Mercury, Venus, and Mars, plus the moons of the gas-giant planets, and even on the surfaces of minor asteroids (Bottke et al., 2020; French, 1998; Melosh, 1992). Therefore, impacts are considered one of the most fundamental processes in the Solar System, being responsible for the formation and evolution of all solid planetary surfaces. Impacts produce craters of different sizes and complexity, which can be studied by remote sensing in all terrestrial planets and moons and by direct in situ observations on the Earth (Pierazzo and Collins, 2004).

The growth of the impact science in the last decades has improved the ability to identify impact structures by the presence of unique evidence, such as shock-metamorphic effects and exclusive geochemistry and petrology (French and Koeberl, 2010). Until now, there are approximately 190 confirmed impact structures on Earth (Earth Impact Database, 2021). These craters range from small circular features, such as Meteor crater in Arizona (Hoyt, 1987), to hundreds of kilometers in diameter, such as Vredefort crater, in South Africa, which is also the oldest impact structure on Earth, dating from approximately 2 billion years (Gibson et al., 1997). It is thought that several hundred more structures remain to be revealed (Kenkmann et al, 2014).

Formation of impact craters

Impact craters are formed by hypervelocity objects capable of penetrating the Earth's atmosphere and striking the ground at cosmic velocities. The crater formation starts at the moment that the cosmic object strikes the target rocks, releasing an enormous amount of kinetic energy as shock waves, which are formed at the impact contact point and radiate in an outward movement through the target rocks. These waves are powerful high-pressure stress waves that are not

produced by conventional geological processes. The formation process of a crater is divided into three different stages: (1) contact/compression, (2) excavation, and (3) modification stage. (Melosh, 1992; French, 1998; French and Koeberl, 2010) (Fig. 1.1).

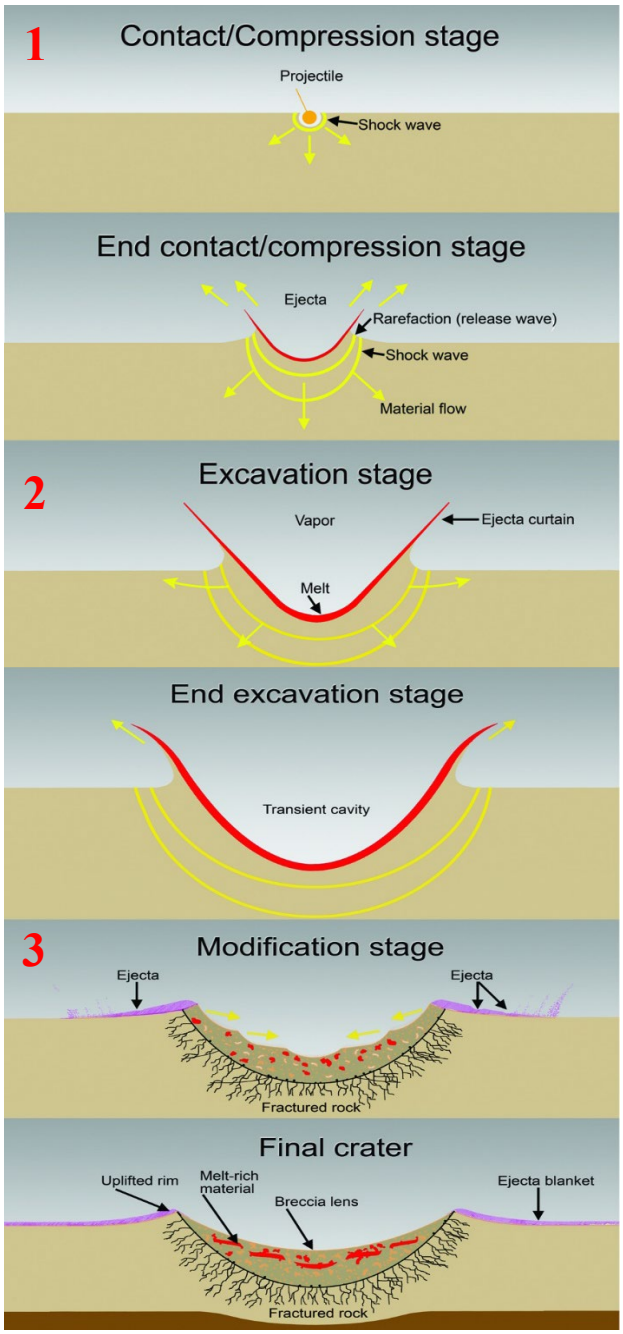

Figure 1.1. Impact crater formation stages. Modified from www.lpi.usra.edu (Bevan M. French\David A. Kring\ LPI\UA)

The contact/compression stage (1) starts at the moment that the projectile touches the surface. In this brief stage, the projectile's energy and momentum are transferred to the ground surface in a period of time that can be calculated in terms of the impactor diameter and its velocity (t ~ diameter/velocity). The projectile may penetrate the target at a depth no larger than 1-2 times its diameter. Right after initial contact, both objects are compressed, generating strong shock waves. Part of the shock waves are transmitted outward from the impact point, and part is reflected into the impactor object. As the shock waves travel through target rocks, they lose energy quickly through heating, deformation, and acceleration. Also, the increasing radial distance results in an increasing hemispherical area of interaction with the front shock, thus reducing the overall energy density. Close to the eventual crater rim, the velocity of shock waves drops to sound speed, and they become regular elastic waves. The wave's strength can be calculated by Hugoniot equation, which relates quantities in front shock to quantities behind the shock. At the impact point, high peak pressures may exceed 100 GPa, producing a large volume of melt and, in some cases, vaporization of the target rocks. Pressures may drop to 10-50 GPa further outward, over many kilometers from the impact point, but still producing shock-deformation effects. The shock waves that are reflected into the projectile eventually reach the back end of the body and then are reflected forward as tensional waves (release waves), which unload the impactor from high shock pressures. This process causes melting and vaporization of the projectile. When these release waves reach the front of the projectile, at the projectile-surface interface, it is the end of the contact compression stage. However, release waves continue to propagate into the target, decompressing it as well.

The excavation stage (2) is characterized by the opening of the crater by complex interactions between the ground surface and the expanding shock waves. Although this stage is a little longer than the compression stage, it is also a brief stage. Duration can be calculated in terms

of diameter and gravity ($t \sim (D/g)^{0.5}$). High pressures from the previous stage are uniform over a volume similar to impactor dimensions, a region called isobaric core. Within this region, the target material experiences high pressures followed by a pressure release, which causes fracturing and shattering. Upon release, the material has a "residual velocity" that is 1/5 of velocity under high pressure (because of thermodynamic irreversibility in the shock compression) and will produce an excavation flow around the center of the developing structure. The excavation flow varies depending on the location in the developing crater. In the upper levels, excavation flow is dominantly outward and upward, excavating and ejecting target rocks, and, at lower levels, the flow is downward and outward, forming a displaced zone. Since excavation flow cuts across contour lines of high peak pressures, the material ejected may contain a wide range of shock levels. The early ejecta, which has greater velocities and lands farther to the crater, contains a higher proportion of highly shocked material. The expansion of the transient cavity is linked with the uplift of near-surface rocks that will form the eventual crater rims. The transient crater keeps expanding until shock waves are lower in energy and, consequently, unable to excavate or displace rock. At this point, the transient crater reaches its maximum size, with a diameter roughly 3 to 4 times the depth, the excavation stage ends, and the modification stage starts instantly. Transient crater dimensions can be affected by the angle of impact, presence of water table, layered target material with different strengths, rock structures, and original topography.

In the modification stage (3), the shock waves were now transformed into regular elastic waves beyond the crater rim and are no longer significant in the crater development. The main factors during the modification stage are gravity and rock mechanics. Rock debris that was moving upward and outward during the excavation stage comes to a momentary pause, then starts to move back into the center of the crater due to gravity. In small transient craters ($< \sim 4$km), the material

falls back, and the steep rim collapses onto the crater's floor. This collapse increases the crater's diameter by about 15%. Breccia lenses, which often include highly shocked materials, are formed in the structure's interior with a thickness of about half of crater depth. The final diameter is about five times greater than depth. In larger transient craters (> ~ 4km), the floor rises (controlled by viscosity of target material), the central peak emerges (or peak rings on even larger structures), and rims sink along faults forming steep terraces. The floor is usually overlain by a layer of highly shocked impact melt and breccia deposit. The end of the modification stage is not clear since these processes of collapse and uplift are slowly followed by conventional geological processes, such as mass movement, isostatic uplift, erosion, sedimentation, burial, and tectonic deformation.

Diagnostic evidence

The geological features that are developed by hypervelocity meteorite impact are, most of the time, not unique. Features such as circular form, circular pattern of deformation, fracturing and brecciation, geophysical anomalies (especially gravity and magnetics), large units of igneous rock may also be formed by conventional geological processes, including tectonics, salt-dome deformation, volcanic activity, and endogenic igneous activity (French and Koeberl, 2010). However, some features are formed exclusively by impacts (French and Koeberl, 2010). The confirmation of impact events is based on unique shock metamorphic effects produced by the interaction between the target rocks and shock waves, thus unique to impact craters. Deformation features that are diagnostic for impact structures are (1) traces of impactor projectile, (2) shatter cones, (3) high-pressure glasses, (4) high-pressure mineral phases, and (5) planar micro-deformation features (French, 1998; French and Koeberl, 2010).

Although preserved meteorite fragments, included in item (1) above, can be powerful evidence, the impactor tends to be completely melted or vaporized because of the enormous shock

pressures. For this reason, the existence of projectile fragments is extremely rare (Melosh, 1989; Schnabel et al., 1999; Maier et al., 2006). However, measurable amounts of melted and vaporized projectile (<1%) are usually incorporated into breccias and melt rocks during crater formation, including ejecta material. Distinct chemical and isotopic signatures, also included in item (1) above, can identify projectile elements in impactites. Detection of extraterrestrial mass is based on the analysis of elements known to be abundant in meteorites relative to typical terrestrial crustal rocks. These elements are siderophiles elements such as Ni, Co, Cr, Au, and the Platinum group elements (Ru, Rh, Pd, Os, Ir, and Pt). Iridium (Ir) analysis has been effectively used as evidence of impact origin. Besides the analysis of elemental abundances, isotopic ratios of Os can also be used since its ratio is distinctively different in meteorites and terrestrial rocks. These chemical analyses must be compared with target rocks in order to affirm any extraterrestrial contribution. If the analysis is being made on ejected material, the comparison should be made with adjacent rock formations (Koeberl, 1998; Tagle and Hecht, 2006; Koeberl, 2007).

Shatter cones (2) are formed by penetrative fractures, forming striated conical features usually formed in low shock pressures (< 10 GPa) (Dietz, 1959, 1963a and b, 1968; Milton, 1977). They can form in large volumes of target rock, playing an essential role in identifying impact craters (Howard and Offield, 1968; Hargraves et al., 1990; Fackelman et al., 2008). Shatter cones are formed in all rock types but are better developed in fine grained rocks such as limestones and dolostones (Dietz, 1963a,b, 1968).

High-pressure glasses (3), also called diaplectic glasses, are minerals that are converted into amorphous phases (glassy) under high pressures (>30–50 GPa). They typically keep the original shape of the mineral, not showing disruption or flow. Common types are diaplectic glasses from feldspar (maskelynite) and quartz (Engelhardt and Stöffler, 1968; Bunch et al., 1967, 1968;

Dvorak, 1969; Arndt et al., 1982). Target rock minerals convert to new phases (4) that are stable under high pressure conditions, such as coesite and stishovite, which are SiO_2 polymorphs, or diamond, which is a carbon polymorph. These minerals are common in lower crust and mantle, where the pressure is naturally high, thus, geologic context must be taken into account (Chao et al., 1960; Shoemaker and Chao, 1961; Chao; Stähle et al., 2008; Kieffer, 1971).

Planar micro-deformation features in quartz grains, such as PFs (planar fractures), PFDs (planar deformation features), and FFs (feather features) are commonly used for identification of impact structures. PFs are sets of multiple parallel open planar fractures whereas PDFs are thinner, closely-spaced planes (Kieffer, 1971; Stöffler and Langenhorst, 1994; French et al., 1997, 2004). PDFs are, in fact, the shock effect that is most used for confirmation of impact structures (Stöffler and Langenhorst, 1994; Grieve et al., 1996). FFs are smaller, subparallel closed planes of fluid inclusions that diverge from PFs, and may represent the development of PDFs at relatively low shock pressures (French et al., 2004; Ferrière and Osinski, 2009; Poelchau and Kenkmann, 2009). PDFs planes are oriented at specific angles to the c-axis of the host quartz, being parallel to only a few specific crystallographic planes, frequently with low Miller-Bravais indices such as c(0001), ω{10$\bar{1}$3}, and π{10$\bar{1}$2}. In a histogram plot showing frequency of PDFs orientation, the concentration at specific values are characteristic of certain pressure intervals. (Bunch, 1968; French, 1998; French et al., 2004).

Numerical modeling of impact cratering

The geology and morphology of a crater may give information about the impactor and target properties and can lead to the amount of energy released during the impact. It is possible to reproduce crater analogues by small-scale laboratory experiments, but processes such as melting and vaporization cannot be easily reproduced since they require a huge amount of temperature and

pressure to occur. Also, laboratory experiments are executed under Earth's gravity and may limit results to other planetary surfaces. However, different physical and chemical conditions can be simulated by computer simulations, which have been a fundamental tool in understanding cratering processes, along with remote sensing, laboratory experiments, and geological surveys. They create a controlled environment with a detailed spatial and temporal resolution (Pierazzo, 2006). In order to create a computer simulation, it is necessary to have a good understanding of physics and chemistry involved in the cratering process, as well as enough computer power (Pierazzo and Collins, 2004).

Hydrocodes are computer programs that may be used to simulate (numerically) dynamic events, particularly those that include shock. The continuum dynamics of impact cratering and solid-state deformation are implemented in the hydrocode in the form of equations for movement, thermodynamics, and target strength (Anderson, 1987). Movement equations are mainly based on Classical Newtonian Mechanics, and the responses of different materials to shock are based on thermodynamic equations of state. It is important to consider that all material's strength is influenced by target properties such as heterogeneity, porosity, layering, and these can affect the amount of melting and ejecta material, as well as crater morphology. The response of materials to stress is defined by specific properties, which will define the different material's behavior under the same amount of stress (specific properties are provided through a series of parameters). Changes in density and internal energy are critical to early cratering stages and are described by equations of state (EOS), and the relation between stress and strain is given by constitutive equations, which is relevant for late cratering stages (Pierazzo, 2006).

According to Pierazzo and Collins (2004), in the process of implementation of the continuum dynamics of cratering into numerical codes, the time and space are divided into discrete

blocks, or cells. The resolution of a simulation is based on the number of cells used (mesh size), which may vary and is limited by the computer physical memory and amount of time available for computation. The choice of temporal and spatial resolution in modelling an impact event is important to understand and detail all variations in space and time but a high-resolution simulation can be limited by the available time and computer power. The resolution can be chosen depending on the situation and on what is relevant to fill the gaps in the knowledge of certain event. For example, to model a 100km-wide crater with a 100 meter resolution it might be difficult to distinguish meter scale features, but it can be observed in the field by a geologist. But, at the same time, a temporal resolution of 10-3 seconds, can be considered low and not enough if one wants to access the development and propagation of shock waves in the target and impactor. Some simulations can take months to be completed and the computer storage needed is directly dependent on time steps required, cell size and number of parameters set. The use of inadequate mesh resolutions can hamper the simulation results as exemplified by Pierazzo (2001), where the melt/vaporization volumes can be declined by progressively lower resolutions, underestimating the maximum shock pressure.

Advantages and limitations of hydrocode simulations

Numerical modeling of impact cratering may be considered a powerful tool in that it can provide detailed information regarding all the variables of interest, setting parameters to represent several different environments. It describes all the crater formation stages (contact/compression, excavation, and modification), as well as production of melting/vaporization volume, crater collapse, and launch and deposition of ejecta. Simulations can be validated by testing against geological observations and laboratory experiments, and all three approaches complete gaps not explained by only one of them. Another good aspect of hydrocode simulations is that it can be

separated in different codes to focus on early or late stages of crater formation, what can be helpful to aim the objective of the research without long times of computing data.

As any other approach, such as geological observation and laboratory experiments, numerical modeling has its own limitations, including spatial and temporal resolution and computer hardware. It cannot simulate processes or features that are smaller than the minimum cell size, nor processes that have not been implemented in the code. That is why it is required a good understanding of the physics and chemistry in the process. It is important that numerical modeling is performed along with geological observations and laboratory experiments in order to acquire a more realistic interpretation. The geological observations and experiments will help to set parameters into the code, such as material strength and impactor size.

Marine-target craters

Although oceans cover 70% of the Earth's surface, impact craters formed in marine targets represent only approximately 20% of the Earth's impact record. The lack of documented marine craters is due to the water layer inhibiting and altering the cratering process and the continuous recycling of the oceanic crust through geological time (Davison and Collins, 2007. Examples of marine target craters are Chesapeake Bay, Lockne, Wetumpka, Flynn Creek, and Tvrären. Marine-target craters may experience a rapid coverage by sediments, depending on the water depth, surviving erosion and being among the best-preserved structures on Earth. Morphological features of marine-target craters depend on the influence of the target in the cratering process, but they are usually characterized by deposits and radial gullies formed by the resurge of the sea. Other planetary surfaces with similar target environments will develop similar features that may be identified by satellite imagery and are connected to ancient water bodies. Martian craters, such as Hellas Planitia and Argyre Planitia, show geomorphic evidence of ancient marine and lacustrine

environments, as well as several smaller craters, supporting the theory that large water bodies occupied the northern plains of Mars.

The formation of marine-target impact craters is governed by the same three stages mentioned above (contact/compression, excavation, and modification), but some differences are noted regarding the water layer. In the contact compression stage, the process is similar to dry-target crater formation, where a large amount of kinetic energy is released as shock waves. The projectile is also, most of the time, completely vaporized and melted by the release of pressure, as explained above. During the excavation stage, the water layer is excavated along with the target rocks and ejected as a curtain. Outward moving tsunami waves are formed. This wave can carry shocked material and seafloor sediments through long distances. During the modification stage, the crater collapse is accompanied by the return of the seawater. This process brings ejecta material and seafloor sediments back into the crater, forming resurge deposits. If the water depth is greater than rim, the final structure is entirely covered by water. Great water depths lead to deep ocean sedimentation that will cover the crater with fine-grained sediments, promoting the preservation of the structure (Ormö and Lindström, 2000; Ormö et al., 2002; 2007; 2009).

Hydrocode simulations for marine-target craters

Marine-target craters are characterized by unique features such as resurge sedimentation, which contain substantial material transported back into the crater by the resurge of displaced water masses moving back towards the center of the crater (Ormö et al. 2007, 2009). The process of marine impact cratering has been a topic of significant interest because of its connections with geological and biotic evolution of Earth, and to ancient oceans on other planetary bodies such as Mars and Europa. Numerical modeling studies have been used to understand the role of the layer of water in the upper part of the target, particularly regarding water depth. By doing this kind of

study on marine-target craters on Earth we can assess water depth of paleo-oceans in other planetary surfaces, such as Mars (Ormö et al., 2002). Ormö et al. (2002) used hydrocode simulations to complement facies analysis of Lockne crater filling sediments in order to estimate the water depth at the time of the impact. The main objective of this study was to link differences in morphology to the target water depth. To do it, the authors simulated different water depth scenarios to compare with geological observations, and then identify an acceptable depth range for the impact. Numerical modeling results indicate a minimum water depth that is capable to pass the elevated rim of the crater, being able to form resurge deposits within the impact structure, which is observed in Lockne geology. Simulations also show that, there is maximum limit of water depth to form a rim with an overturned flap, which is also observed at Lockne. Thus, by linking what is directly observed in the crater geology with numerical modeling it was possible to set a reliable range of water depth for the impact. Similar studies focused on comparing geological data to numerical models, and estimate water depth, were also carried out by Shuvalov and Trubestkaya (2002).

Aim of study

This study aims to better understand marine-target impact structures from a numerical perspective, experimental and field studies, with focus on Wetumpka crater, located in central Alabama, USA. The crater was formed in a shallow sea environment, approximately 85 million years ago, during the Late Cretaceous (King et al., 2002). Since Wetumpka crater has been extensively drilled and geologically characterized over the last 20 years, it can support validating numerical simulation results, which were acquired by using iSALE-2D. The main questions explored are the effects of impact speed, initial water depth, target layer thickness, and material properties on the final crater morphology and resulting tsunami formation, with focus on the

southern collapsed rim. Material models within iSALE-2D were augmented by experimental studies performed on samples gathered from inside and outside the crater. This study, combined with existing and new field-based geological observations, aims to fill the gaps in our knowledge of marine impact craters.

Chapter 2. Wetumpka impact crater

The Wetumpka impact structure is a marine-target crater located in central Alabama (King et al., 2002; 2006; 2015; King and Ormö, 2011) (Fig. 2.1). The impact occurred during Late Cretaceous (± 85 m.y.) in a shallow marine environment within the Gulf Coastal Plain (Wartho et al., 2012). The target region is comprised of crystalline rocks of the Piedmont metamorphic terrane, which was unconformably overlain by several tens of meters of poorly consolidated sediments, specifically the Upper Cretaceous Tuscaloosa Group and Eutaw Formation (Neathery et al., 1976; King et al., 2002). The water depth was estimated to have been approximately in the range of ~ 35 to 100 m based on target paleogeography (King et al., 2002; 2006).

The current crater is heavily eroded and exhibits rims composed of Appalachian Piedmont bedrock. It has an asymmetric nature due to the collapse of the southwest, ocean-facing section (King et al., 2006) (Fig. 2.1). The crater is, on average, 6.1 km in diameter. However, it reaches a maximum northeast-southwest distance of ~ 7.6 km, owing to the inclusion of an exterior disturbed terrain (King et al., 2002; King and Ormö, 2011). It is noteworthy that Wetumpka impact structure has no evident central uplift, despite having a diameter where such a feature is generally thought likely to develop (King and Ormö, 2011; King et al., 2015). Gravimeter-based mapping of residual Bouguer gravity appears to confirm that there is no clearly detectable central uplift at Wetumpka (Plescia, 2009; Robbins, 2011), maybe as a consequence of the layered target known to suppress the formation of central uplift (Hopkins et al., 2019).

Wetumpka is relatively well exposed, and its surficial geology consists of a deformed, semi-circular, crystalline-rim, and lower relief areas both in the crater interior and outside the rim

in a disturbed area on the southern side, which is composed of faulted and otherwise deformed sediments, plus limited areas of resurge mud-flow ("chalk") deposits (King and Ormö, 2011).

Wetumpka impact structure's crater-filling materials have been investigated during field campaigns (1997-date) and core-drilling campaigns (1998, 2006, and 2009), which are briefly summarized below. A geophysical (i.e., gravity) profile, which lends insights into the deeper part of the crater fill not observed in the field or by drilling, is also summarized below. The crater-filling materials, and their vertical sequence, informs us of the modification stage of crater formation and helps to validate numerical models of the Wetumpka impact event.

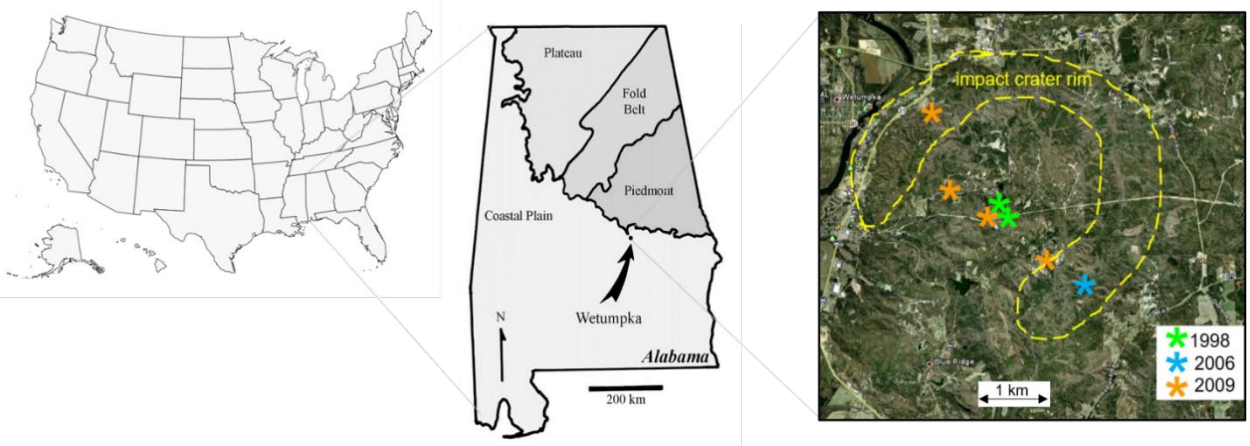

Figure 2.1. Location of Wetumpka crater and crater outline showing drill cores location (modified from King et al., 2015).

Wetumpka crater's geology

The current understanding of Wetumpka crater's geology is based on field observations and drill core studies. The Wetumpka crater's geology was initially mapped by Neathery et al. (1976), who first suggested a meteorite impact origin for the structure based on stratigraphic and structural evidence. The main observed features were (1) a circular rim comprised of metamorphic

rock and surrounded by Cretaceous sedimentary rocks, (2) chaotic orientation of sedimentary and metamorphic rock units in the center, (3) concentric marginal faulting, and (4) a radial pattern of the foliation structural dip, in an outward direction from the center of the structure, contrasting with the regional pattern, generally towards the east. Although Neathery et al. (1976) did not observe diagnostic impact features such as shatter cones, planar micro deformation features, projectile isotopic signature, or high-pressure mineral phase changes (criteria of French and Koeberl, 2010), his field observations altogether provided initial evidence of reorientation of rock units possibly caused by a cosmic impact.

The confirmation of an impact origin and a better understanding of the crater's formation arose with subsequent research at Auburn University (King et al., 2002; 2006; King and Ormö, 2011). At Auburn University, there were multiple graduate students' theses on Wetumpka (Nelson, 2000; Johnson, 2007; Tabares Rodenas, 2012; Rodesney, 2014; Markin, 2015; Heider, 2015; Chinchalkar, 2019), that contributed to our current understanding of Wetumpka crater's geology.

In 1998, two core holes were drilled near to the center of the structure to a depth of ~ 190 m (King et al., 2002; Johnson, 2007) (green stars on Fig. 2.1), evidencing part of the basin-filling sequence, which was initially interpreted as polymitic breccias overlaid by resurge deposits. Microscopic analysis of the polymitic breccia matrix revealed shocked quartz showing planar deformation features (PDFs) with a concentration of approximately 10 grains/cm^3, supporting the impact origin (King et al., 2002). The orientation of PDFs related to c-axis of host quartz grain, specifically the angle between c-axis poles to PDF, is diagnostic of certain pressure intervals (French, 1998), and quartz grains from the Wetumpka impact structure have shown evidence of shock pressures that may be estimated to be as high as 20 GPa (discussed below). In addition to planar deformation features, geochemical analysis of two powdered samples from the polymitic

breccia revealed elevated contents of Ir, Co, Ni, and Cr (King et al., 2002), known to be standard meteoritic components (Koeberl, 2014), suggesting an extraterrestrial contribution (King et al., 2002).

Building on the pioneering field-mapping work of Neathery et al. (1976), the results of modern field studies at Wetumpka impact structure, which began in 1997 and continue to present, include the delineation of three main impact-related terrains. These are the impact structure's crystalline rim, interior structure-filling, and exterior disturbed terrains (Fig. 2.2) (King et al., 2002; 2006; King and Ormö, 2011). The crystalline rim terrain is an asymmetrical feature that spans approximately 270 degrees of an arc open on the southwestern quadrant, displaying a horseshoe-shaped outline (Fig. 2.2). The width of the impact structure rim is not the same all around, but in an NW-SE direction, the rims outcrops reflect a crater diameter of 6.1 km. However, the structural diameter, limited by faults in the exterior terrain, reflects approximately 7.6 km (Szabo et al., 1998). The orientation of constituent foliation within the rim ranges from a westerly dip on the west side to a near-vertical dip on the eastern side. The interior structure-filling unit consists of broken sedimentary formations, which is a term that is intended to mean that the formations have been intensively deformed and fragmented but still recognizable as their origin (Nelson, 2000; King et al., 2006; King and Ormö, 2011). The exterior disturbed terrain, which comprises a limited area adjacent to and directly outside the southwestern open quadrant of the structure's crystalline rim, consists of target formations that are part of large slump blocks that appear to have rotated and moved a short distance toward the crater interior (King et al., 2006). In this regard, Wetumpka's exterior disturbed terrain appears to mimic part of the "annular trough," an extensively slumped feature surrounding the excavated crater in the Chesapeake Bay impact structure (King and Ormö, 2011; King et al., 2015). There is also an external zone of horst and

graben structures striking tangential to the crater and located adjacent to the missing rim section, suggesting tensional stress caused by the southern rim collapse (King et al., 2002; King et al., 2006).

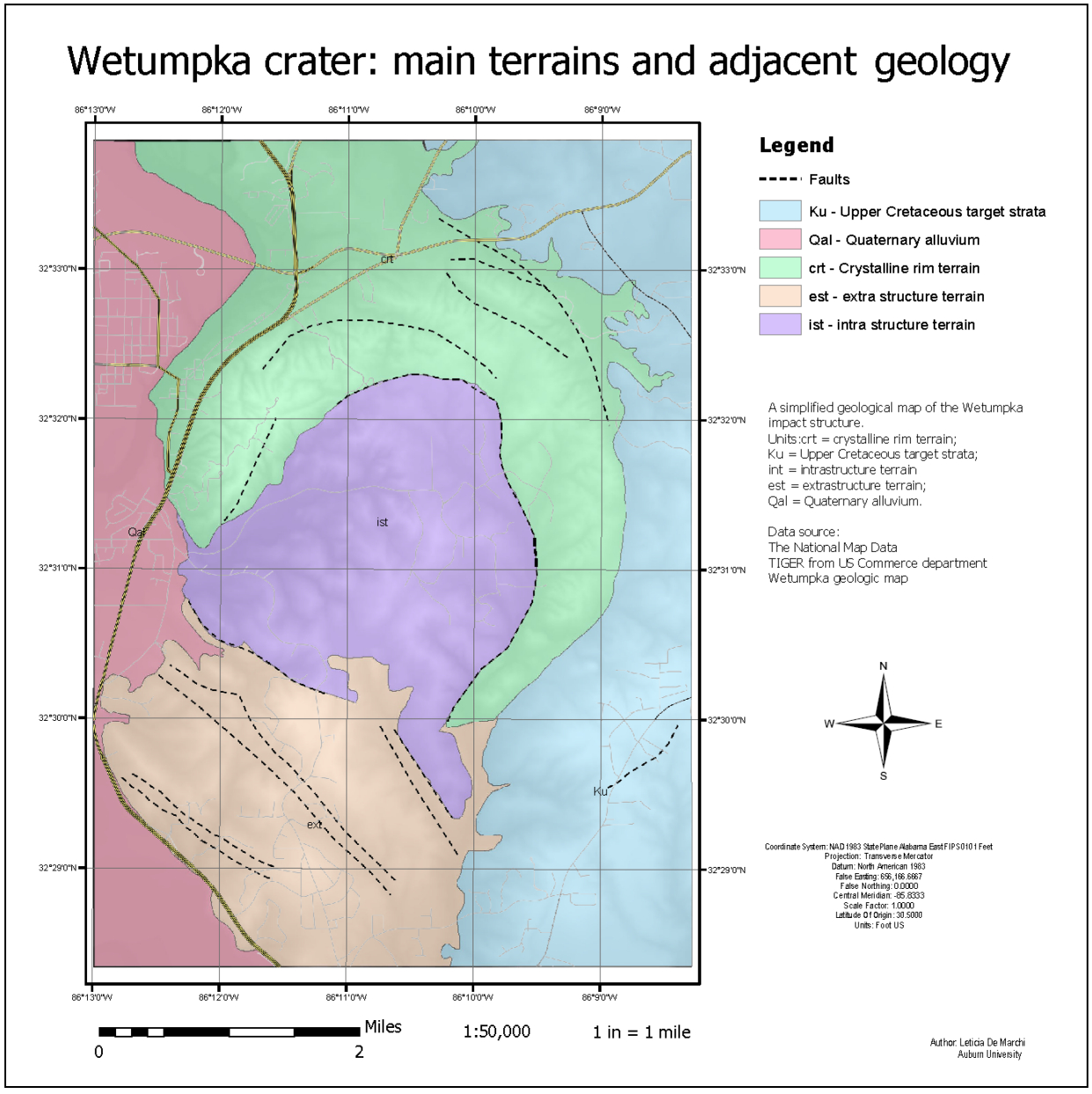

Figure 2.2. Impact-related main terrains and adjacent terrains of Wetumpka crater. LiDAR-based DEM with digitized geologic map from Neathery et al. 1976.

Core drilling

The drilling campaigns, realized in 1998, 2006, and 2009, produced a total of seven core holes located in different parts of the crater, spread along an NW-SE direction (Fig. 2.1), and at different depths, providing a better understanding of the interior structure-filling units, which have several distinctive stratigraphic components. In apparent order of formation during impact, these components are the impactite sands, trans-crater slide unit, crystalline boulder-bearing bed, and resurge chalk deposits. Impactite sands are monomict clastic sediments that contain sedimentary target blocks; whereas the trans-crater slide unit has folded and sometimes inverted stratigraphy of target units, and its origin is related to the failure of the southern rim (King et al., 2006; King and Ormö, 2011). The crystalline boulder-bearing unit consists of a pebble and cobble-rich sandy matrix that contains shocked proximal ejecta and a noteworthy component of crystalline target boulders (mainly schists and gneisses) that range up to 45 m in apparent diameter (King et al., 2006; 2015). Resurge chalks are resedimented beds of Mooreville Chalk that contain fine ejecta components (Petruny and King, 2018), as well as evidence of long-distance transport from the adjacent, coeval shelfal area of central Alabama (suggesting a turn-around of the original rim-wave tsunami). All these various interior-filling components comprise the upper few tens of meters of the Wetumpka impact structure's interior structure-filling materials. Drill cores from crater fill sediments attained a maximum depth of 218 m, penetrating through sediments from Tuscaloosa Group and Eutaw Formation, and reaching the lower impactite sand unit (King & Ormö, 2011).

Figure 2.3 shows a schematic cross-section of the Wetumpka crater and the location of all core drillings. Both drill cores from 1998 (AU scientific core holes #98-01 and #98-02), when viewed together, define the following sequence: (1) the lower ~ 60 m of the drill cores is comprised of impactite sands with sedimentary target megablocks; (2) the lower middle part (~ 40 m) is

comprised of crystalline target blocks and a subordinate amount of polymict impact breccia; and the upper middle part (~ 90 m) is comprised of sedimentary megablocks from broken sedimentary formations (specifically, the Tuscaloosa Group and Eutaw Formation) with very little impactite sand as matrix. Above this lies the upper part of the sequence (3), which is found in outcrop and consists of ~ 40 m of the trans-crater slide plus the overlying crystalline boulder-bearing bed that contains some polymict impact breccia.

The drill core from 2006 (AU scientific core hole #06-01 – blue star on Fig. 2.1) was bored into the eastern rim to a depth of ~ 30 m, showing that this location consists entirely of a highly weathered crystalline target (mainly micaceous schist). The 2009 drilling campaign consisted of drilling four core holes (orange starts on Fig. 2.1) of various depths ranging from ~ 30 to ~ 215 m (King and Ormö, 2011; and graduate student theses – Tabares Rodenas, 2012; Rodesney, 2014; Markin, 2015; Heider, 2015; Chinchalkar, 2019). One core was drilled in the northern crystalline rim (AU scientific core hole #09-01), and one was drilled in the southern crystalline boulder-bearing bed (~ 15 m) and a few meters into the underlying trans-crater slide unit (AU scientific core hole #09-02). The other two were drilled in the interior crater-filling terrain (AU scientific core holes #09-03 and #09-04). One of these drill cores (#09-03), located in the west part of the crater-fill, penetrated ~ 25 m of resurge chalk and ~ 70 m of sedimentary megablocks from broken sedimentary formations (specifically, the Eutaw Formation) with very little impactite sand as matrix. The other drill core (#09-04), located closer to the crater center, penetrated trans-crater slide unit (~ 75 m) and ~ 150 m of impactite sand with sedimentary target megablocks.

In taking stock of this brief review of Wetumpka core drilling, it is worthy to note that the five drill cores that penetrate the crater-filling terrain are nearly all comprised of material of sedimentary target origin. By sedimentary target origin, we mean that the drill core is composed

either of (1) impactite sands or (2) sedimentary target megablocks with minimal sandy matrix. Crystalline materials occur in only two places in the drilled sequence, (1) the lower middle, ~ 40 m section within the central drill cores that contains crystalline target blocks and polymict impact breccia and (2) the surficial crystalline boulder-bearing bed.

Deeper crater filling materials

Outcrops and cores drilled so far reveal some details of the upper ~ 210 m of the Wetumpka crater-filling materials, yet the crater bowl of Wetumpka is likely to have as much as ~ 700 to ~ 1000 m of material within it, based on gravity modeling (Robbins et al., 2011 – Annex 7) and theoretical model estimates (King et al., 2006). The gravity model of the crater, along a west-east direction, produced a vertical profile of crater-filling materials that consists of a lower unit with a density equal to ~ 2.6 g/cm^3 (ranging from ~ 375 to ~ 750 m depth) and an upper unit with a density equal to ~ 2.1 g/cm^3. Drilling has not penetrated to the depth of the lower unit defined by gravity modeling, but based on impact crater's formative processes, it is likely that the lower unit of higher density is likely composed of crystalline bedrock slump blocks. The higher density suggests that, the lower unit contains a much higher proportion of crystalline blocks than the upper unit. In this gravity model, target crystalline bedrock is estimated to have a density of ~ 2.7 g/cm^3 (Robbins et al., 2011). Figure 2.3 shows the interpreted location of the boundary between the 2.1 and 2.6 g/cm^3 crater-filling units.

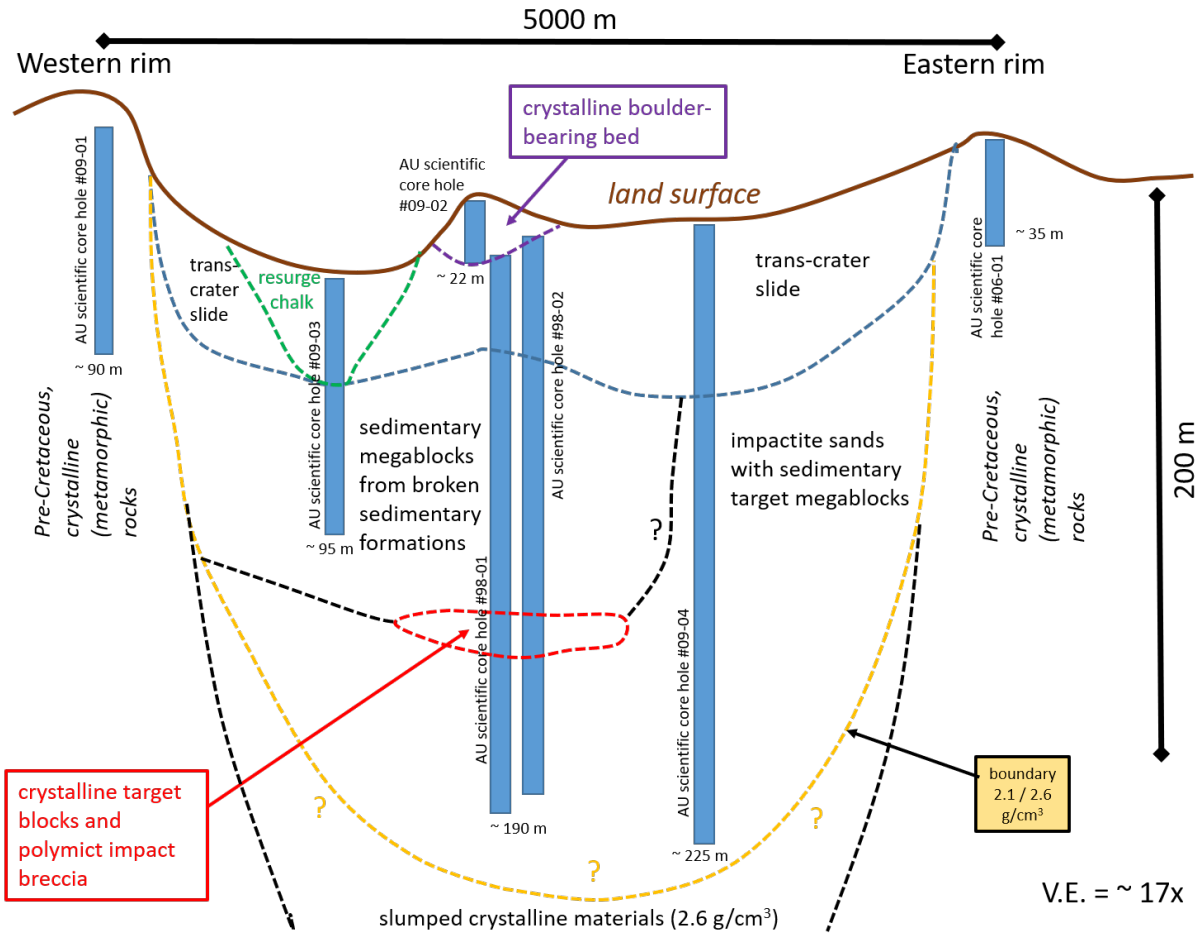

Figure 2.3. Schematic cross-section of Wetumpka impact structure showing the approximate land surface profile. The location of cores drilling in the impact structure (vertical blue lines labeled with the name AU scientific core hole #nn-xx and approximate total depth) and the approximate correlation between the upper crater-filling units as described in the text. Vertical exaggeration is approximately 17x. The approximate boundary between the upper crater-filling unit (2.1 g/cm3) and the underlying slumped crystalline materials (2.6 g/cm3), as discussed in the text, is shown as a dashed line with queries (?). This figure is a synthesis of research on core drilling, as noted in the text (De Marchi et al., 2021).

An estimated theoretical model cross-section, presented by King et al. (2006), shows the crater filling materials may be ~ 1 km thick. In this interpretation, the upper ~ 400 m of this ~ 1 km is likely displaced materials (i.e., slumped materials akin to the impactite sands, trans-crater slide, and crystalline boulder-bearing breccia noted above), and the lower ~ 600 m is the anticipated autochthonous breccia lens (i.e., slumped crystalline materials). These units, which

were defined before the gravity modeling of Robbins et al. (2011), likely correspond closely to the 2.1 and 2.6 g/cm^3 crater-filling units.

Shock pressures

Previous studies of impact-affect (i.e., Planar Fractures-PFs, Feather Features-FFs, and Planar Deformation Features-PDFs bearing) quartz grains from Wetumpka impact structure have shown evidence of shock pressures that may be estimated to be as high as 20 GPa, as explained below. Figure 2.4 is a composite histogram of published data on FF and PDF crystallographic directions from Wetumpka. Impact affected, or shocked, quartz grains occur mainly in two main locations within Wetumpka, one location is at about 100 m depth in the central drill cores where there is a layer of slumped, polymict breccia in the drill cores (King et al., 2002). This occurrence, which is rich in quartz bearing the common PDF plane $\{10\bar{1}3\}$ among others, suggests shock pressures of up to 20 GPa (in comparison with definitions presented by Ferrière et al., 2009). Because the impact-affected grains were largely sub-rounded, the suggested target materials were Upper Cretaceous sedimentary target, rather than the underlying crystalline (metamorphic) bedrock, which would more likely yield angular quartz grains (King et al., 2002). The second occurrence of impact-affected quartz grains is in the surficial polymict boulder-bearing breccia unit atop the trans-crater slide unit of the interior crater fill (King et al., 2015). These PF- and PDF-bearing quartz grains, which also are thought to have derived from Upper Cretaceous sedimentary target materials, include sand grains and pebbles. The pebbles and some sand grains also contain feather features (FFs), which are attendant to PFs and have a curvi-planar aspect (King et al., 2015). It is thought that these impact-related features are related to slightly lower shock pressures, perhaps in the 7 to 10 GPa range, and may represent materials from higher up in the sedimentary target zone (King et al., 2015). Planes $\{11\bar{2}2\}$ and $\{10\bar{1}1\}$ are most common in this

occurrence, and the $\{10\bar{1}3\}$ is apparently absent. However, the occurrence of the plane $\{10\bar{1}2\}$ and the wide distribution of shock-characteristic angles among impact-affected quartz grains from the boulder-bearing unit, suggests shock pressures may have been as much as 20 GPa (Ferrière et al., 2009; Ferrière and Osinski, 2013; Holm-Alwmark et al., 2018; Feignon et al., 2020).

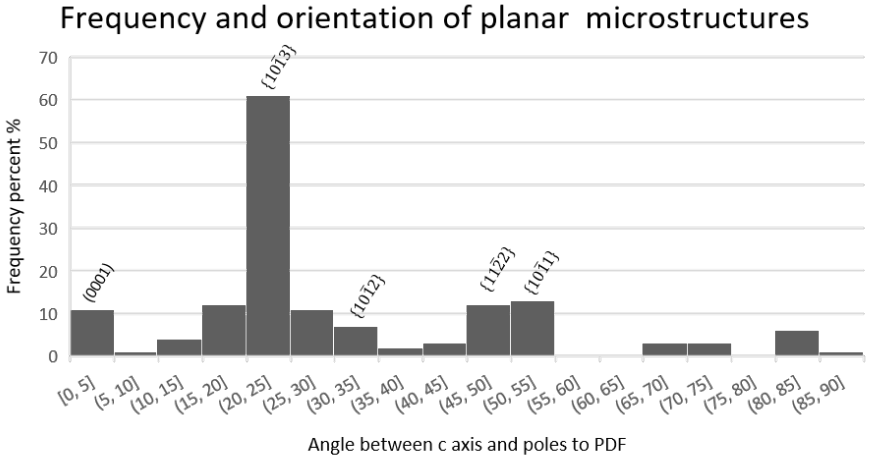

Angle between c axis and poles to feature	# of PDFs	# of FFs	Total	%	Frequency
0-5	5	6	11	7.3	common
5-10	1	0	1	0.7	rare
10-15	4	0	4	2.7	rare
15-20	12	0	12	8	common
20-25	59	2	61	40.7	abundant
25-30	11	0	11	7.3	common
30-35	3	4	7	4.7	rare
35-40	2	0	2	1.3	rare
40-45	3	0	3	2	rare
45-50	7	5	12	8	common
50-55	7	6	13	8.7	common
55-60	0	0	0	0	absent
60-65	0	0	0	0	absent
65-70	2	1	3	2	rare
70-75	2	1	3	2	rare
75-80	0	0	0	0	absent
80-85	2	4	6	4	rare
85-90	0	1	1	0.7	rare
Total	120	30	150	100	-

Frequency: rare <5%; common 5-15%; abundant >15%

Figure2.4. Frequency and preferred orientation of planar microstructures (PDF and FF) in shocked quartz from Wetumpka crater (King et al., 2002). Top: composite histogram of absolute frequency vs. orientation. Bottom: total number and percentage of microstructure

Chapter 3. Methodology

This study focuses on a numerical approach to the development of the Wetumpka crater, producing distinct models based on different input parameters such as target rocks properties or impact velocity. The models produce outputs for every 0.1 second of crater development, allowing a detailed view and assessment of all formation stages (contact/compression, excavation, and modification). A total of forty different simulations (annex 7) were performed, varying target thickness, material type and properties, and impact velocity. After an initial analysis, it was possible to filter possible scenarios based on fewer variables, focusing on the twelve most significant scenarios, varying sediment thickness, water depth, and impact speed (more details below, in section 3.2). Although default input parameters are provided in the code, these major twelve simulations were augmented by experimentally based values, specifically for the crystalline basement. For this, samples were collected, prepared, and submitted for split-Brazilian and uniaxial compressive tests as per ASTM standards (Figs. 3.1 and 3.2). Tests results allowed an estimation of cohesion and friction angle for the crystalline basement target layer, used as input parameters in the numerical simulations.

Experiments

The outcrop from where samples were collected is located on the crater's western rim, behind the First Community Bank of Central Alabama, by the Old US Highway 231 (Fig. 3.1, 3.2a, and 3.2b). Samples were then drilled and trimmed according to test requirements (Fig. 3.2c and Fig. 3.2d) at the Concrete Material Laboratory, at Auburn University Civil Engineering department. Both tests were performed by Instron 1321 servo-hydraulic test frame, 100 kN load

cell, at the Structures and Materials Lab, located at the Aerospace engineering department at Auburn University (Fig 3.2e).

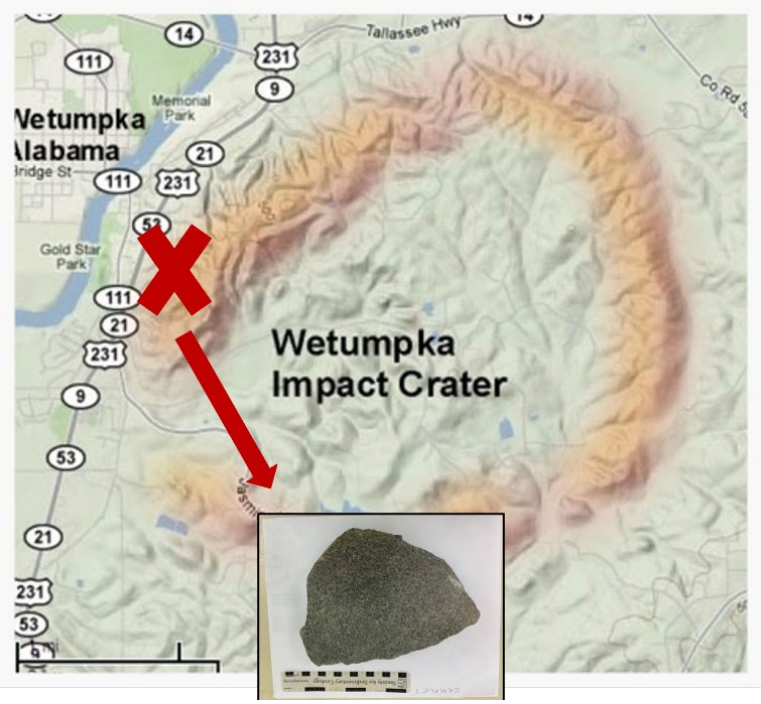

Figure3.1. Location of crystalline rim outcrop where samples were collected (adapted from www.wetumpkaimpactcratercommission.org

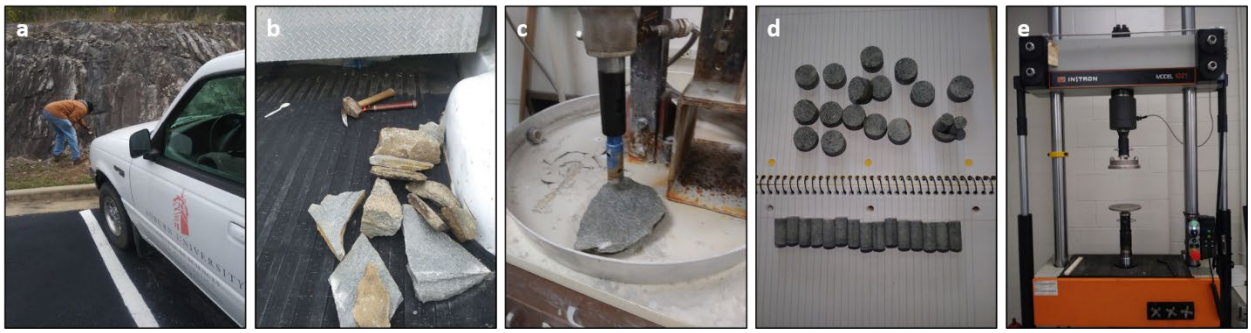

Figure 3.2. Sample collection (a and b) and preparation (c and d) for mechanical tests by Instron 1321 servo-hydraulic test frame (e)

Split-Brazilian tensile test

The tensile test (Fig 3.3a), also called split-Brazilian test, is a widely accepted indirect method to obtain the tensile strength of a material. In this test, a cylindrical specimen with thickness-to-diameter ratio of 1:2, is subjected to increasing compressive load, perpendicular to its axis, until it fails (ASTM D3967-08). The tensile strength is then calculated as:

$$\sigma_t = \frac{2P}{\pi t D}$$

Where σ_t is the splitting tensile strength, P is the maximum load applied, t is the thickness of the specimen, and D is the diameter. The test was performed on eight specimens with 1-inch diameter × 0.5-inch height at a 0.2 mm/min rate. Data of extension and load were recorded at a 0.1s interval, using Instron Bluehill 3, a software developed to run Instron testing instruments (Fig. 3.1f).

Uniaxial compressive test

In the uniaxial compressive strength test (Fig. 3.3b), a cylindrical specimen with a thickness-to-diameter ratio of 2:1 is subjected to a uniform vertical normal stress parallel to the specimen axis until it fails (ASTM D7012-14). The test was performed on eight specimens with 0.5-inch diameter x 1-inch height at a rate of 0.125 mm/min. Once again, the data of extension and load were recorded at 0.1s intervals. Values of stress were calculated by dividing the load (N) by the cross-sectional area (m^2), and the strain was calculated by dividing the extension (mm) by the

original thickness (mm). Thus, stress vs. strain curves were generated, and the compressive strength was calculated (σ_c) at yield point for all samples.

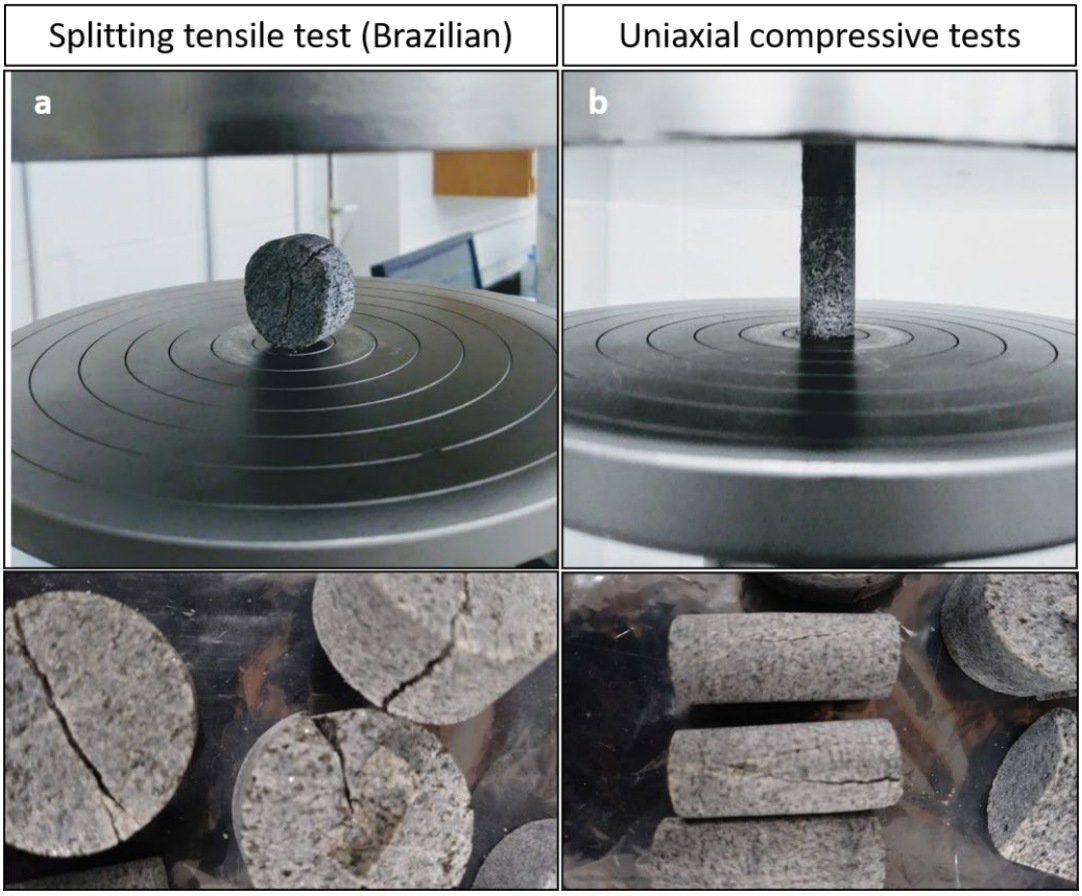

Figure 3.3. Fractured specimens after splitting tensile test (a) and uniaxial compressive test (b). Bottom figures show a zoomed view of samples.

The values of tensile and compressive strengths obtained from experiments were then to estimate cohesion (c) and the friction angle (ϕ) of the crystalline rock, which were added to the simulations input parameters. According to Sivacugan et al. (2014), c and ϕ can be derived from σ_t and σ_c, by applying the following equations:

$$c = \frac{0.5\sigma_c\sigma_t}{\sqrt{\sigma_t\sigma_c - 3\sigma_t}}, \qquad \phi = \sin^{-1}\left[\frac{\sigma_c - 4\sigma_t}{\sigma_c - 2\sigma_t}\right]$$

Figure 3.4 shows the Mohr circle for the state of stress, and the relation between tensile strength, compressive strength, friction angle, and cohesion.

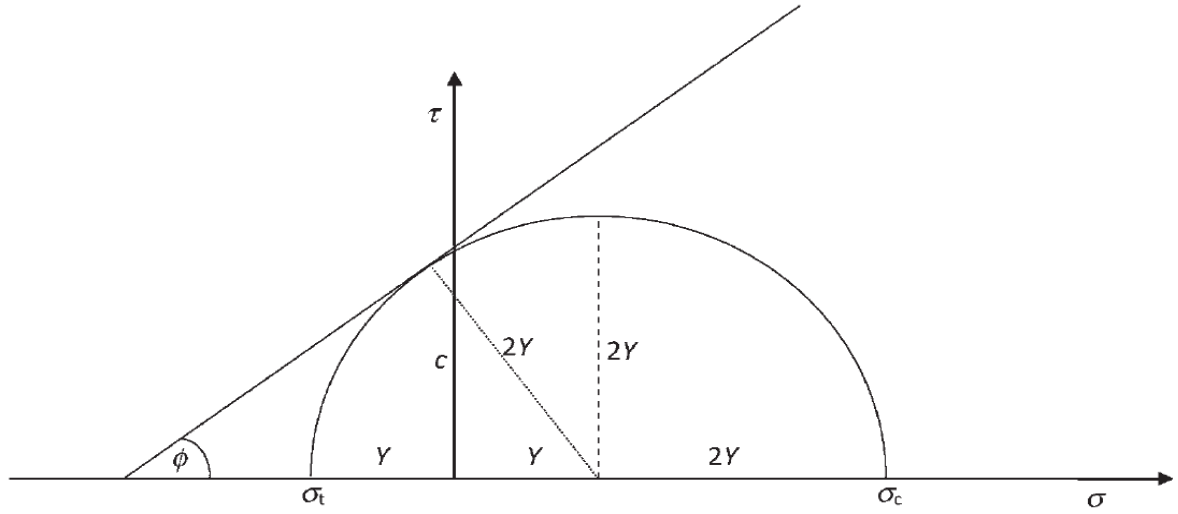

Figure 3.4. Mohr circle for the state of stress. X axis is the normal stress, which can be negative (tension, σ_t) or positive (compression, σ_c). Y axis is the shear stress. Cohesion (c) is "the shear strength when normal stresses are equal to zero". Φ is the material angle of friction. Adapted from Sivacugan et al. (2014).

Modeling with iSALE-2D

Wetumpka's cratering process was simulated by iSALE-2D, an extension of the SALE hydrocode developed and extensively used to model impact-crater formation (Melosh et al., 1992; Ivanov et al., 1997; Collins et al., 2004; Wünnemann et al., 2006). Relying on iSALE-2D database, different equations of state (EOS) were applied to each target material. The target model consisted of three layers: a) crystalline basement represented by granite EoS; b) the sediment layer, which is represented by the wet tuff EoS, and c) the uppermost seawater layer.

ANEOS equations, analytic EOS for shock physics, were used for granite (Melosh, 2007), whereas Tillotson equations commonly used alternative EOS for planetary collisions were applied

for wet-tuff and water. The ROCK strength model, which defines the yield strength as a function of the measure of damage, was used in this study to describe the mechanical behavior of the target material. The damage model presented by Collins et al. (2004) was used to account for pressure and shear in the material. Finally, a strain-based porosity model proposed by Wünnemann et al. (2006) was used for the sediment layer (see Annex 2-6 for details on equations of state, damage, strength, and porosity models).

To account for the continental shelf slope, simulations were performed with different water depths (62.5 m and 125 m) and different sediment thicknesses (100, 200, and 300 m) while maintaining the impactor and target properties. Table I summarizes material input parameters used for each target layer.

The simulations were performed limiting the scope to an axisymmetric approximation of the original impact problem and a resolution of 32 CPPR (cells per projectile radius), reflecting a cell size of 6.25 meters. The impactor was represented by a 400-meter granitic sphere traveling at either 12 km/sec or 20km/sec. The lower velocity simulation approximates the case of oblique impact by considering the vertical component of the impact velocity. Simulation output figures were generated using the plotting tool pySALEPlot. Table II displays resolution information and grid dimensions used in the simulation.

Table 1. Material inputs in target layers.

Material input	**Target**		
Parameters	Metamorphic basement	Sediment layer	Water
EoS	Granite (aneos)	Wet tuff (Tillotson)	Water (Tillotson)
Thickness	~3,000 m	100-200-300 m	60 - 125 m
Strength model	ROCK	ROCK	HYDRO
Damage model	COLLINS	COLLINS	-
Porosity model	None	Wünemman (15%)	-
Cohesion (intact)	$1.712*10^{7}$	$2.5*10^{6}$	-
Cohesion (damaged)	1*104	1*104	-
Friction angle (intact)	0.392	0.69	-
Friction angle (damaged)	0.4	0.69	-

Table 2. Resolution, cell size, and grid dimensions.

Parameter	**Input**
CPPR (cells per projectile radius)	32
GRIDSPC (grid spacing)	6.25 meters
GRIDH (# of cells in horizontal grid) - Left extension zone	0
GRIDH - Central high-resolution zone	2000
GRIDH - Right extension zone	90
GRIDV (# of cells in vertical grid) – upper extension zone	90
GRIDV – central high-resolution zone	1000
GRIDV – lower extension zone	90
High resolution zone (horizontal x vertical)	12.5 x 6.25 km

Chapter 4. Results

Experiments

Mechanical tests on schist rock samples from the rim provided tensile and compressive strength values for each specimen (Table 3 and 4) (Compiled results in annexes 8 and 9). The average tensile strength (σ_t) and compressive strengths were σ_t=9.747 MPa and σ_c=50.194 MPa, respectively. We used the cohesion (c = 17.118 MPa) and friction angle (ϕ = 0.375) obtained from this analysis in iSALE-2D simulations as input in the material file for the bedrock material.

Table 3. Tensile strength values for each specimen submitted to Brazilian tensile test

Tensile strength=$2P/\pi DL$		
Specimen	**P-max load (N)**	**Tensile Strength (MPa)**
Braz1	4291.8228	8.2856
Braz2	5476.2266	10.6943
Braz3	4933.5430	9.9174
Braz4	5708.4478	11.5072
Braz5	4842.2305	9.8438
Braz6	4046.4385	7.8366
Braz7	5203.6250	10.3326
Braz8	4996.4204	9.5610

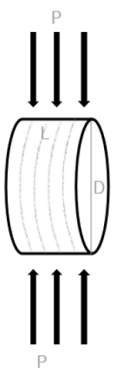

Table 4. Compressive strength values for each specimen submitted to uniaxial compressive test

Compressive strength = P/A			
Specimen	**Area (m^2)**	**P-max load (N)**	**Compressive strength (MPa)**
Comp1	0.000130293	5888.0986	45.1912
Comp2	0.000123505	6984.9023	56.5556
Comp3	0.000122326	7531.9043	61.5724
Comp4	0.000122522	7220.3091	58.9307
Comp5	0.000122522	6368.8389	51.9812
Comp 6	0.000122326	5347.4565	43.7148
Comp7	0.000123308	4711.8950	38.2124
Comp8	0.000123702	5651.2798	45.6846

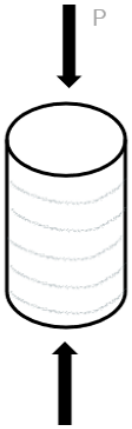

Numerical modeling

The analysis of impact conditions, such as impact velocity, sediment thickness, and water depth, were performed by comparing pairs of simulations, in which parameters were kept the same except the parameter being evaluated. For example, to analyze how impact velocity affects the cratering process, two model runs with different impact speeds, but the same sediment thickness and water depth were compared. In this instance, the crater dimensions produced by the lower impact speed of 12km/sec best approximates the actual crater than the faster impact scenario of 20km/sec. Figure 4.1 shows the crater evolution for both velocities at about 11, 30, and 90 seconds, during the maximum opening of the transient crater, rim flap/tsunami formation, and final crater,

respectively. At about 11 seconds, the maximum excavation reaches approximately 1.5 km in depth and 5 km in diameter in the lower speed scenario, whereas in the higher speed impact reaches about 1.8 km in depth and 6 km in diameter. After rim flap and subsequent tsunami wave formation (~30 sec), material from the rim collapses back into the crater bowl, widening and filling the entire structure in both scenarios. At this point, we can see that the higher velocity model contains a higher volume of crystalline material as proximal ejecta than the lower velocity model. Final dimensions are visible at about 90 seconds and are approximately 6 km in diameter and 1.3 km in depth, in slower impact scenario, and 8 km in diameter and 1.7 km in depth, in faster impact scenario.

As expected, peak pressures are slightly higher in the 20km/sec impact in comparison to the 12km/sec impact, considering the higher amount of kinetic energy released by the faster impactor. Figure 4.2 shows the model outcome for pressure at 0.1 seconds and graphs indicating a maximum pressure of 42 GPa in the lower velocity model and 47 GPa in a higher velocity model.

Peak temperatures (Fig. 4.3) are significantly different in both impact velocity situations. Not just the peak value, but also the area of target affected by maximum temperature conditions. The lower velocity model (12 km/sec) produces a peak of temperature of approximately 4,500 K, whereas the higher velocity model (20 km/sec) creates temperature conditions almost 75% higher, reaching approximately 7,800 K. The volume of target rocks that undergoes such high temperatures are significantly higher in the faster impact (20 km/sec) speed scenario, which is represented by the noticeable reddish area in figure 4.3. At 0.1 seconds after the impact, this high-temperature region, which radially involves the crater floor and walls, seems to be positively related to the size of the transient crater, which is also almost doubled in the higher speed scenario.

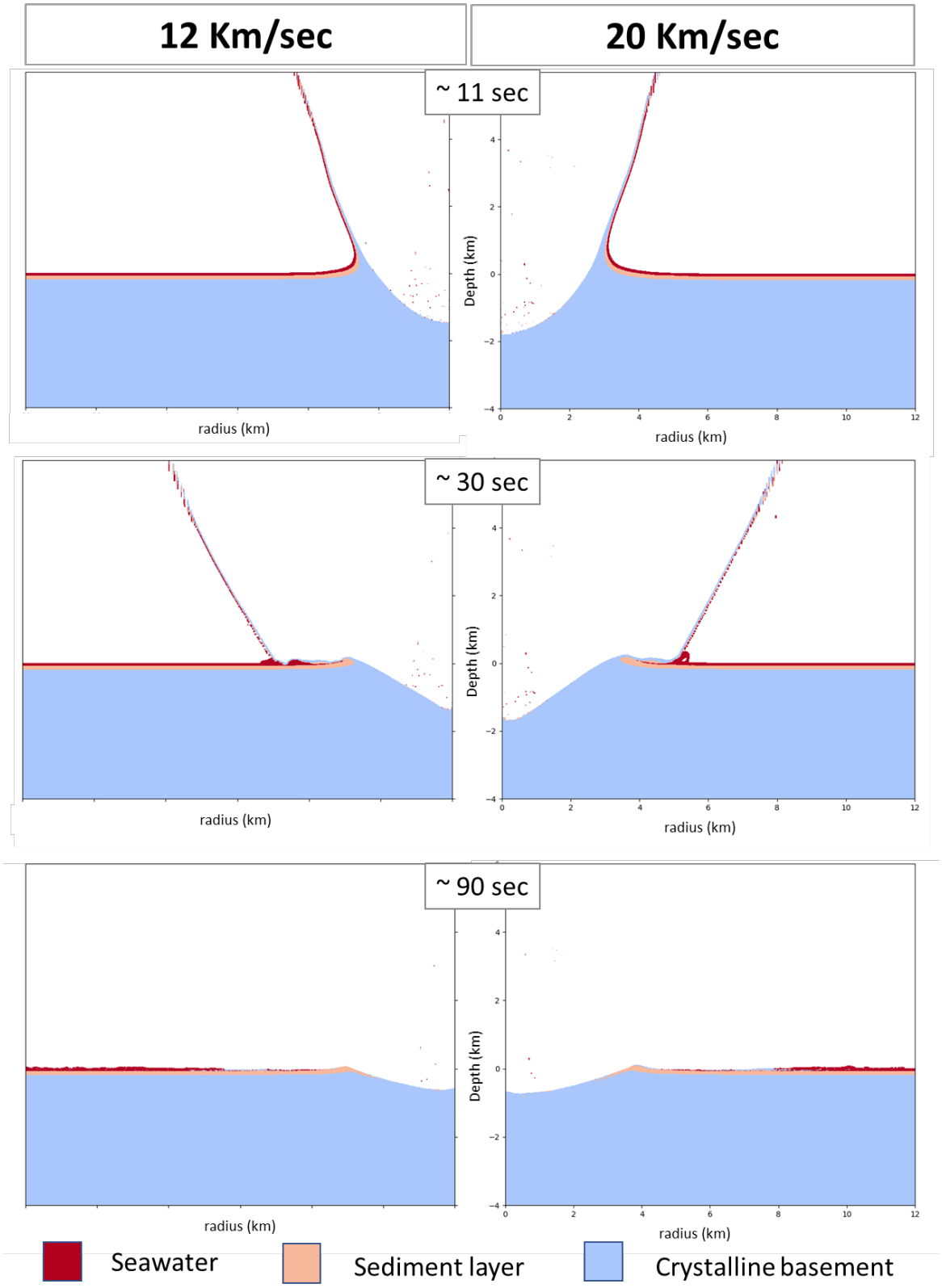

Figure 4.1. Comparison between different impact speed scenarioS. ISALE2D outcomes shows crater evolution for both impact velocitites. Maximum opening of transient crater occurs at ~11 seconds, rim flap/tsunami formation at ~30 seconds, and final crater at ~90 seconds. On both models, the sediment thickness is 100 meters, and the water depth is 62.5 meters.

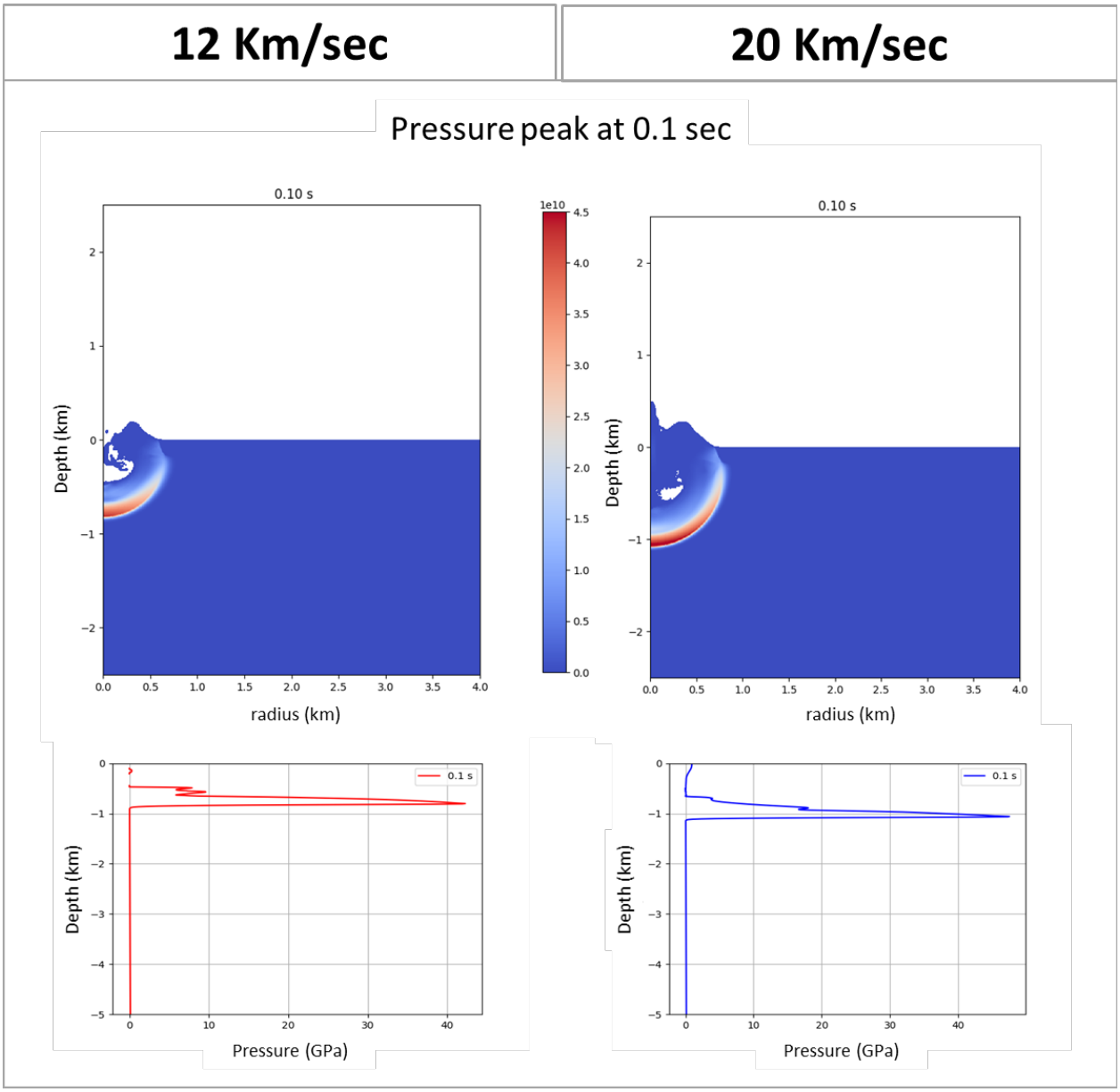

Figure 4.2. Peak pressures at 0.1 seconds from lower (left) and higher (right) velocity model. Graphs show pressure by depth near the center of the crater at 0.1 seconds.

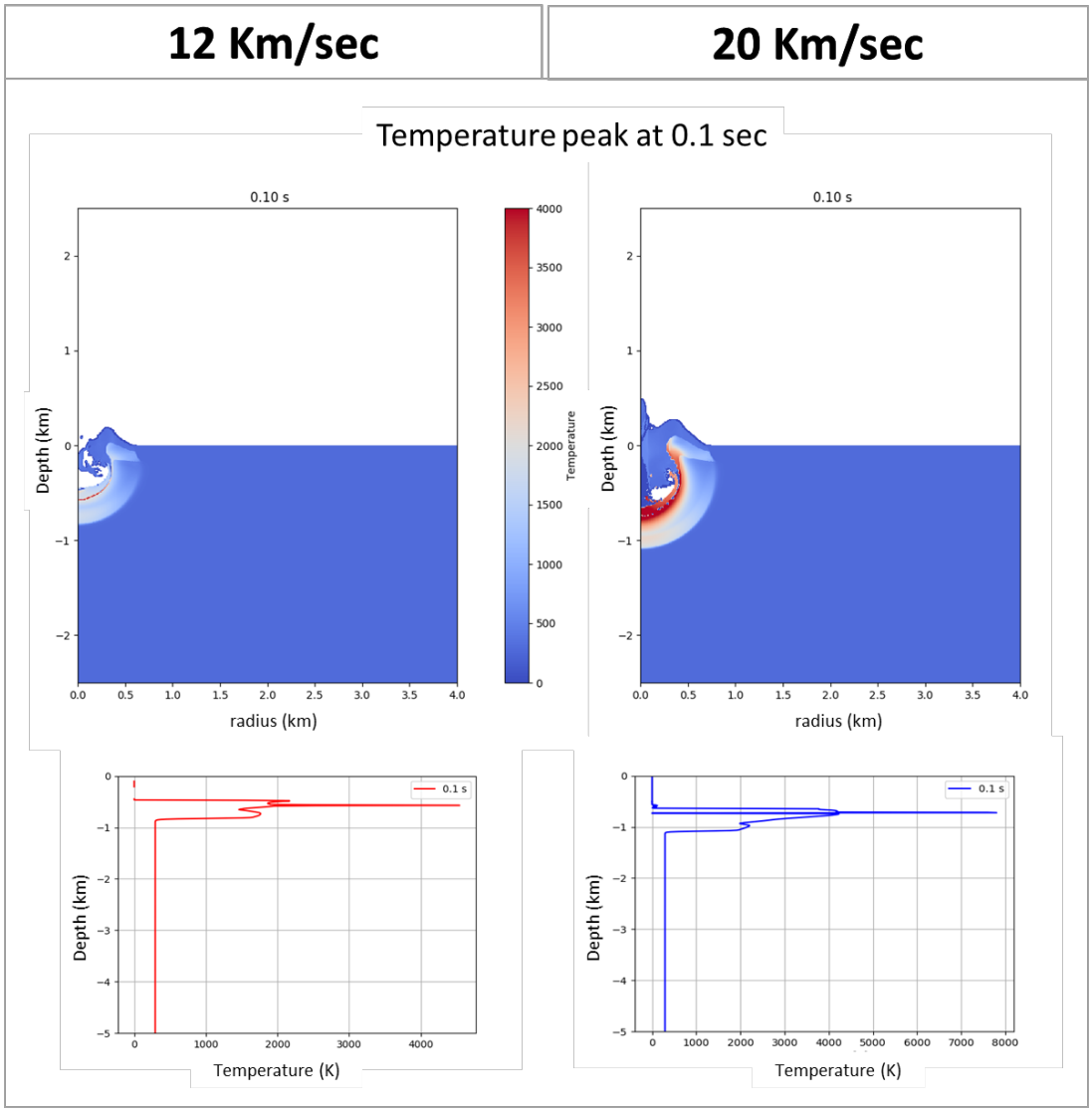

Figure 4.3. Temperature peaks at 0.1 seconds from lower (left) and higher (right) velocity model. Graphs show temperature by depth near the center of the crater at 0.1 seconds. Scale on figure goes from 0 (blue) to 4000 K (red).

The overall velocity of the outgoing tsunami wave ranges from 50 m/sec and 120 m/sec in both the lower and higher speed model, except at the wavefront, where the falling ejecta curtain accelerates the outgoing mass of water, reaching more than 150 m/sec. Figure 4.4 shows model outcomes around 30 seconds representing the outward/inward movement of target material in the

X-direction. There is a very discrete higher velocity and amplitude in the 20km/sec impact condition at this specific time step, but as the crater develops, the outgoing wave does not show substantial differences between both impact speed conditions. However, a higher velocity at specific time steps can improve the displacement of larger blocks close to the crater rim. The blue region along the crater walls indicates an inward movement during the accommodation of the entire structure in the modification stage.

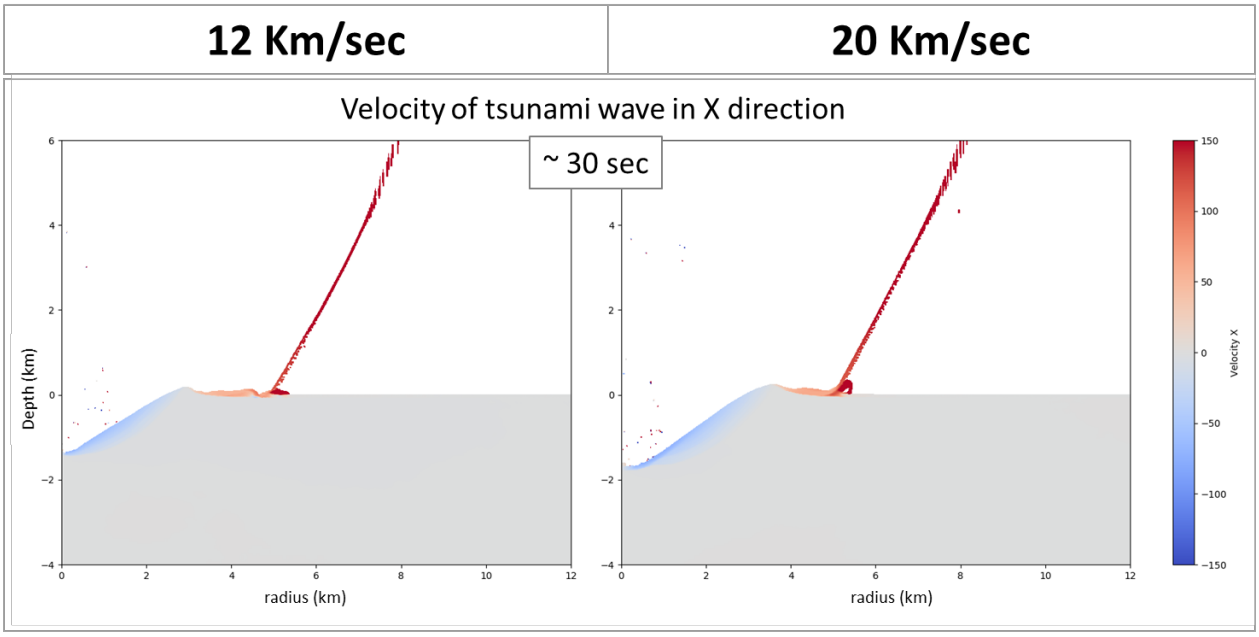

Figure 4.4. Velocity of material flow in the x-direction, in lower and higher velocity scenario. Scale on figure goes from -150 (blue) to 150 m/sec (red).

In the simulations, the accumulation of damage is represented by the totality of tensile and/or shear failure, which are calculated and combined by the used damage model (Collins et al., 2004). The total damage is mainly accumulated during the excavation stage when the shock waves

expand and dissipate. The tensile failure occurs near the surface, where target rocks experience relief of shock-induced high pressure and below the crater floor due to divergent crater growth flow and rebound movement. The shear failure occurs during the expansion of the transient crater and is caused by the passage of compressive waves and shear deformation (Collins et al., 2004). Maximum values of tensile damage (DAM=1) are achieved when flaw expansion is mature enough that the fractures cross the cell's width. For shear, the maximum damage is reached when the plastic strain is equal to plastic strain at failure, being closely related to local pressure (Collins et al., 2004).

Figure 4.5 illustrates the accumulation of damage in the lower and higher velocity simulated impact events at about 30 seconds. Both model runs show a similar concentric pattern of total damage expanding laterally along a line parallel to the surface. However, in the lower velocity impact simulation, the concentrical damaged area reaches a total depth of approximately 4 km and a radius of about 4.5 km, whereas, in the higher velocity model, it reaches about 5 km in depth and 5.5 km in radius.

According to Collins et al. (2004), the shear failure and tensile damage are confined to the brittle near-surface zone, but because the tensile strength is not dependent on depth, the transition from completely damaged to relatively undamaged material can be abrupt, as observed in figure 4.5.

To investigate how the sediment layer affects the cratering process, three model runs with different sediment layer thicknesses, but the same impactor velocity and water depth were compared. Figure 4.6 illustrates three different simulations, at approximately 80 seconds, in which

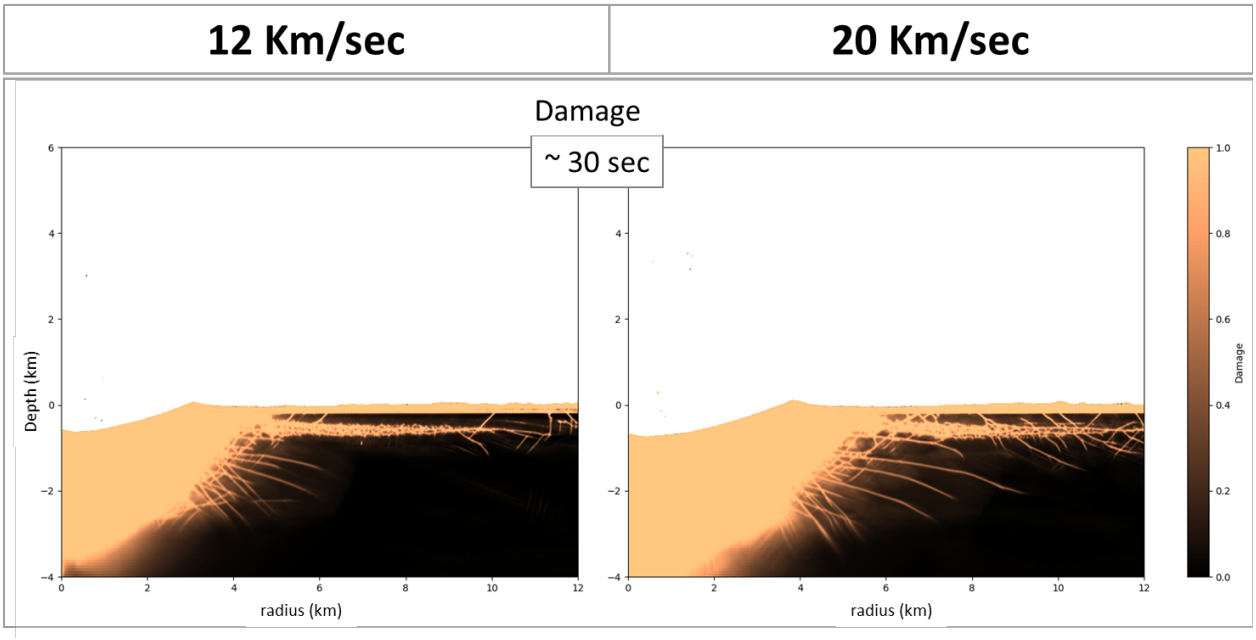

Figure 4.5. Damage contours from lower (left) and higher (right) impact speed simulations. Scale on figure goes from 0.0 (black) to 1.0 (yellow).

the sediment layer varies at steps of 100, 200, and 300 meters. The water depth is set as 62.5 m and impactor velocity as 12km/sec. Although all three scenarios show the crater rim mainly composed of sedimentary material, the main difference is that as the layer thickness increases, a progressively higher volume of sedimentary material comprises the rims and upper crater walls (Figure 4.6).

In all three different sediment layer thickness scenarios, the crater evolves in a similar manner, with the maximum transient crater opening at about 15 seconds, followed by the rim flap and subsequent tsunami formation at approximately 25 seconds. During the modification stage, the entire structure structurally accommodates, and sedimentary material from the rims starts to collapse back into the crater cavity. This process can be observed in model plots of the horizontal

(x-direction) velocity of material flow (Fig.4.7) and occur at slightly different time steps in the three sediment layer thickness conditions. As the sediment layer thickness increases, the collapse

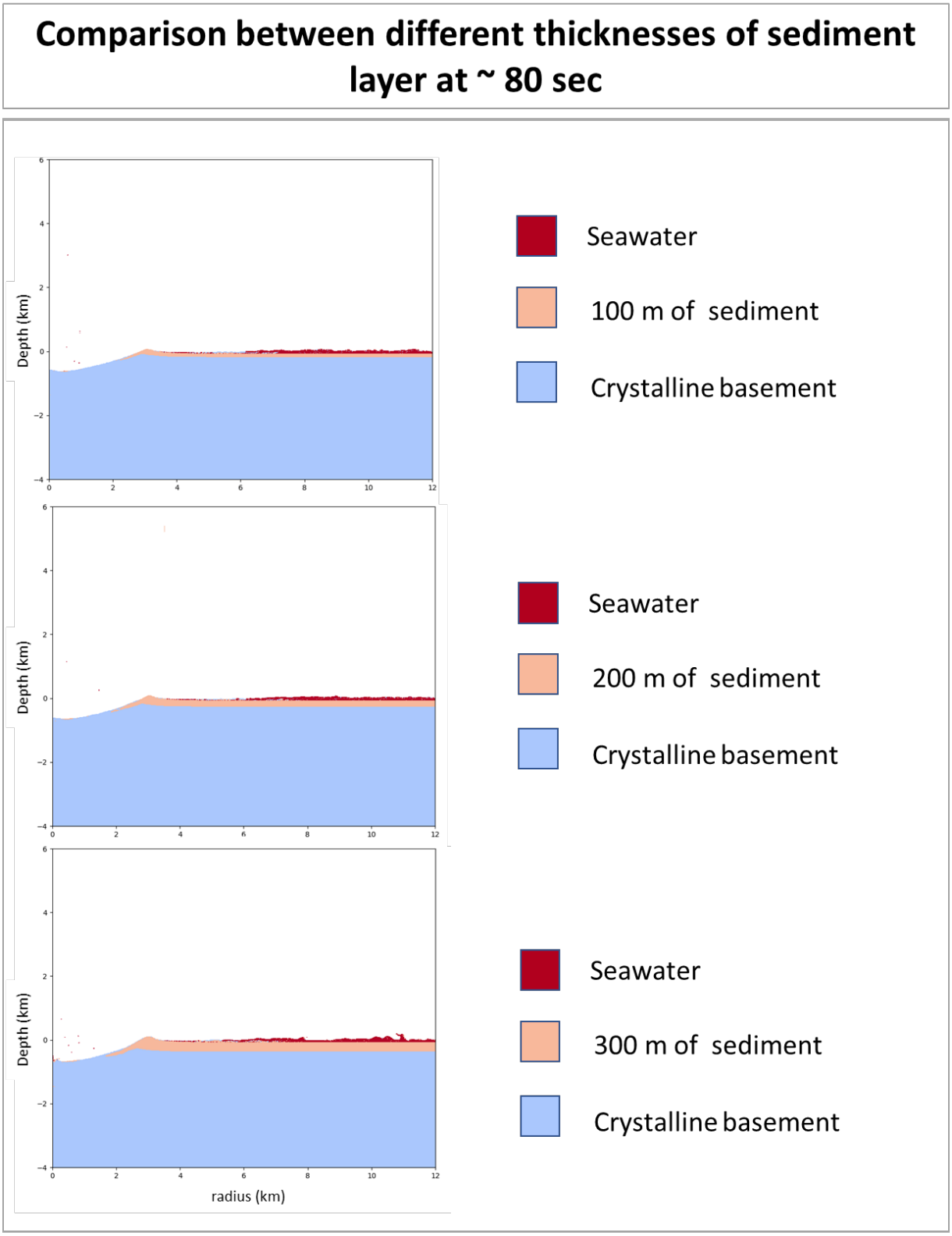

Figure 4.6. Comparison between different sediment layer thicknesses. iSALE2D outcomes shows cratering process at about 80 seconds, when tsunami waves are moving outwards. On the three models, the water depth is 62.5 meters and impactor velocity is 12km/sec.

of sedimentary material from the rims occurs at progressively earlier time steps. For the thinnest sediment layer condition (100 meters), the collapse starts at 149 seconds; for the intermediate condition (200 meters), it occurs at 138 seconds; finally, for the thicker layer scenario (300 meters), it occurs at 124 seconds.

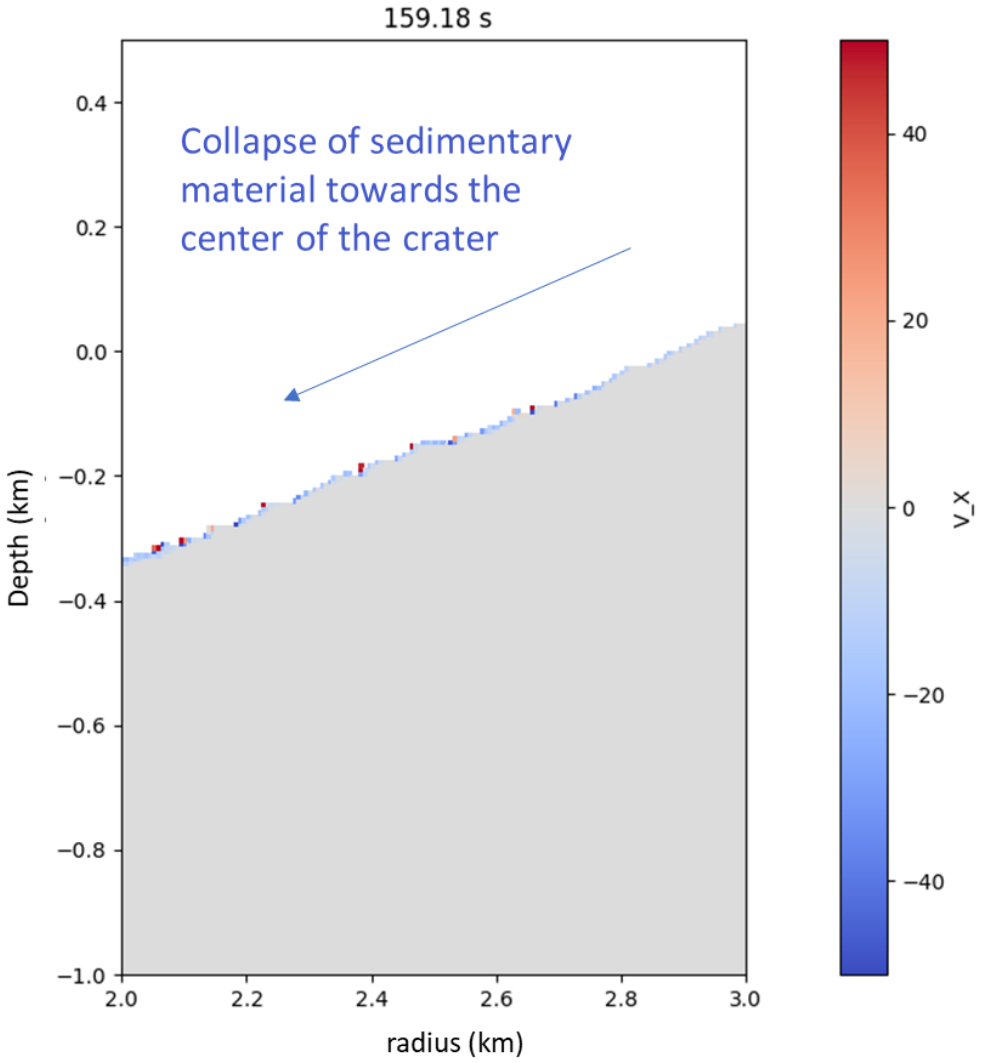

Figure 4.7. Model output of velocity of material in the x-direction. Zoomed to the crater walls. Scale on figure goes from -50 (blue) to 50 m/sec(red). Blue layer on top of crater walls indicates movement of material to the left, towards the crater center

The comparison between water depth scenarios, 62.5m and 125m (Fig. 4.8), does not show any significant difference in the cratering process but in the amplitude of outgoing tsunami wave, which is higher in the deeper target water setup. On the other hand, in the shallower target (62.5m), the rim seems' to have a slightly higher content of sediment material toward crater walls.

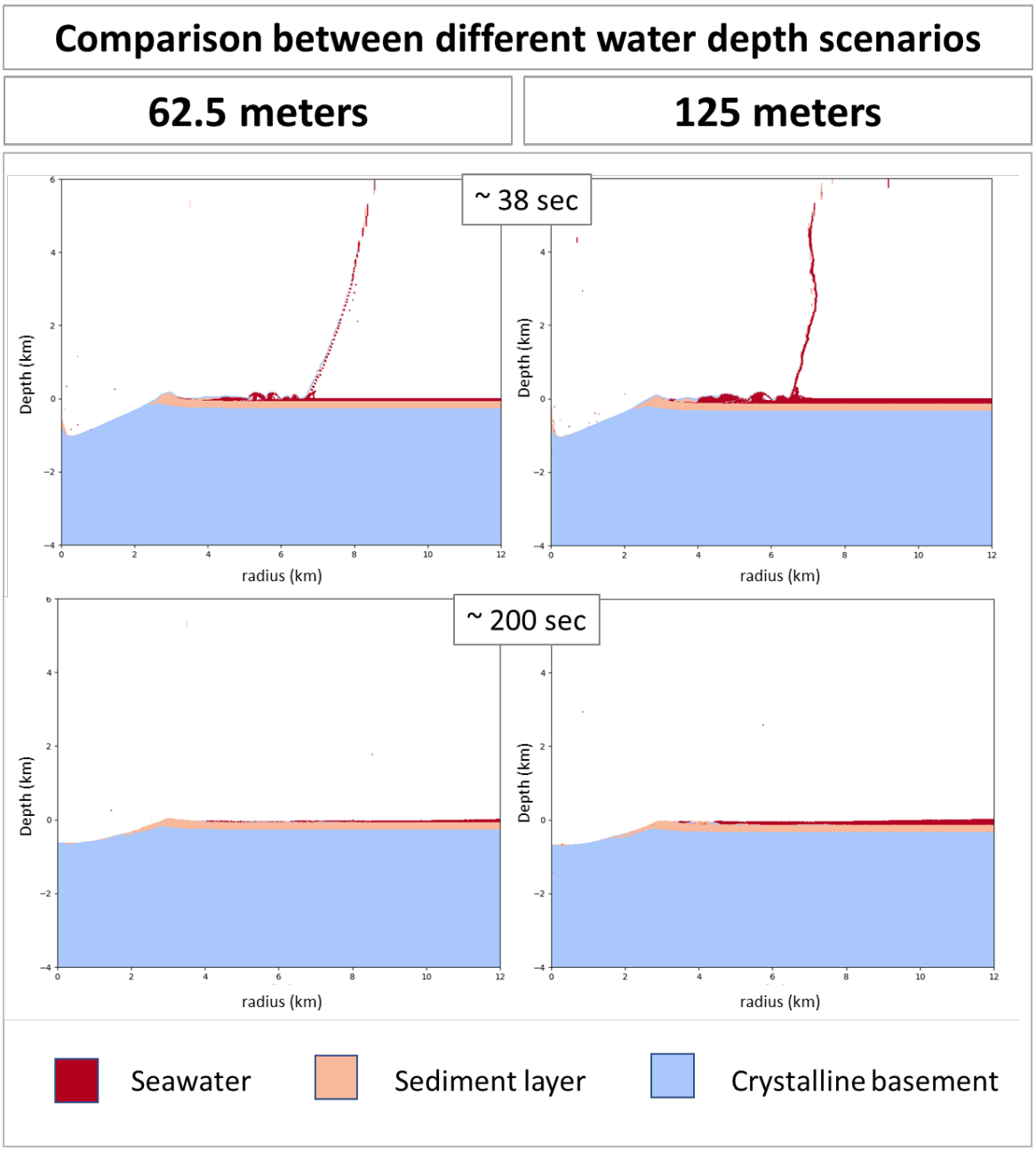

Figure 4.8. iSALE outputs from 62.5m (left) and 125m (right) water depth scenarios, at 38 and 200 seconds. Both models consider the impactor velocity as 12km/sec and sediment layer thickness as 200 meters.

The velocity of the outgoing tsunami wave does not differ significantly between both water depth target scenarios. Figure 4.9 exhibits simulation outcomes of material velocity in the x-direction at approximately 40 seconds, representing the outward/inward movement of target material. The tsunami wave's velocity is between 50 m/sec and 120 m/sec in both the shallower (62.5 meters) and deeper (125 meters) target water model, except at the wavefront, where the velocity exceeds 150 m/sec due to the contribution of movement from the falling ejecta curtain, that accelerates the mass of water. The main difference between the distinct water depth scenarios is the continuity of the ejecta curtain, which seems to be more fragmented in the shallower sea scenario and continuous in the deeper water condition.

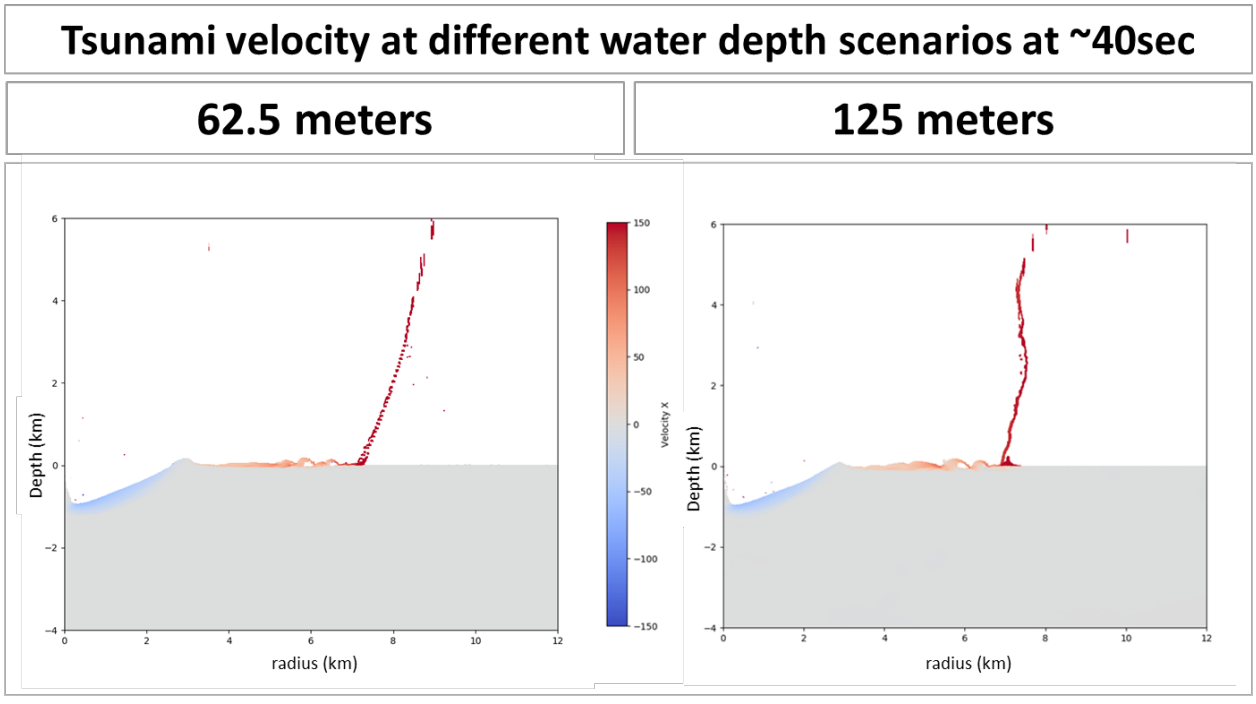

Figure 4.9. Velocity of material flow in the x-direction, in shallower (62.5 m) and deeper (125 m) water depth scenario. Scale on figure goes from -150 (blue) to 150 m/sec (red).

Best-fit model

Based on comparisons between different models and known characteristics from field and drilling campaigns, the most similar model to the actual structure (focusing on the southwestern rim) considers a target water depth of 62.5 m and sediment thickness of 200 m. The choice of sediment thickness is reassured by drill core data in an adjacent part of Montgomery County about 20 km south of Wetumpka, which is reported to be approximately 240 m (Knowles et al., 1960).

The lower velocity (12 km/sec) model produced an impact structure with more sedimentary component of the crater rim and less crystalline component as proximal ejecta at the end of crater excavation stage. This is consistent with the expected southern rim development based on the field and drill core observations in the crater interior. Further, the transient and final crater depths and diameters produced with the 12 km/sec velocity are consistent with our best understanding of the overall crater structure. In this case, the crater rim comprised almost entirely of the sedimentary target material as expected for the southern rim, albeit the sectors with a remaining crystalline rim indicate a target sequence in these parts with less water and sediments. The layers of ejected crystalline material were relatively much thinner in comparison to the 20km/s simulation and appeared to break up and largely come to reside just beyond the crater rim. As summarized in Chapter 2, the drill cores penetrated crater-filling units that were almost entirely composed of sedimentary target materials, much of which had entered through the collapsed southern sector of the rim. It should be noted that the discussion of results relates closely to the southern and southwestern rim aspects of Wetumpka impact structure, which are relatively much better understood owing to the location of key outcrops (King and Ormö, 2011). Key time steps in the 12 km/sec velocity model show considerable amounts of sedimentary material, during the early

modification stage, moving from the rim back into the crater, which is supported by the field and drill-core findings for the upper ~ 210 m of the crater-filling sequence.

Figure 4.10 shows the velocity of material flow in the x- and y-direction at 0.5 seconds, illustrating the downward/outward movement of material in the lower levels, and upward/outward movement in upper levels, during the early excavation stage from the best-fit iSALE model.

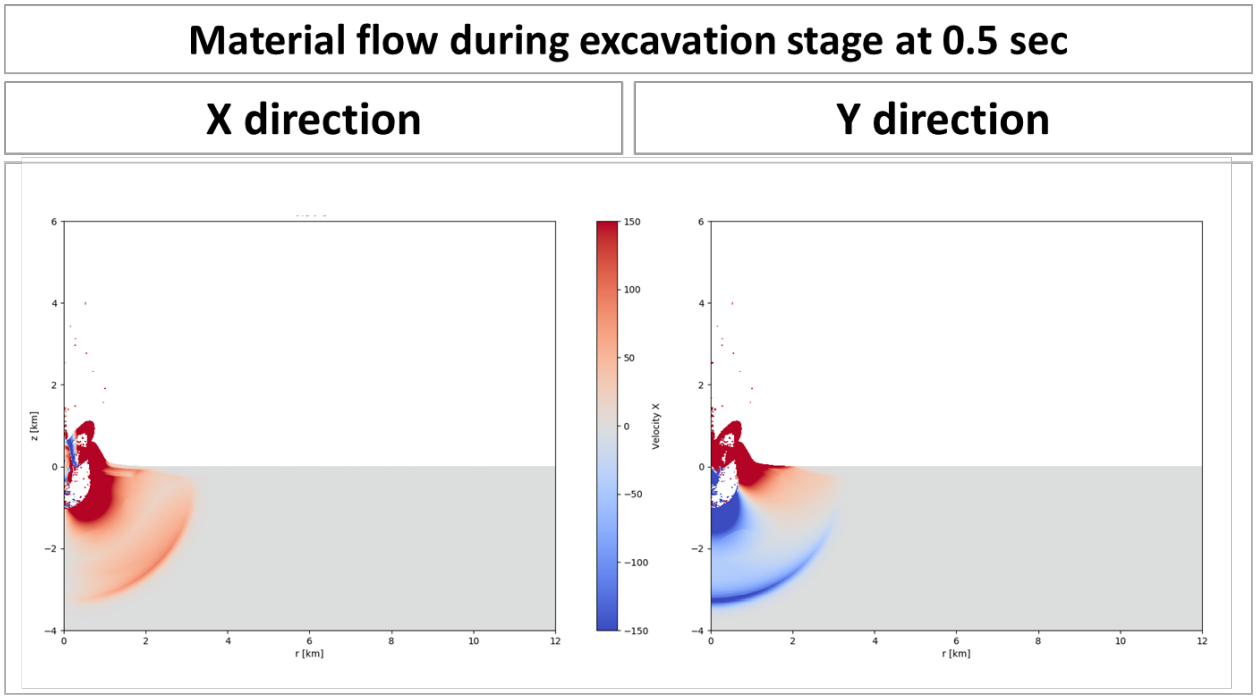

Figure 4.10. iSALE-2D plot of velocity of material flow in the x- and y-direction at 0.5 seconds from best-fit model. Scale on figure goes from -150 m/s (blue) to 150 m/s (red).

Figure 4.11 shows six key time steps during crater development. The first three time steps are summarized as follows; At 2.00 seconds, during early excavation, the transient crater is opening and has attained a depth of well over 1 km. We note that the ejecta flap in this time step is largely sedimentary material. At 14.00 seconds, at the maximum transient crater development (or moment of theoretical balance as per French, 1998), more crystalline material has become part of the crater rim and ejecta flap. This is important because it heralds the inclusion of crystalline blocks within

the overturned rim and proximal ejecta, but the crystalline component is not so great that it forms a coherent crystalline-upon-sedimentary target flap as, for instance, noted at marine crater Lockne in Sweden (Lindström et al., 2005). At 28.21 seconds, during near-field ejecta outward movement and initial tsunami formation, several things are happening of note. These are: development of an overturned rim of mainly sedimentary material (drilled at AU scientific core hole #09-04; King and Ormö, 2011); emplacement of thin, discontinuous ejecta of crystalline blocks upon and slightly beyond the crater rim; ejecta-curtain forcing ("pushing") the seawater away from the crater as it falls outward (adding to the rather poorly developed rim-wave tsunami); and the initial rebound of the transient crater floor and coeval initial slumping of crystalline crater wall materials. As the driving mechanism for the outwards tsunami in the model differs slightly but significantly from the rim wave tsunami formation described by Wünnemann et al. (2007), it is here described as an' ejecta emplacement tsunami' reminiscent of the "debris surges" of target strata caused by ballistic ejecta bombardment (cf. Oberbeck, 1975).

The next three time steps from Figure 4.11 are as follows. At 45.02 seconds, during modification involving a rebound of the crater floor (now much less than 1 km, and with a minor central hump feature) and during continued slumping of crystalline material from the crater walls, outward tsunami propagation continues, and the collapse of the ejecta curtain continues to contribute to the outward tsunami development.

At 72.48 seconds, during continued modification, the crater rebound has reduced floor depth to less than 0.5 km through a combination of rebound and slump of crystalline material from the crater walls. Seawater flow is still outwards, but notably, a small amount of sedimentary rim material is starting to flow back into the crater. At 174.59 seconds, as shown especially in the

enlarged view of the crater rim area, significant quantities of sedimentary rim material are now slumping into the crater bowl. In terms of crater-filling sequence, at 174.59 seconds, the model shows the transition from the lower more-dense crater-filling unit (2.6 g/cm^3 in the cited gravity model - Ch.2) and the overlying (2.1 g/cm^3) sedimentary fill.

Figure 4.12 shows the location of an evolving zone of elevated shock pressures in the best fit iSALE model. The model shows a maximum pressure of approximately 42 GPa near the center at 0.1s. However, this rapidly decays to 16 GPa, 7 GPa, and 3GPa at 0.2, 0.3 and 0.4 seconds, respectively. It should be noted that diaplectic glass, expected at 45 GPa pressure (French, 1998) (Fig. 4.14), has not been observed to date in field and drill core samples. Even though the pressures indicated here are slightly higher than suggested by petrographic analysis, the model generally affirms the field- and laboratory-based evidence within impact-affected quartz grains. Figure 4.13 shows the temperature peak in the chosen model at 0.1 seconds. The model indicates a maximum temperature of approximately 5,600K (5,325 Celsius degrees) near the center of the crater at about 0.7 km of depth.

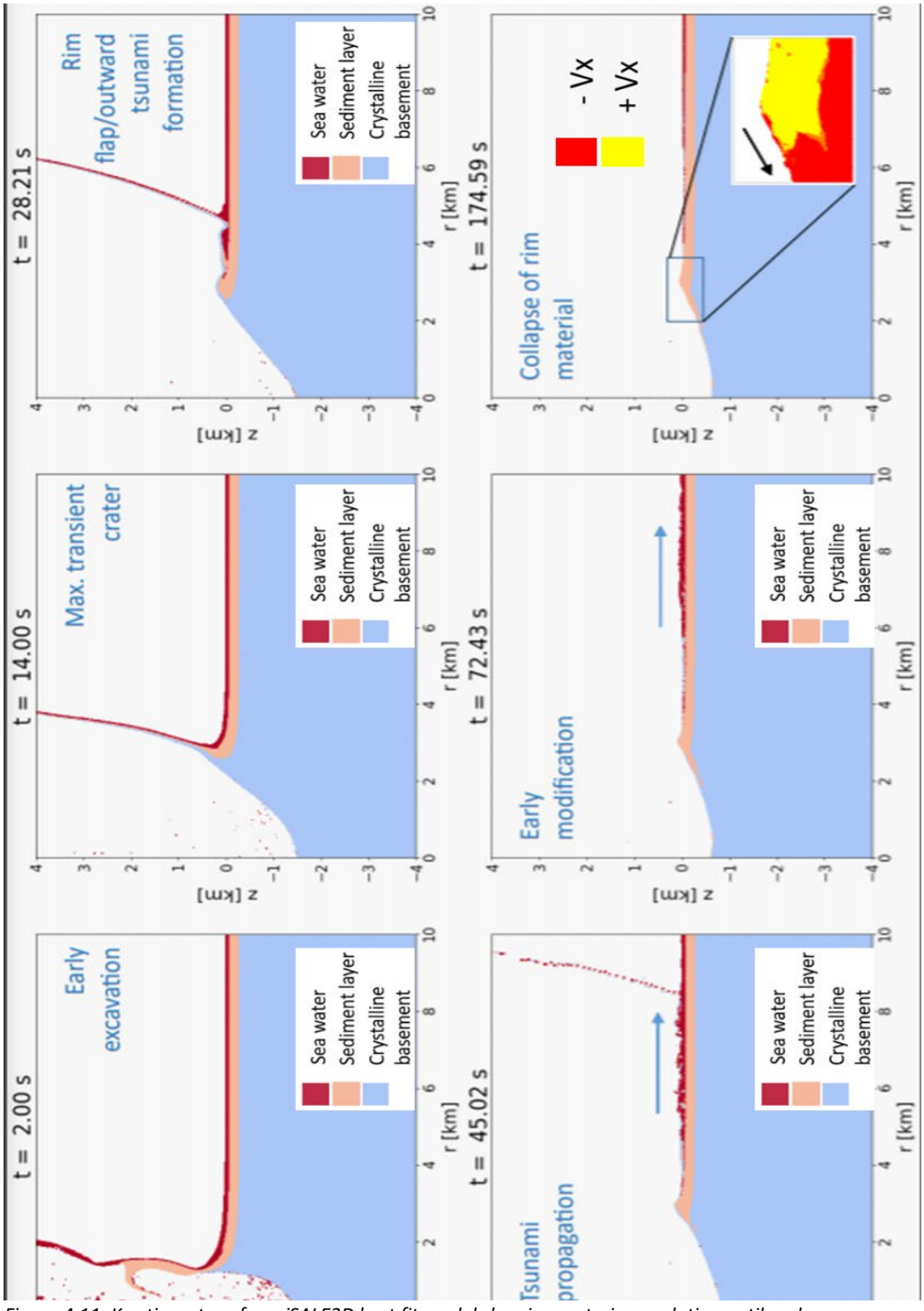

Figure 4.11. Key time steps from iSALE2D best fit model showing cratering evolution until early modification stage. 400m-projectile traveling at 12 km/s, 62.5m water depth, and 200m of target sediments. Inset figure for t=174.59 seconds shows the direction of the velocity in the x direction. Red and yellow represent the horizontal component of the velocity in the negative and positive X-direction respectively (modified from De Marchi et al., 2021).

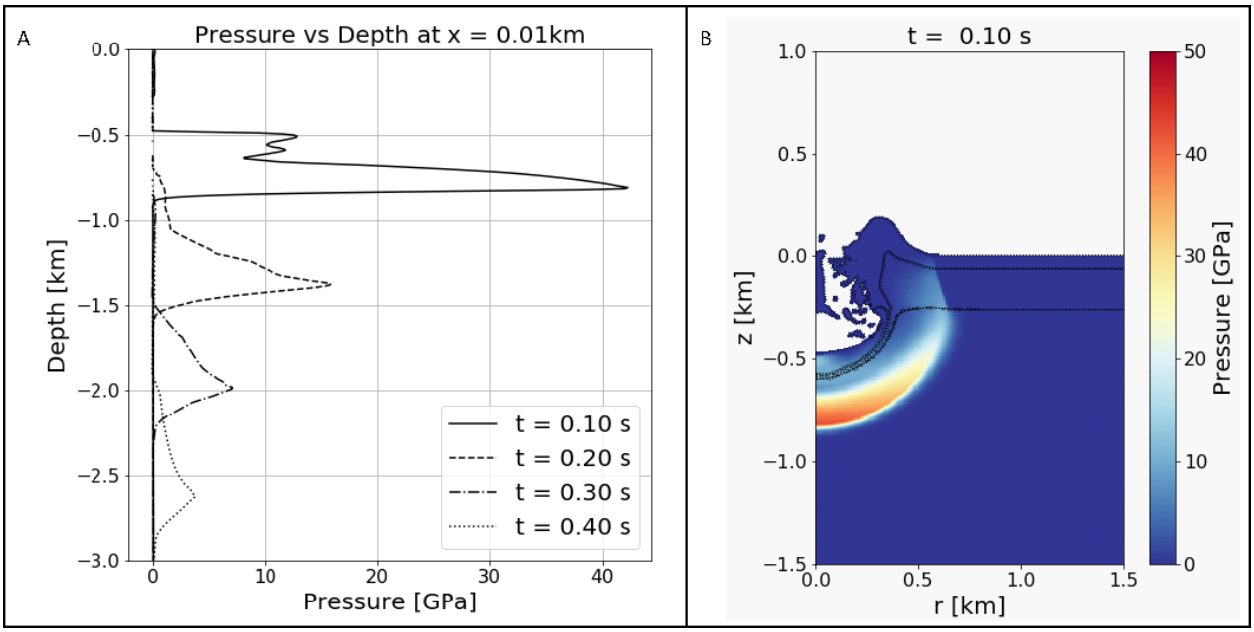

Figure 4.12. Pressure peaks at the first tenths of seconds from our best fit model. A: evolution of pressure by depth near the center of the crater at 0.1, 0.2, 0.3 and 0.4 seconds. B: pressure plot at 0.10 seconds after the impact. Scale on figure goes from 0 (blue) to 50 GPa (red) (De Marchi et al., 2021).

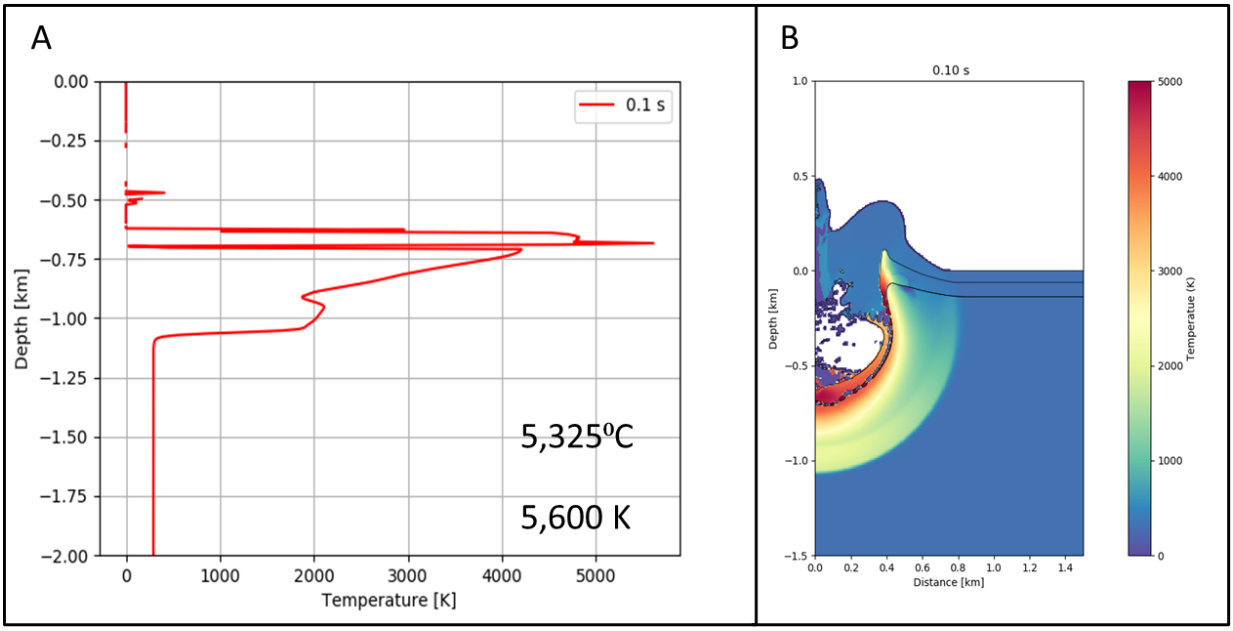

Figure 4.13. Temperature peak from best fit model. A: temperature by depth near the center of the crater at 0.1seconds. B: temperature plot at 0.10 seconds after the impact. Scale on figure goes from 0 (blue) to 5000 K (red).

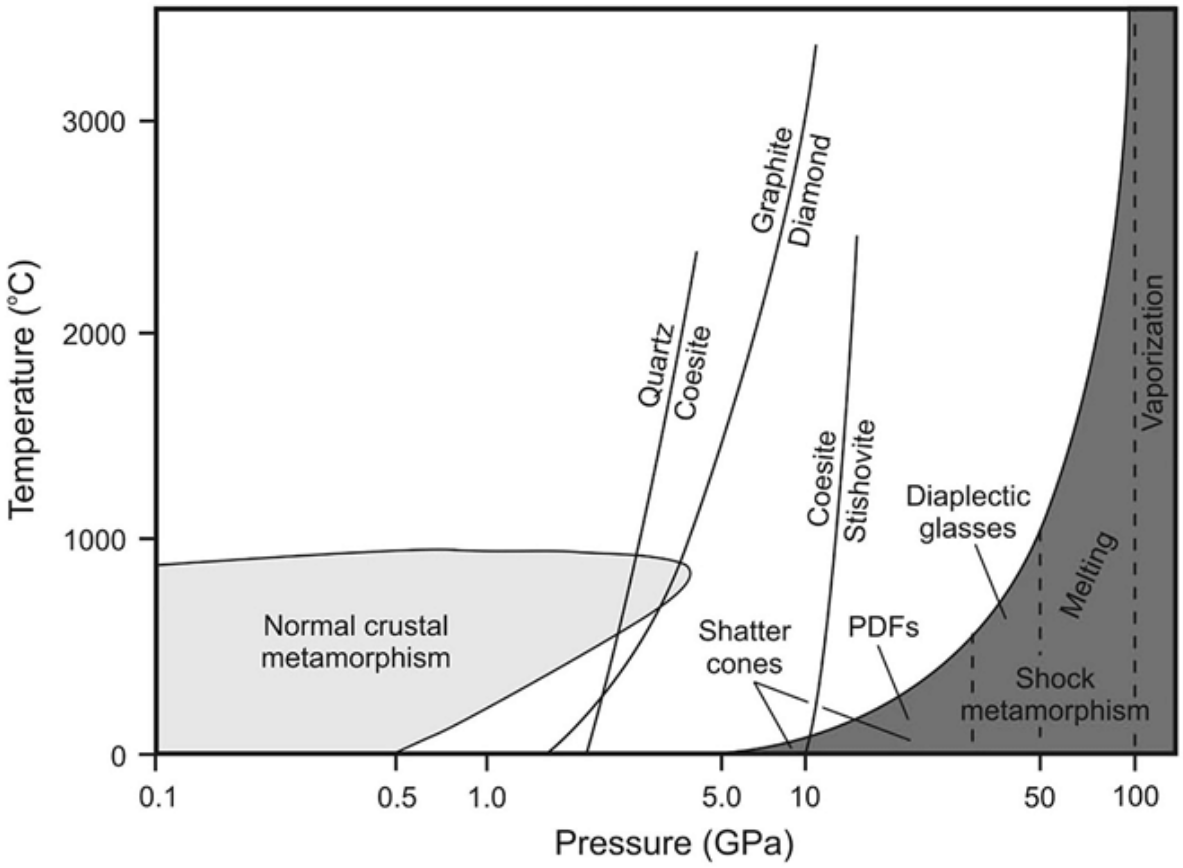

Figure 4.14. Pressure-Temperature diagram showing conditions for conventional metamorphism on the left and shock metamorphism on the right (modified after French 1998).

Chapter 5. Discussion and Conclusion

This study builds upon previous field, drill-core, and shock petrological studies in order to develop a hydrocode numerical model for the Wetumpka impact structure. The present model used iSALE-2D, and there was a special focus of the modeling on the development of the extensively collapsed southern sector of the rim, which had a dominant role in the formation of the crater-infill sequence. Simulations for different impact velocities, water depth, and sediment thickness were performed in order to study their effects on the transient and final crater morphology. Results from this study showed that these parameters, when properly selected, strongly affect the transient crater evolution and crater-fill sequence.

The final crater structure, especially the southern rim and the crater infill sequence, predicted by the numerical model closely approximates the observed deformation caused by a 400-m diameter asteroid, impacting at 12km/s (vertical velocity component) on a three-layered target with 62.5m water depth, 200m sediment layer thickness, and granite bedrock (see Annex 1 for material outputs from best-fit model). The split-Brazilian and uniaxial compressive tests were performed to obtain tensile and compressive strength of intact bedrock for the damage model, used to estimate the material cohesion and friction angle. The number of samples prepared for these mechanical tests was limited to the accessibility of intact rock outcrops.

Simulations with different impact scenarios produced craters with varying dimensions and distribution of target materials comprising the rims and proximal ejecta area. Initial assessment of data was based on the variation of crater dimensions, acting as the first "filter" of data. The comparison between the two impact velocitites conditions (12km/sec and 20km/sec) showed that the slower impact produced a crater with more realistic dimensions of depth and diameter,

narrowing down the number of simulations by half. Then, considering the focus of this study as the southwestern collapsed rim, which is the source for a significant part of the crater fill content, the choice of the best fit model was mainly based on the rim area. Therefore, composition, distribution of target material, and processes, such as emplacement of proximal ejecta and collapse of material, were taken into account while analyzing the rim area.

The final choice and definition of the best fit model considered the average crater diameter of 5 km, the lower amount of crystalline material as proximal ejecta, and the higher amount of sedimentary material comprising the rims and crater wall. These choices correlated well with available geological data. For instance, it was observed that thicker sediment layer scenarios resulted in a rim with progressively higher amounts of sedimentary material, but the choice of 200 meters instead of 300 meters of sediment was supported by drill core data from the surrounding area. Without this critical information, the choice of sediment thickness would be less accurate, comprising a wider possible interval of values. This means that the correlation of the computational model with geological data is valuable for validating the model. However, it does not mean that this study reached the perfect interpretation of the impact scenario. The constant validation of the model basically narrows the spectrum of possibilities that future studies may improve. For example, Ormö et al. (2002) used numerical simulations in addition to facies analysis of Lockne crater filling sediments, reaching a minimum and maximum possible water depth value at the time of the impact. Shuvalov and Trubestkaya (2002), after modeling the formation of Mjølnir, Lockne, and Eltanin craters at different water depths, compared the results to experimental data obtained underwater nuclear explosions. Geological characterization and laboratory experiments strongly support and refine modeling results as a powerful source of data for comparison and validation of the model. In Ormö et al. (2010), the authors compared previous publications on resurge deposits

from Lockne, Tvären, and Chesapeake Bay craters with results from low-velocity impact experiments and hydrocode simulations analyzing the effect of impact angle and target water depth. Among other conclusions, the authors found that in the case of oblique impacts and targets with varied water depth (which is the case of Wetumpka crater), the resurge becomes strongly asymmetrical, significantly affecting the sediment deposition. For Wetumpka studies, the model validation is mainly based on field and drill core information, with experiments being focused on the calibration of material physical parameters. However, low-velocity impact experiments would provide valuable information for our understanding of marine impacts, and it is the aim of future work.

The numerical model of Wetumpka formation predicts the presence of crystalline basement rocks in the crater rim and the proximal ejecta. However, as anticipated from the observed geology of the southern rim and basement material in the crater-infill sequence, the crystalline component was not enough to form a crystalline-on-sedimentary flap. The model describes an overturned sedimentary strata at the rim (also confirmed by drill-core and field observations near the remnants of the southern crater rim), an 'ejecta emplacement tsunami' driven by the bombardment from the ejecta curtain, transient crater rebound followed by slumping of crystalline and sedimentary material into the crater floor. The final crater predicted by the numerical model does not exhibit a central uplift, which is consistent with the current understanding of the impact structure. Finally, the numerical simulations also indicate pressures consistent with shock petrological studies. Although temperature peaks reach more than 5,000 K, the pressure seems to be a more determinant factor on the appearance of shock features, as the transition between different shock features occurs at specific pressure values, but over wide temperature intervals (Fig 4.4). The pressure and

temperature peaks reached by the Wetumpka impact reach the zone of diapletic glasses formation, according to figure 4.4. However, it was not identified by the petrographic analysis to date.

The collapse of sedimentary material from the rims towards the crater's center seems to be a significant process for Wetumpka's crater development. Besides being a significant source of sediments to the crater fill, it could have been the main trigger for the collapse of the southwestern section of the rim, which was possibly also affected by the returning seawater (discussed below). Moreover, the collapse of sedimentary material from rims connects the numerical model with the field and drill-core observations. For instance, the drill core that penetrates through the trans-crater slide revealed large sedimentary blocks with inverted stratigraphy, suggesting that this was part of the sedimentary rim flap, collapsed into the crater cavity.

Although the present iSALE simulations do not predict the development of concentric normal faulting surrounding the impact structure and the possible subsequent formation of terraces, this is a typical process during crater formation and can trigger the slump of material from rims to the center of the structure. Geological mapping of the Wetumpka crater shows concentric marginal faulting associated with the structure's rim (Fig. 2.2), suggesting the existence of planes of weakness that could have contributed to the collapse of the southwestern section. Consistently, the model results show brittle deformation near the surface over a distance of about 1 km from the crater rims, illustrated by the pattern of calculated damage values (Fig 4.5), supporting the possibility of faulting development surrounding the crater cavity. The development of these faults could also be one of the possible origins of Wetumpka's exterior disturbed terrain, which appears to mimic part of the "annular trough," an extensively slumped feature surrounding the excavated crater in the Chesapeake Bay impact structure (King and Ormö, 2011; King et al., 2015).

Despite the significant difference in size, Wetumpka and Chesapeake Bay (85 km) structures share some similarities, such as the target sequence, comprised of a metamorphic basement overlaid by unconsolidated sediments and seawater. Modeling studies on the Chesapeake Bay crater (Collins & Wunemann, 2005; Kenkmann et al., 2009) consider the same three-layer target used in the model presented here and predict a deep basin surrounded by a shallower outer basin. The inner basin displays an evident central uplift, is filled with inwardly collapsed sediments, and is limited by a ring of the uplifted basement. The outer part, or "annular trough," is a shallower basin where deformation is confined to the sediment layer. The model is validated against drill core descriptions and seismic data, which leads to the assumption that the drill cores, like in Wetumpka, do not reach the crater floor. Although there is a possible connection between Wetumpka's exterior terrain with the "annular trough" in the Chesapeake Bay crater, the model presented here does not show the development of a central uplift, a function of impactor size, nor an outer shallower basin. The latter could be attributed to the fact that the Chesapeake Bay model considers a sedimentary layer relatively strong in the intact state but as very weak when damaged (Collins and Wünnemann, 2005), which gives a fluid-like behavior to the sediment layer during the cratering process. In conclusion, the main similarities between both models seem to be regarding the target profile and the inward collapse of material from the rims.

In all simulations, the collapse of sedimentary material from the rims is preceded by a slide of crystalline target material during structural accommodation of crater cavity in the early modification stage. This would form a lower crater-fill layer with more crystalline content. Although all drill cores discussed in this study penetrate just into the upper sedimentary part of the crater fill, gravity modeling studies (Robbins et al., 2011) predict this lower unit of higher density,

which is likely composed of crystalline bedrock slump blocks. Again, the model is validated by geological and geophysical data.

After such a high energy impact, the generated tsunami waves are expected to travel several tenths of kilometers before water begins to return towards the crater region, bringing seafloor sediments and ejecta material back into the central cavity. In the model, the moment of return of the seawater to the crater region cannot be precisely predicted since it defined by the mesh dimensions, meaning that the seawater is reflected back into the crater direction when it reaches the end of the mesh, at about 13 km from the center of the crater. A different code focused on fluid dynamics would be helpful for a precise estimation of the resurge timing.

It is important to note that there are several areas of improvement. First, none of the existing drill cores within the crater were deep enough to encounter the crystalline basement. Deeper drill-core studies will be useful to validate model predictions and geological estimates regarding the absence of the central uplift. Second, due to the nature of the hydrodynamic code, modeling large time-scale processes such as tsunami and resurge is difficult. Modeling resurge driven sediment transport back into the crater would require specialized computational fluid dynamics software. Third, the damage and strength models used in this work do not account for the anisotropic laminated nature of the schist bedrock. Recently, the effect of material anisotropy on the crater structure has been studied (Agarwal et al., 2019; Hopkins et al., 2019) experimentally. However, material anisotropy needs to be implemented and extensively validated using iSALE-2D before it can be used for predicting crater evolution.

Finally, the iSALE-2D model simulated an idealized target with axisymmetric assumption. As such, the model cannot account for the continental slope and the change in water depth and sediment thickness across the crater. This can be resolved with three-dimensional simulations

using iSALE-3D supported by low-velocity impact experiments. These aspects will be reserved for future work.

Despite its limitations outlined above, the results from the numerical model were consistent with the field, drill-core, and petrological studies. Overall, the model predicted the crater shape and evolution with reasonable accuracy. The model identified the sequence of events and their role in the final crater shape. Finally, the model also explained the crater infill and rim modification sequences observed in drill core and gravity studies. The current study represented the first assessment of the Wetumpka crater's formation through a numerical perspective and was submitted for publication. The manuscript is now being refined according to editors' recommendations for improvement (De Marchi et al., 2021).

References

Adrian, D.R., King, Jr., D.T., and Ormö, J. 2018. Resurge gullies and "inverted sombrero" morphology, Flynn Creek impact structure, Tennessee, Meteoritics & Planetary Science, 54, 11, (2758-2768).

Agarwal, A., Poelchau, M. H., Kenkmann, T., Rae, A., and Ebert, M. 2019. Impact experiment on gneiss: the effects of foliation on cratering process. Journal of Geophysical Research: Solid Earth 124,12:13532-13546.

Arndt, J., Hummel, W., Gonzales-Cabeza, I., 1982. Diaplectic labradorite glass from the Manicouagan impact crater. I. Physical properties, crystallization, structural and genetic implications. Physics and Chemistry of Minerals 8, 230–239.

ASTM Standard D3967-08, 2008. Standard test method for splitting tensile strength of intact rock core specimens. ASTM International, West Conshohocken, PA, DOI: 10.1520/D3967-16.

ASTM Standard D7012-14, 2014. Standard Test Methods for Compressive Strength and Elastic Moduli of Intact Rock Core Specimens under Varying States of Stress and Temperatures. ASTM International, West Conshohocken, PA, DOI: 10.1520/D7012-14E01.

Bottke, W. F., Vokrouhlický, D., Ballouz, R. L., Barnouin, O. S., Connolly Jr, H. C., Elder, C., ... & Lauretta, D. S. 2020. Interpreting the cratering histories of Bennu, Ryugu, and other spacecraft-explored asteroids. The Astronomical Journal, 160(1), 14.

Bunch, T.E., 1968. Some characteristics of selected minerals from craters. In: French, B.M., Short, N.M. (Eds.), Shock metamorphism of natural materials. Mono Book Corp, Baltimore, MD, pp. 413–422.

Bunch, T.E., Cohen, A.J., Dence, M.R., 1967. Natural terrestrial maskelynite. American Mineralogist 52, 244–253.

Carroll, M. M. and Holt, A. C. 1972. Static and dynamic pore-collapse relations for ductile porous materials. Journal of Applied Physics, 43(4):1626–1636.

Chao, E.C.T., Shoemaker, E.M., Madsen, B.M., 1960. First natural occurrence of coesite. Science 132, 220–222.

Chinchalkar N. 2019. Provenance of a boulder-bearing impact breccia from surface outcrops and a drill-core from the Wetumpka impact structure, Elmore County, Alabama. M.S. thesis, Auburn University, Auburn, Alabama, USA.

Collins G. S., Melosh H. J., and Ivanov B. A. 2004. Modeling damage and deformation in impact simulations. Meteoritics & Planetary Science 39:217–231.

Collins, G. S., and Wünnemann, K. 2005. How big was the Chesapeake Bay impact? Insight from numerical modeling. Geology, 33(12), 925-928.

Davison, T., & Collins, G. S. 2007. The effect of the oceans on the terrestrial crater size-frequency distribution: Insight from numerical modeling. Meteoritics & Planetary Science, 42(11), 1915-1927.

De Marchi, L., Agrawal, V., King Jr, D. T., Ormö, J. 2021. Numerical Simulations of the formation of the critical, ocean-facing, southern sector of the Wetumpka impact structure constrained by field and drill-core data. [Manuscript submittd for publication].

Dietz, R.S., 1959. Shatter cones in cryptoexplosion structures (meteorite impact?). Journal of Geology 67, 496–505.

Dietz, R.S., 1963a. Cryptoexplosion structures: a discussion. American Journal of Science 261, 650–664.

Dietz, R.S., 1963b. Astroblemes: ancient meteorite-impact structures on the Earth. In: Middlehurst, B.M., Kuiper, G.P. (Eds.), The Moon, meteorites, and comets. University of Chicago Press, Chicago IL, pp. 285–300.

Dietz, R.S., 1968. Shatter cones in cryptoexplosion structures. In: French, B.M., Short, N.M. (Eds.), Shock Metamorphism of Natural Materials. Mono Book Corp, Baltimore, MD, pp. 267–285.

Dvorak, U., 1969. Stosswellenmetamorphose des Anorthosits vom Manicouagan Krater, Quebec, Canada. Contributions to Mineralogy and Petrology 24, 306–347.

Engelhardt, W.V., Stöffler, D., 1965. Spaltflächen im Quarz als Anzeichen für Einschläge grosser Meteoriten. Naturwissenschaften 17, 489–490.

Fackelman, S.P., Morrow, J.R., Koeberl, C., McElvain, T.H., 2008. Shatter cone and microscopic shock-alteration evidence for a post-Paleoproterozoic terrestrial impact structure near Santa Fe, New Mexico, USA. Earth and Planetary Science Letters 270, 290–299.

Feignon, J. G., Ferrière, L., Leroux, H., and Koeberl, C. 2020. Characterization of shocked quartz grains from Chicxulub peak ring granites and shock pressure estimates. Meteoritics & Planetary Science 1-18.

Ferrière, L., and Osinski, G. R. 2013. Shock metamorphism. In Impact cratering: processes and products, first edition. Edited by Osinski G. R. and Pierazzo E. Chinchester, UK: Blackwell Publishing Ltd. pp. 106-124.

Ferrière, L., Morrow, J. R., Amgaa, T., and Koeberl, C. 2009. Systematic study of universal-stage measurements of planar deformation features in shocked quartz: implications for statistical significance and representation of results. Meteoritics & Planetary Science 44: 925–940.

Ferrière, L., Osinski, G., 2009. Characterization of shock-metamorphic effects in quartz from sandstones at the Houghton impact structure, Canada (abstract). Meteoritics and Planetary Science 44, A68.

French, B. M. 1998 Traces of catastrophe, a handbook of shock metamorphic effects in terrestrial impact structures. Houston, Texas: Lunar and Planetary Institute. 120 p.

French, B. M., & Koeberl, C. 2010. The convincing identification of terrestrial meteorite impact structures: What works, what doesn't, and why. Earth-Science Reviews, 98(1-2), 123-170.

French, B.M., Cordua, W.S., Plescia, J.B., 2004. The Rock Elm meteorite impact structure, Wisconsin: geology and shock-metamorphic effects in quartz. Bulletin of the Geological Society of America 116, 200–218.

French, B.M., Koeberl, C., Gilmour, I., Shirey, S.B., Dons, J.A., Naterstad, J., 1997. The Gardnos impact structure, Norway: petrology and geochemistry of target rocks and impactites. Geochimica et Cosmochimica Acta 61, 873–904.

Gibson, R.L., Reimold, W.U., Wallmach, T., 1997. Origin of pseudotachylite in the lower Witwatersrand Supergroup, Vredefort Dome (South Africa): constraints from metamorphic studies. Tectonophysics 283, 241–262.

Grieve, R.A.F., 1991. Terrestrial impact: the record in the rocks. Meteoritics 26, 175–194.

Grieve, R.A.F., 2001. The terrestrial cratering record. In: Peucker-Ehrenbrink, B., Schmitz, B. (Eds.), Accretion of Extraterrestrial Matter throughout Earth's History. Kluwer Academic/Plenum Publishers, New York, NY, pp. 379–402.

Grieve, R.A.F., Langenhorst, F., Stöffler, D., 1996. Shock metamorphism of quartz in nature and experiment: II. Significance in geoscience. Meteoritics and Planetary Science 31, 6–35.

Grieve, R.A.F., Shoemaker, E.M., 1994. The record of past impacts on Earth. In: Gehrels, T. (Ed.), Hazards Due to Comets and Asteroids. University of Arizona Press, Tucson, AZ, pp. 417–462.

Hargraves, R.B., Cullicott, C.E., Deffeyes, K.S., Hougen, S., Christiansen, P.P., Fiske, P.P., 1990. Shatter cones and shocked rocks in southwestern Montana: the Beaverhead impact structure. Geology 18, 832–834.

Heider E. S. 2015. Early modification stage dynamics of shallow crater-filling units, Wetumpka impact structure, Alabama. M.S. thesis, Auburn University, Auburn, Alabama, USA.

Heider, E. S., and King, Jr., D. T. 2016. Early modification stage emplacement of shallow crater-filling units, Wetumpka impact structure, Alabama: Gulf Coast Association of Geological Societies Transactions 66:231-249.

Herrmann, W. 1969. Constitutive equation for the dynamic compaction of ductile porous materials. Journal of Applied Physics, 40(6):2490–2499.

Hildebrand, A.R., Penfield, G.T., Kring, D.A., Pilkington, M., Camargo, Z.A., Jacobsen, S.B., Boynton, W.V., 1991. Chicxulub crater: a possible Cretaceous–Tertiary boundary impact crater on the Yucatan Peninsula, Mexico. Geology 19, 867–871.

Holm-Alwmark, S., Ferrière, L., Alwmark, C., and Poelchau, M. H. 2018. Estimating average shock pressures recorded by impactite samples based on universal stage investigations of planar deformation features in quartz - sources of error and recommendations. Meteoritics & Planetary Science 53: 110-130.

Holsapple, K. A. 2008. Porous Material Models for Impact Studies. In Lunar and Planetary Institute Science Conference Abstracts, volume 39 of Lunar and Planetary Institute Science Conference Abstracts, pages 2257–+.

Hopkins, R. T., Osinski, G. R., and Collins, G. S. 2019. Formation of complex craters in layered targets with material anisotropy. Journal of Geophysical Research: Planets 124: 349-373.

Howard, K.A., Offield, T.W., 1968. Shatter cones at Sierra Madera, Texas. Science 162, 261–265.

Hoyt, W.G., 1987. Coon Mountain Controversies: Meteor Crater and the Development of the Impact Theory. University of Arizona Press, Tucson, AZ. 442 pp.

Ivanov B. A., Deniem D., and Neukum G. 1997. Implementation of dynamic strength models into 2D hydrocodes: Applications for atmospheric breakup and impact cratering. International Journal of Impact Engineering 20:411–430.

Johnson R.C. 2007. Wetumpka impact structure modeled as the exposed remains of a large, shallow-water, marine-target impact crater for analysis and interpretation of two drill cores taken from near the structure's geographic center. M.S. thesis, Auburn University, Auburn, Alabama, USA.

Kenkmann, T., Collins, G. S., Wittmann, A., Wünnemann, K., Reimold, W. U., and Melosh, H. J. 2009. A model for the formation of the Chesapeake Bay impact crater as revealed by drilling and numerical simulation. Geological Society of America Special Papers, 458, 571-585.

Kenkmann, T., Poelchau, M. H., & Wulf, G. 2014. Structural geology of impact craters. Journal of Structural Geology, 62, 156-182.

Kerley, G. 1992. Cth equation of state package: Porosity and reactive burn models. Technical report.

King, Jr., D. T., and Ormö, J. 2011. The marine-target Wetumpka impact structure examined in the field and by shallow core-hole drilling. In Analogs for planetary exploration: geological society of America special paper 483, edited by Garry, W. B. and Bleacher, J. E. pp. 287–300.

King, Jr., D. T., Morrow, J. R., Petruny, L. W., and Ormö, J. 2015. Surficial polymict impact breccia unit, Wetumpka impact structure, Alabama: shock levels and emplacement

mechanism. In Large meteorite impacts and planetary evolution V, edited by Osisnki, G. R. and Kring, D. A. Boulder, CO: Geological Society of America pp. 149-164

King, Jr., D. T., Neathery, T. L., Petruny, L. W. Koeberl, and C., Hames, W. 2002. Shallow-marine impact origin of the Wetumpka structure (Alabama, USA). Earth and Planetary Science Letters, 202:541–549, 09.

King, Jr., D. T., Ormö, J., Petruny, L. W., and Neathery, T. L. 2006. Role of water in the formation of the late cretaceous Wetumpka impact structure, inner gulf coastal plain of Alabama, USA. Meteoritics & Planetary Science, 41:1625–1631.

Knowles, D. B., Reade, Jr., H. L., and Scott, J. C. 1960, Geology and ground-water resources of Montgomery County, Ala., with special reference to the Montgomery area. Alabama Geological Survey Bulletin 68. Montgomery: pp. 11-48.

Koeberl, C., 1998. Identification of meteoritic component in impactites. In: Grady, M.M., Hutchison, R.,McCall, G.J.H., Rothery, D. (Eds.), Meteorites: Flux with Time and Impact Effects. Geological Society, London, Special Publications, vol. 140, pp. 133–153.

Koeberl, C., 2007. The geochemistry and cosmochemistry of impacts. In: Davis, A. (Ed.), Treatise of Geochemistry, vol. 1. Elsevier, New York, NY, pp. 1.28.1–1.28.52. doi:10.1016/B978-008043751-4/00228-5. online edition.

Koeberl, C., Reimold, W.U., Brandt, D., 1996. Red Wing Creek structure, North Dakota: petrographical and geochemical studies, and confirmation of impact origin. Meteoritics and Planetary Science 31, 335–342.

Lindström, M., Shuvalov, V., and Ivanov, B. 2005. Lockne crater as a result of marine-target oblique impact. Planetary and Space Science 53, 8:803-815.

Markin J. K. 2015. Lithofacies analysis of AU scientific drill cores 09-03 and 09-04, Wetumpka impact structure, Elmore County, Alabama. M.S. thesis, Auburn University, Auburn, Alabama, USA.

Markin, J.K., and King, D.T., Jr., 2012, Wetumpka impact structure's resurge chalk deposits – Insights from x-ray computed tomography: Gulf Coast Association of Geological Societies Transactions, v. 62, p. 265-271.

Marvin, U.B., 1990. Impact and its revolutionary implications for geology. In: Sharpton, V.L., Ward, P.D. (Eds.), Global Catastrophes in Earth History. Special Paper, vol. 293. Geological Society of America, Boulder, CO, pp. 147–154.

Marvin, U.B., 1999. Impact from space: the implications for uniformitarian geology. In: Craig, G.Y., Hull, J.H. (Eds.), James Hutton — Present and Future. Geological Society of London Special Publication, vol. 150. Geological Society, London, pp. 89–117.

Masaitis, V.L., 1998. Popigai crater: origin and distribution of diamond-bearing impactites. Meteoritics and Planetary Science 33, 349–359.

Melosh H. J., Ryan E. V., and Asphaug E. 1992. Dynamic fragmentation in impacts: Hydrocode simulation of laboratory impacts. Journal of Geophysical Research 97:14,735–14,759.

Melosh, H. J. 2007. A hydrocode equation of state for SiO2, Meteoritics and Planetary Science 42: 2079-2098.

Melosh, H.J., 1989. Impact Cratering: A Geologic Process. Oxford University Press, New York, NY. 245 pp.

Milton, D.J., 1977. Shatter cones—an outstanding problemin shockmechanics. In: Roddy, D.J., Pepin, R.O., Merrill, R.P. (Eds.), Impact and Explosion Cratering: Planetary and Terrestrial Applications. Pergamon Press, New York, NY, pp. 703–714.

Neathery, T. L., Bentley, R. D., Lines, G. C. 1976. Cryptoexplosive structure near Wetumpka, Alabama. Geological Society of America Bulletin, 87:567.

Nelson A.I., 2000. Geological mapping of Wetumpka impact crater area, Elmore County, Alabama. M.S. thesis, Auburn University, Auburn, Alabama, USA.

Oberbeck, V. R. 1975. The role of ballistic erosion and sedimentation in lunar stratigraphy. Reviews of Geophysics and Space Physics, 13:337–362.

Ormö J. and Muinonen P. 2000. Impact craters as indicators for oceanic phases on Mars (abstract #1266). 31st Lunar and Planetary Science Conference

Ormö J., Dohm J. M., Ferris J. C., Lepinette A., and Fairén A. G. 2004. Marine-target craters on Mars? An assessment study. Meteoritics & Planetary Science 39:333–346.

Ormö, J., Lepinette, A., Sturkell, E., Lindström, M., Housen, K. R., Holsapple, K. A. 2010. Water resurge at marine-target impact craters analyzed with a combination of low-velocity impact experiments and numerical simulations. Geological Society of America Special Papers, 465, 81-101.

Ormö, J., Shuvalov, V. V., & Lindström, M. 2002. Numerical modeling for target water depth estimation of marine-target impact craters. Journal of Geophysical Research: Planets, 107(E12), 3-1.

Ormö, J., Sturkell, E., Lindström, M. 2007. Sedimentological analysis of resurge deposits at the Lockne and Tvären craters: clues to flow dynamics. Meteoritics and Planetary Science 42:1929-1943.

Ormö, J., Sturkell, E., Horton, J.W., Jr., Powars, D.S., and Edwards, L.E. 2009. Comparison of clast frequency and size in the Exmore sediment-clast breccia, Eyreville and Langley cores, Chesapeake Bay impact structure: clues to the resurge process. Edited by Gohn, G. S., Koeberl, C., Miller, K. G., and Reimold, W.U. The ICDP-USGS deep drilling project in the Chesapeake Bay impact structure: results from the Eyreville coreholes. Boulder, Colorado. Geological Society of America Special Paper 458, pp. 617-632.

Petruny, L. W. King, Jr., D. T., 2018. Distal ejecta particles in marine resurge deposits (Mooreville chalk), Wetumpka impact structure, Alabama. (abstract #2704) 49th Lunar and Planetary Science Conference.

Pierazzo, E. 2006. Numerical Modeling of Impact Cratering. Planetary Science Institute, Tucson, AZ, USA.

Pierazzo, E., and Collins, G. 2004. A Brief Introduction to Hydrocode Modeling of Impact Cratering. In: Dypvik H., Burchell M.J., Claeys P. (eds.) Cratering in Marine Environments and on Ice. Impact Studies. Springer, Berlin, Heidelberg.

Plescia, J. 2009. Wetumpka impact structure, Alabama: gravity survey (abstract #1218). 40th Lunar and Planetary Science Conference.

Poelchau, M.H., Kenkmann, T., 2009. Feather textures — a possible shock feature in quartz diagnostic of low shock pressures. Meteoritics and Planetary Science 44, A170.

Reimold, W.U., 2003. Impact cratering comes of age. Science 300, 1889–1890.

Reimold, W.U., Koeberl, C., 2008. Catastrophes, extinctions, and evolution: 50 years of impact cratering studies. Golden Jubilee Memoir of the Geological Society of India, vol. 66, pp. 69–110.

Robbins, E. A., Wolf, L. W., and King, Jr., D. T. 2011. Wetumpka impact structure (Alabama) – a gravity model. (abstract #2732). 42nd Lunar and Planetary Science Conference.

Rodesney S. N. 2014. Provenance and composition of impactite sands; AU drill Core #09-04, Wetumpka impact structure, Alabama. M.S. thesis, Auburn University, Auburn, Alabama, USA.

Schnabel, C., Pierazzo, E., Xue, S., Herzog, G.F., Masarik, J., Cresswell, R.G., di Tada, M.L., Liu, K., Fifield, L.K., 1999. Shock melting of the Canyon Diablo impactor: Constraints from nickel-59 contents and numerical modeling. Science 285, 85–88.

Shoemaker, E.M., Chao, E.C.T., 1961. New evidence for the impact origin of the Ries Basin, Bavaria, Germany. Journal of Geophysical Research 66, 3371–3378.

Shuvalov, V. V., Trubestkaya, I. A. 2002. Numerical modeling of marine target impacts. Solar System Research, 36(5), 417-430.

Sivacugan, N., Das, B.M., Lovisa, J., Patra, C.R. 2014. Determination of c and Φ of rocks from indirect tensile strength and uniaxial compression tests, International Journal of Geotechnical Engineering, 8:1, 59-65, DOI: 10.1179/1938636213Z.00000000053

Stähle, V., Altherr, R., Koch, M., Nasdala, L., 2008. Shock-induced growth and metastability of stishovite and coesite in lithic clasts from suevite of the Ries impact crater (Germany). Contributions to Mineralogy and Petrology 155, 457–472.

Stöffler, D., Langenhorst, F., 1994. Shock metamorphism of quartz in nature and experiment: I. Basic observation and theory. Meteoritics 29, 155–181.

Szabo, M.W., Osborne, W.E., Copeland, C.W., Neathery, T.L. 1988. Geologic map of Alabama, Geological Survey of Alabama, Special Map 220, scale 1:250,000.

Tabares Rodenas P. 2012. Drill-Core and geophysical investigation of the western part of the crystalline rim of Wetumpka impact structure. M.S. thesis, Auburn University, Auburn, Alabama, USA.

Tagle, R., Hecht, L., 2006. Geochemical identification of projectiles in impact rocks. Meteoritics and Planetary Science 41, 1721–1735.

Thompson, S. and Lauson, H. 1972. Improvements in the CHART D radiation-hydrodynamic code III: revised analytic equations of state. Sandia National Laboratory Report, SC-RR-71 0714:113p.

Tillotson, J. H. 1962. Metallic equations of state for hypervelocity impact. Technical Report GA-3216, General Atomic Report.

Villiers, G., King, Jr, D. T., and Marzen, L. J. 2010. A study of candidate marine target impact craters in Arabia Terra, Mars. Meteoritics and Planetary Science 45, Nr 6, 947–964.doi: 10.1111/j.1945-5100.2010.01068.x.

von Dalwigk, I., Ormö, J. 2001. Formation of resurge gullies at impacts at sea: The Lockne crater, Sweden. Meteoritics and Planetary Science 36: 359–369.

Wartho, J. A., van Soest, M.C., King, D.T., Jr., Petruny, L.W. 2012, An (U-Th)/He age for the shallow-marine Wetumpka impact structure, Alabama, USA. Meteoritics & Planetary Science, 47:1243–1255.

Wüunnemann K., Collins G. S., and Melosh H. J. 2006. A strain-based porosity model for use in hydrocode simulations of impacts and implications for transient crater growth in porous targets. Icarus 180:514–527.

Annexes

1. iSALE material outputs from best-fit model

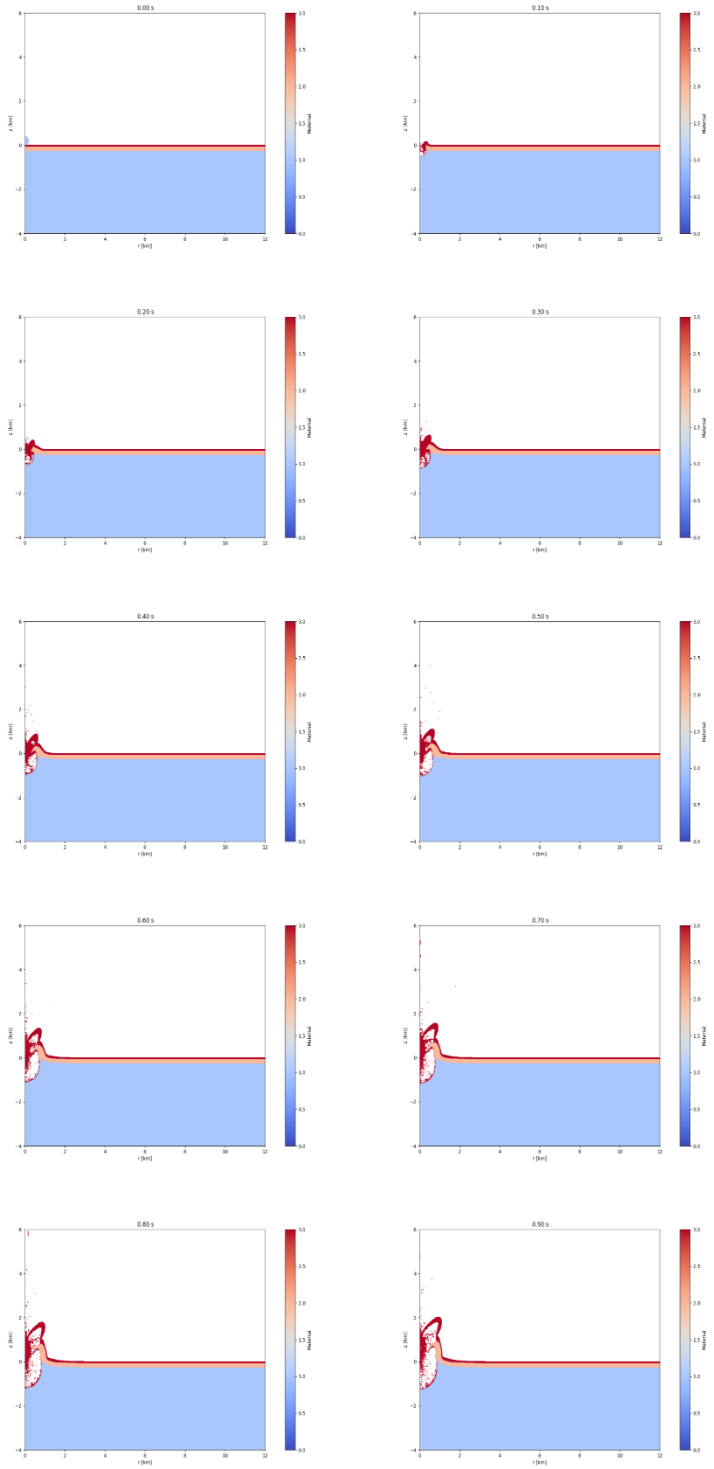

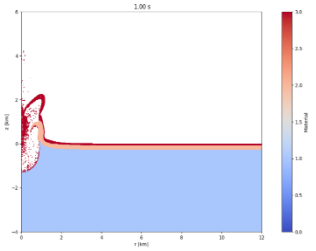
1.00 s
z [km]
r [km]
Material

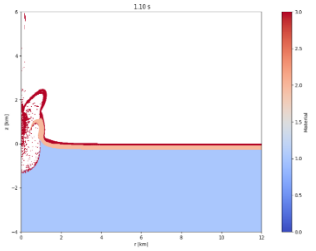
1.10 s
z [km]
r [km]
Material

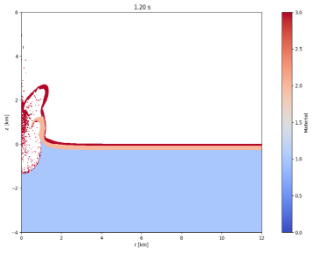
1.20 s
z [km]
r [km]
Material

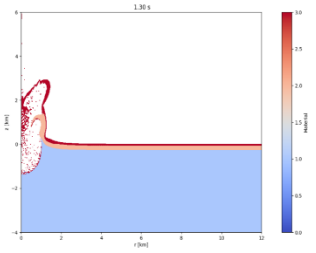
1.30 s
z [km]
r [km]
Material

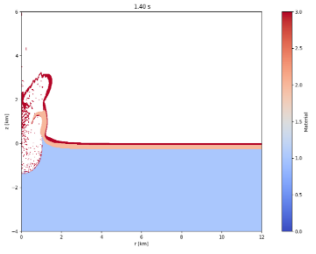
1.40 s
z [km]
r [km]
Material

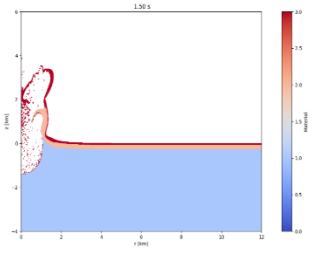
1.50 s
z [km]
r [km]
Material

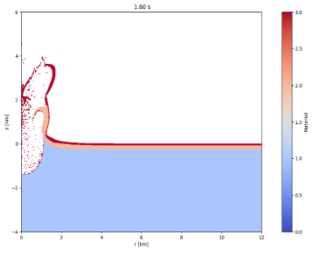
1.60 s
z [km]
r [km]
Material

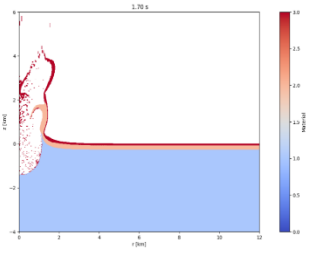
1.70 s
z [km]
r [km]
Material

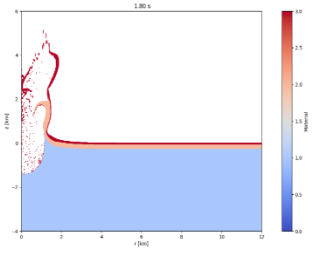
1.80 s
z [km]
r [km]
Material

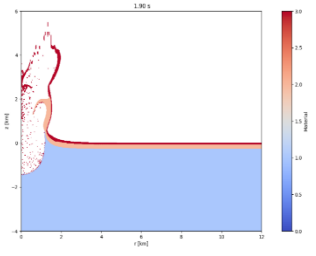
1.90 s
z [km]
r [km]
Material

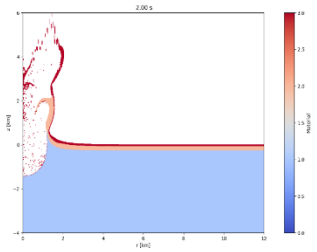
2.00 s
z [km]
r [km]
Material

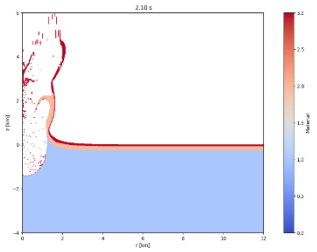
2.10 s
z [km]
r [km]
Material

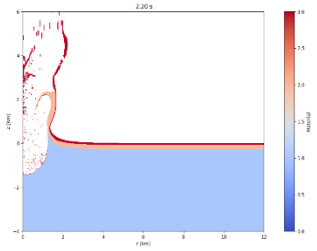
2.20 s
z [km]
r [km]
Material

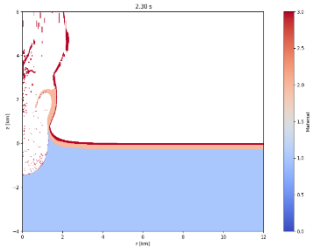
2.30 s
z [km]
r [km]
Material

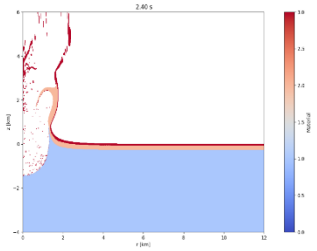
2.40 s
z [km]
r [km]
Material

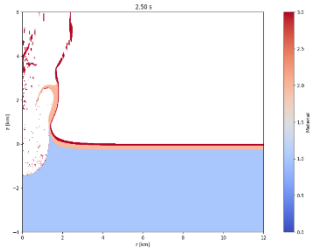
2.50 s
z [km]
r [km]
Material

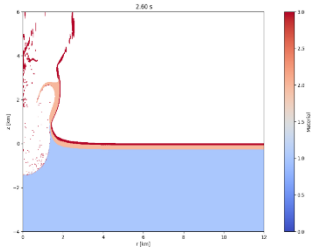
2.60 s
z [km]
r [km]
Material

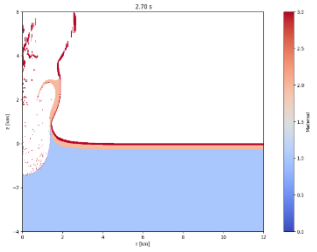
2.70 s
z [km]
r [km]
Material

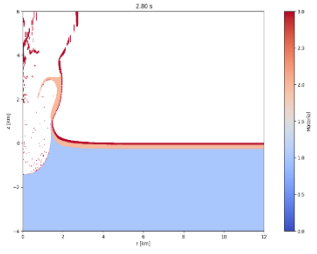
2.80 s
z [km]
r [km]
Material

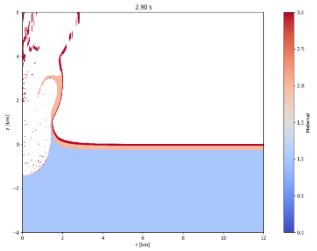
2.90 s
z [km]
r [km]
Material

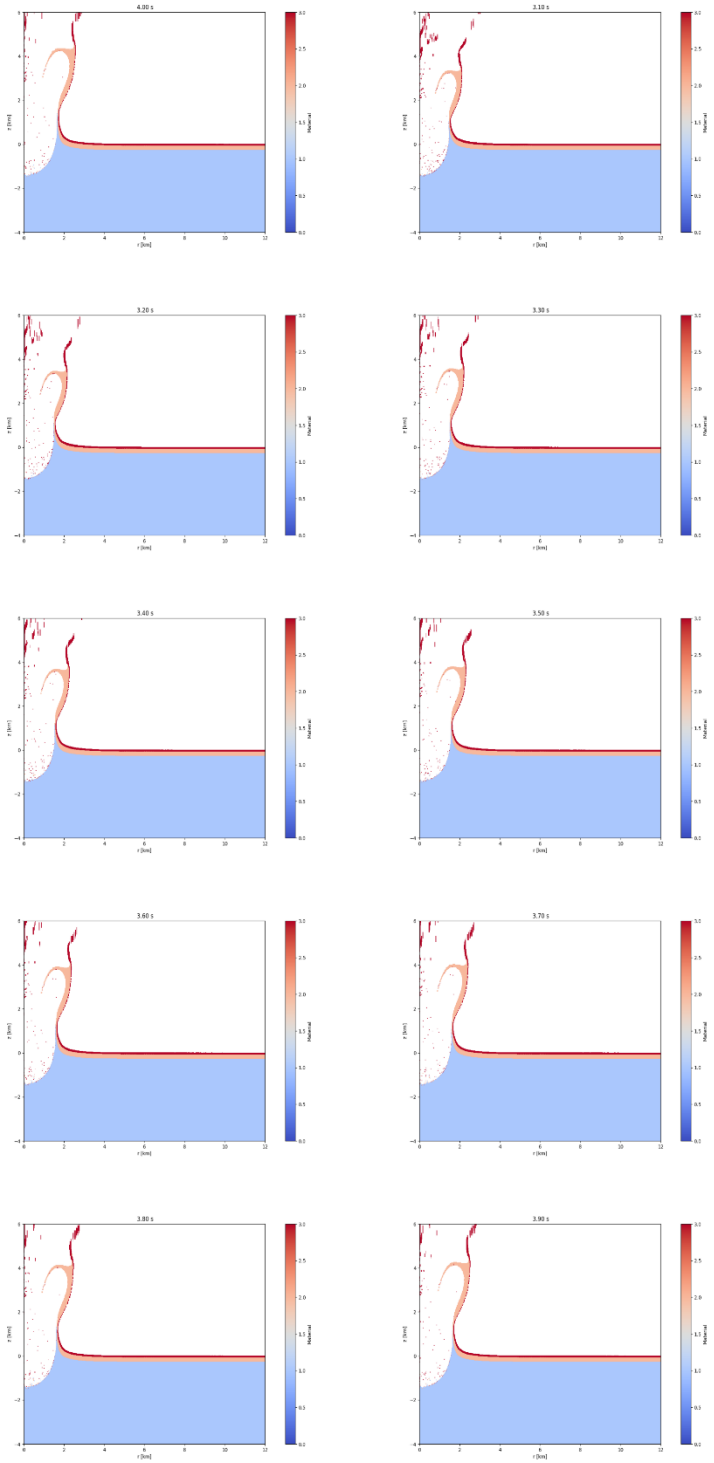
4.00 s
2.10 s
3.20 s
3.30 s
3.40 s
3.50 s
3.60 s
3.70 s
3.80 s
3.90 s

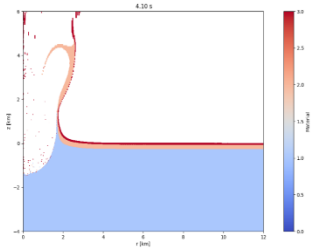
4.10 s
z [km]
r [km]
Material

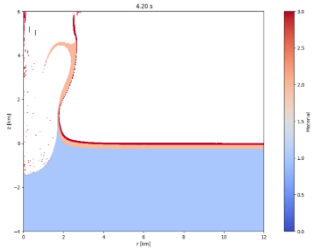
4.20 s
z [km]
r [km]
Material

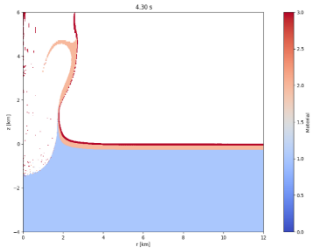
4.30 s
z [km]
r [km]
Material

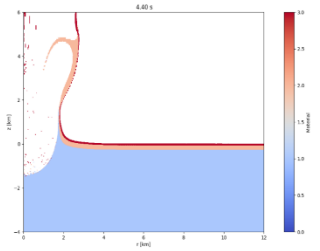
4.40 s
z [km]
r [km]
Material

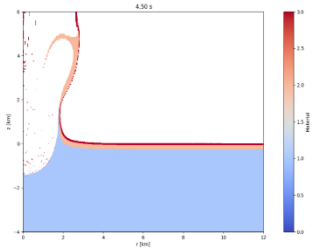
4.50 s
z [km]
r [km]
Material

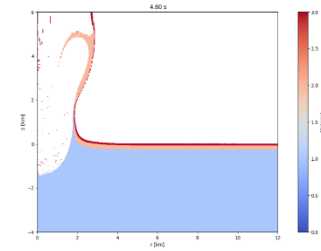
4.60 s
z [km]
r [km]
Material

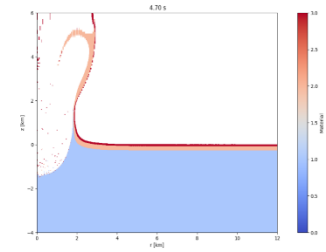
4.70 s
z [km]
r [km]
Material

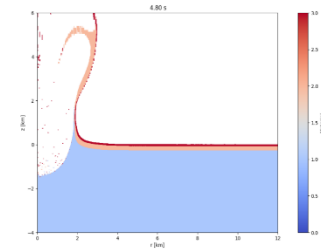
4.80 s
z [km]
r [km]
Material

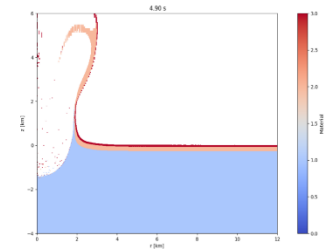
4.90 s
z [km]
r [km]
Material

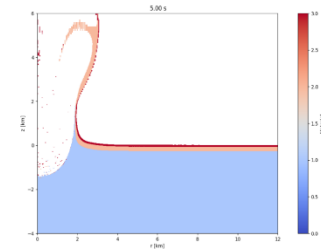
5.00 s
z [km]
r [km]
Material

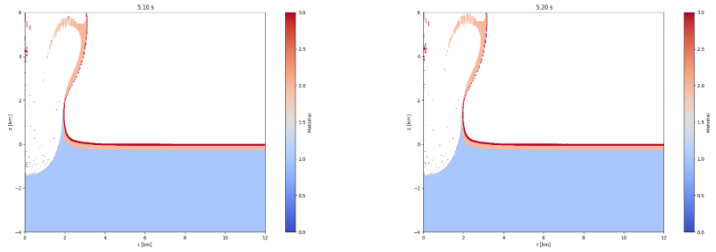
5.10 s
5.20 s

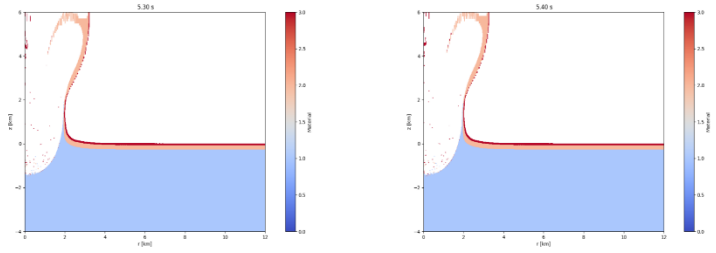
5.30 s
5.40 s

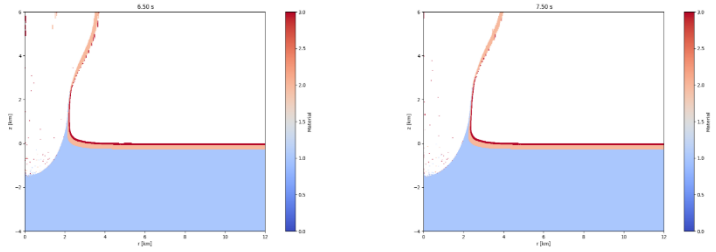
6.50 s
7.50 s

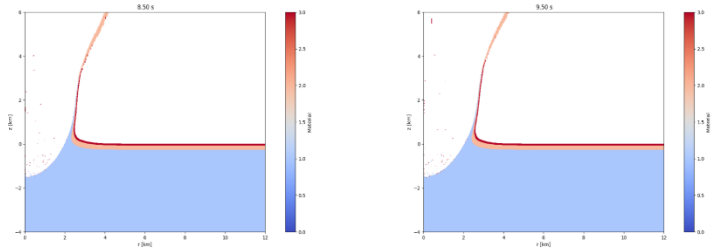
8.50 s
9.50 s

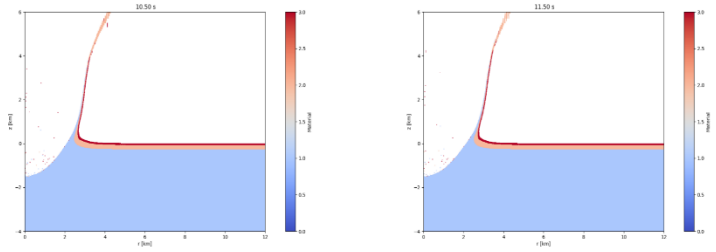
10.50 s
11.50 s

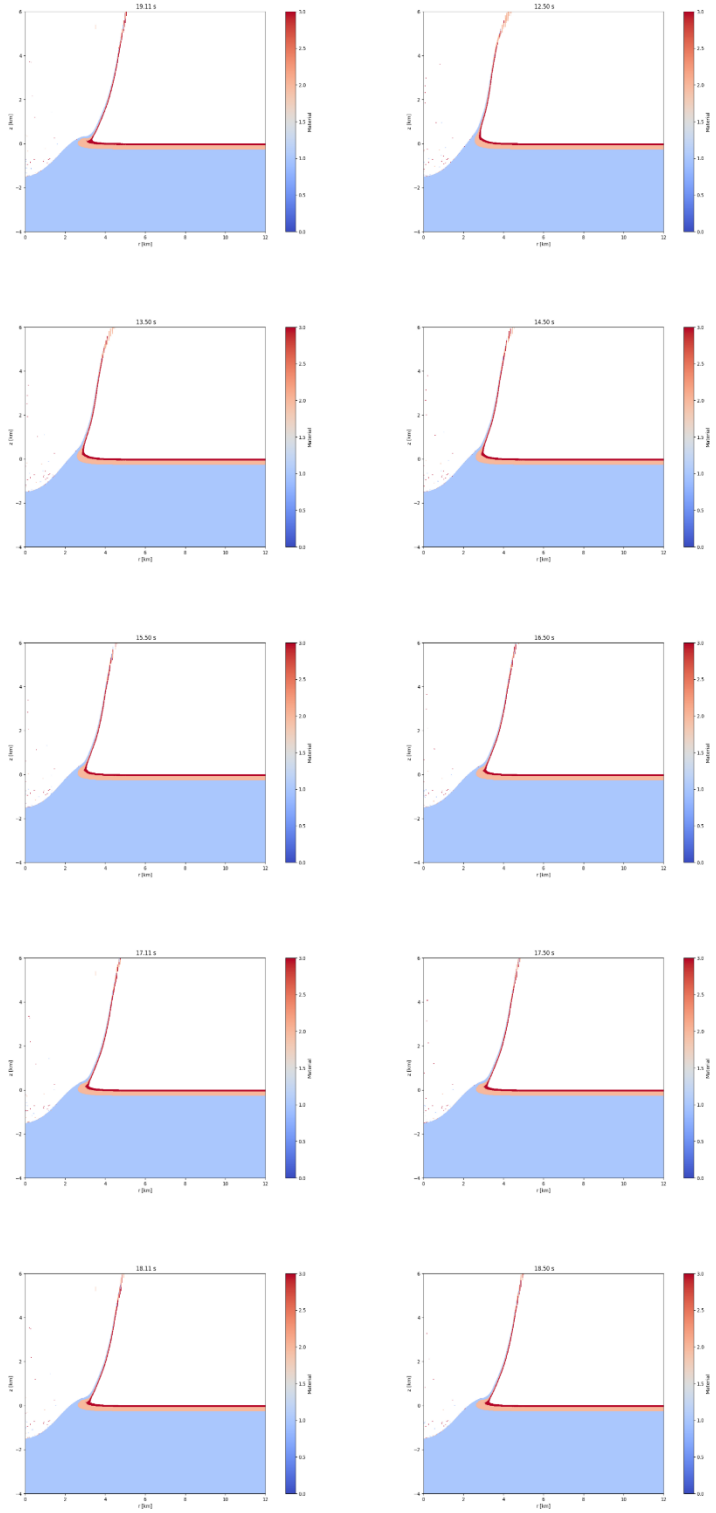
19.11 s
12.50 s
13.50 s
14.50 s
15.50 s
16.50 s
17.11 s
17.50 s
18.11 s
18.50 s

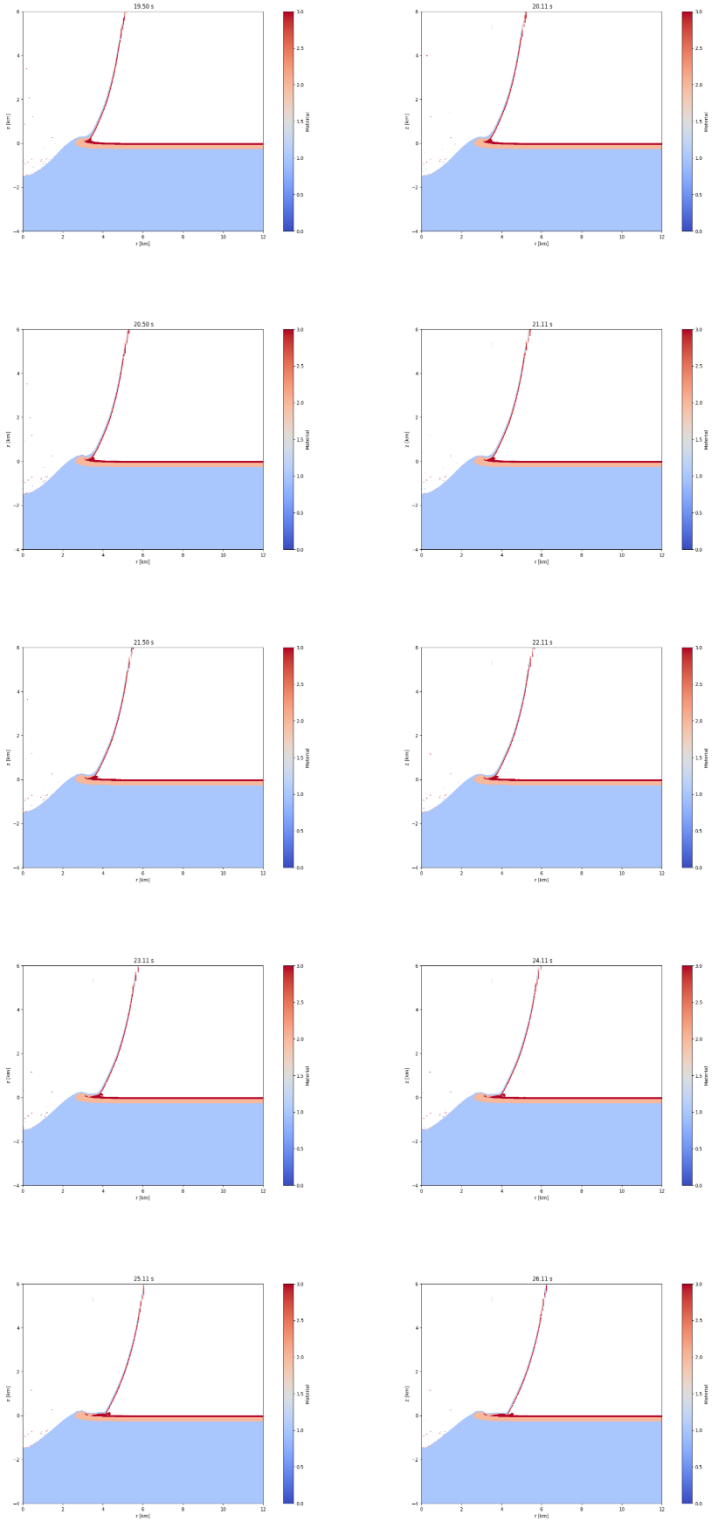
19.50 s
20.11 s
20.50 s
21.11 s
21.50 s
22.11 s
23.11 s
24.11 s
25.11 s
26.11 s

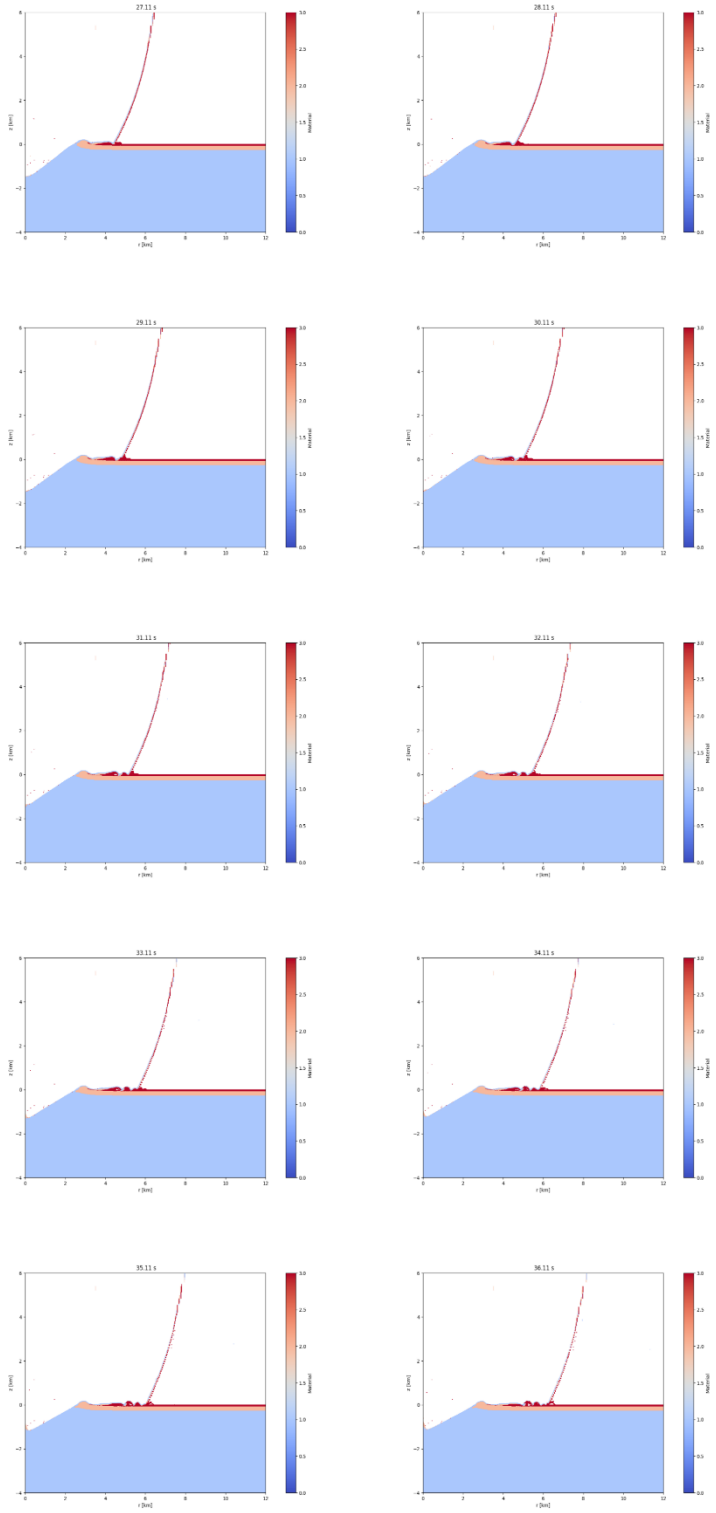
27.11 s
28.11 s
29.11 s
30.11 s
31.11 s
32.11 s
33.11 s
34.11 s
35.11 s
36.11 s

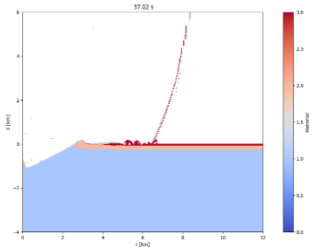
37.02 s
z [km]
r [km]
Material

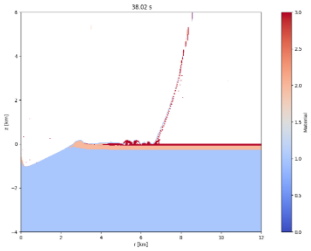
38.02 s
z [km]
r [km]
Material

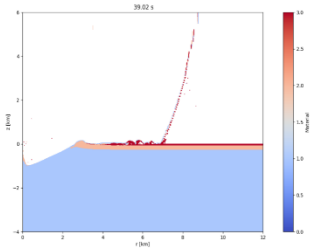
39.02 s
z [km]
r [km]
Material

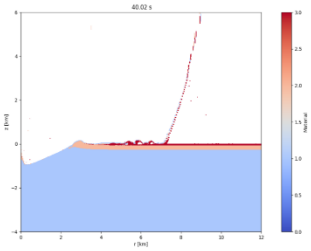
40.02 s
z [km]
r [km]
Material

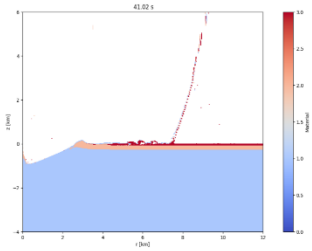
41.02 s
z [km]
r [km]
Material

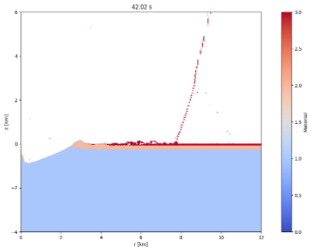
42.02 s
z [km]
r [km]
Material

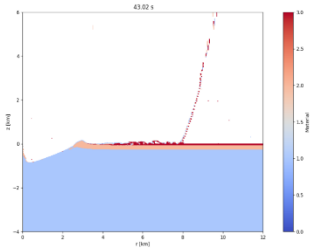
43.02 s
z [km]
r [km]
Material

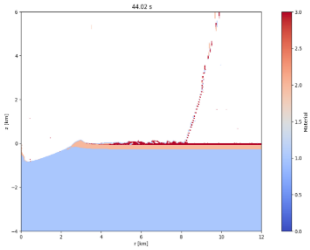
44.02 s
z [km]
r [km]
Material

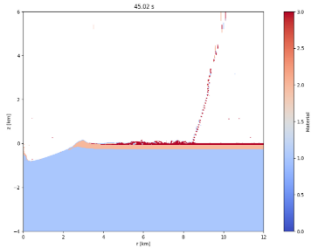
45.02 s
z [km]
r [km]
Material

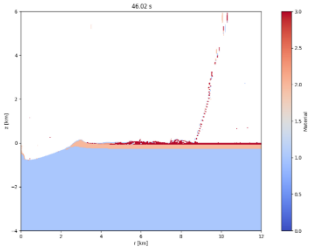
46.02 s
z [km]
r [km]
Material

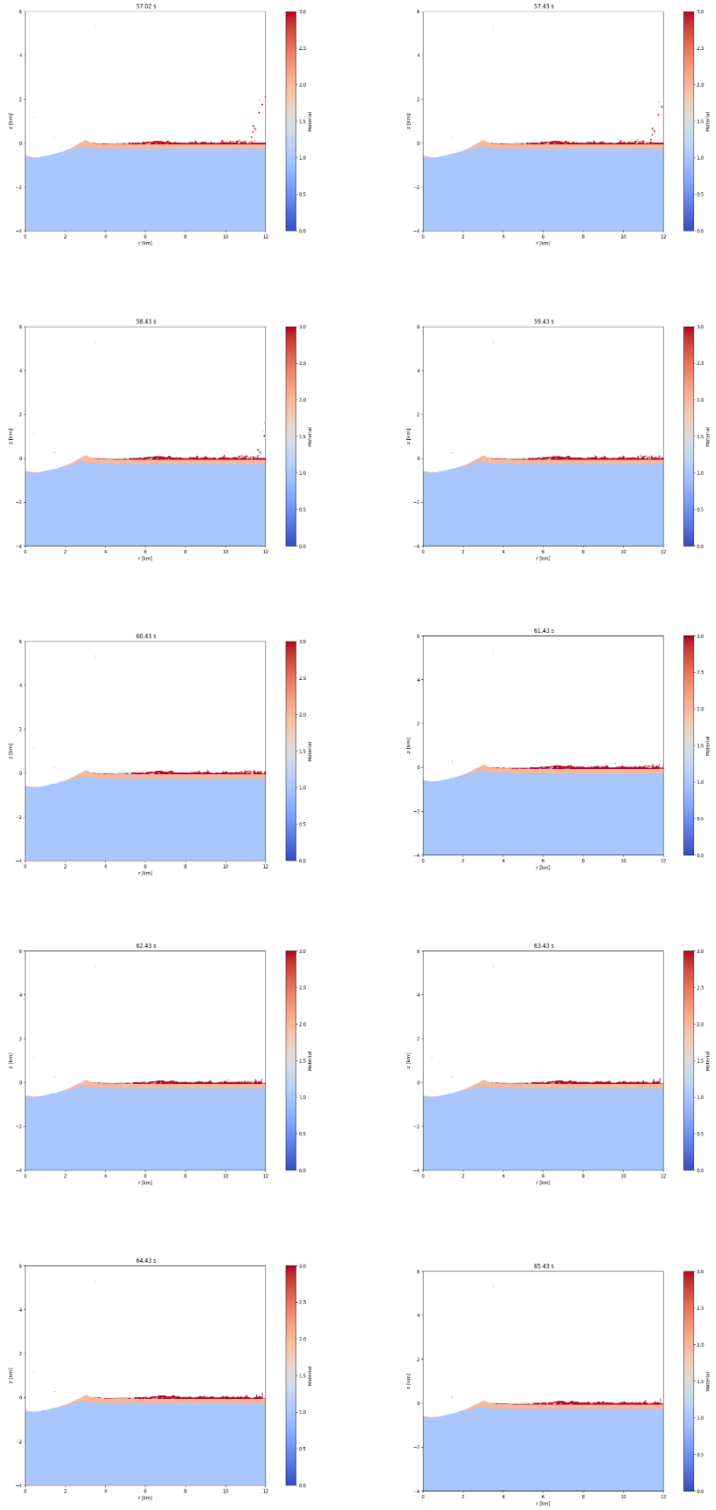
57.02 s
57.43 s
58.43 s
59.43 s
60.43 s
61.43 s
62.43 s
63.43 s
64.43 s
65.43 s

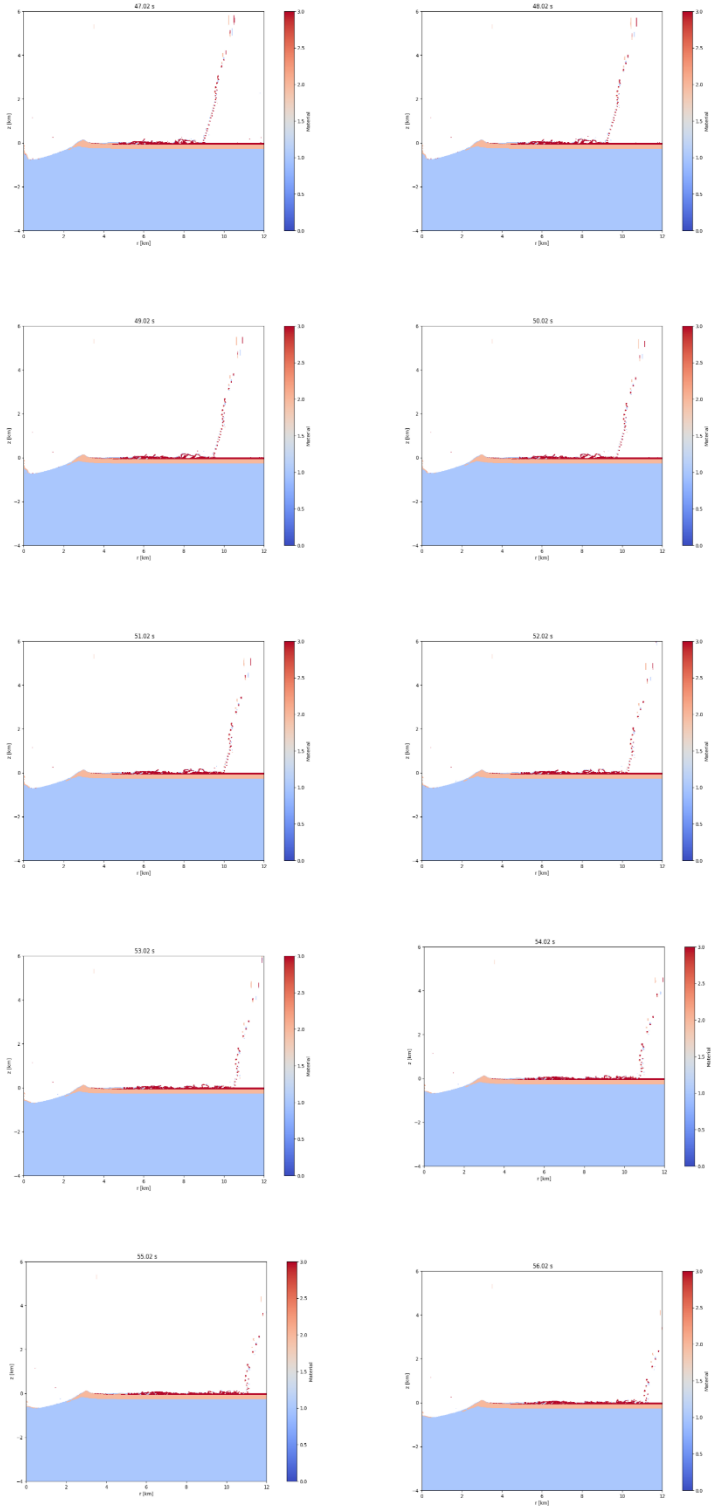
47.02 s
48.02 s
49.02 s
50.02 s
51.02 s
52.02 s
53.02 s
54.02 s
55.02 s
56.02 s

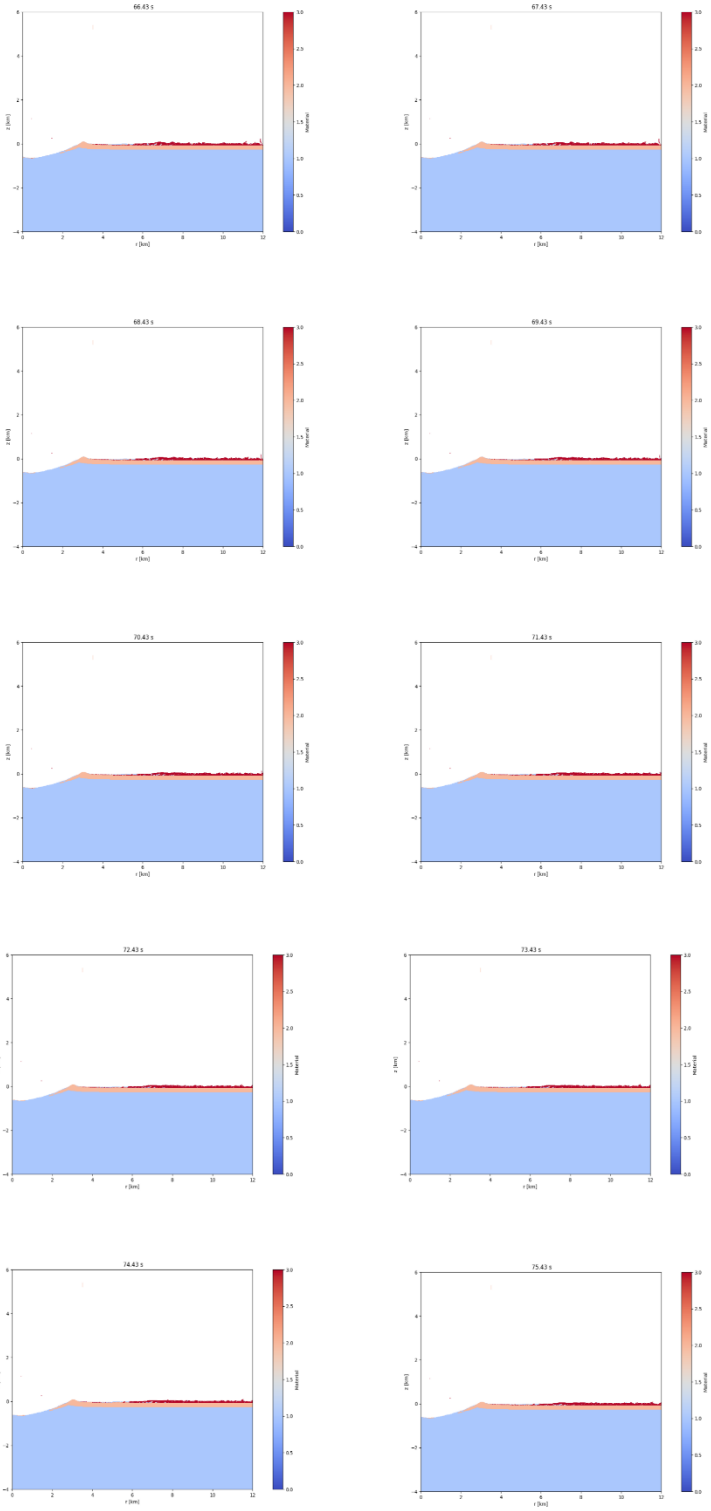
66.43 s
67.43 s
68.43 s
69.43 s
70.43 s
71.43 s
72.43 s
73.43 s
74.43 s
75.43 s
r [km]
z [km]
Material

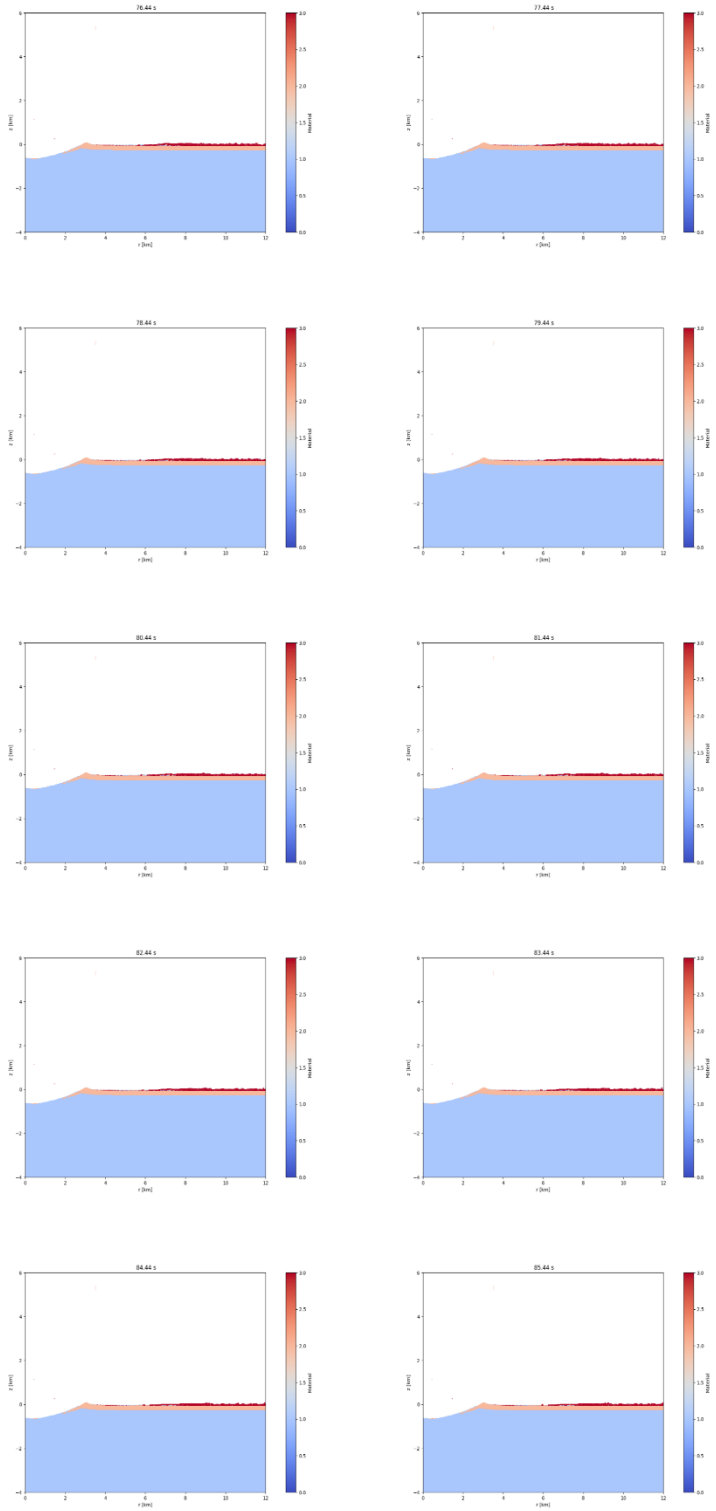
76.44 s
77.44 s
78.44 s
79.44 s
80.44 s
81.44 s
82.44 s
83.44 s
84.44 s
85.44 s

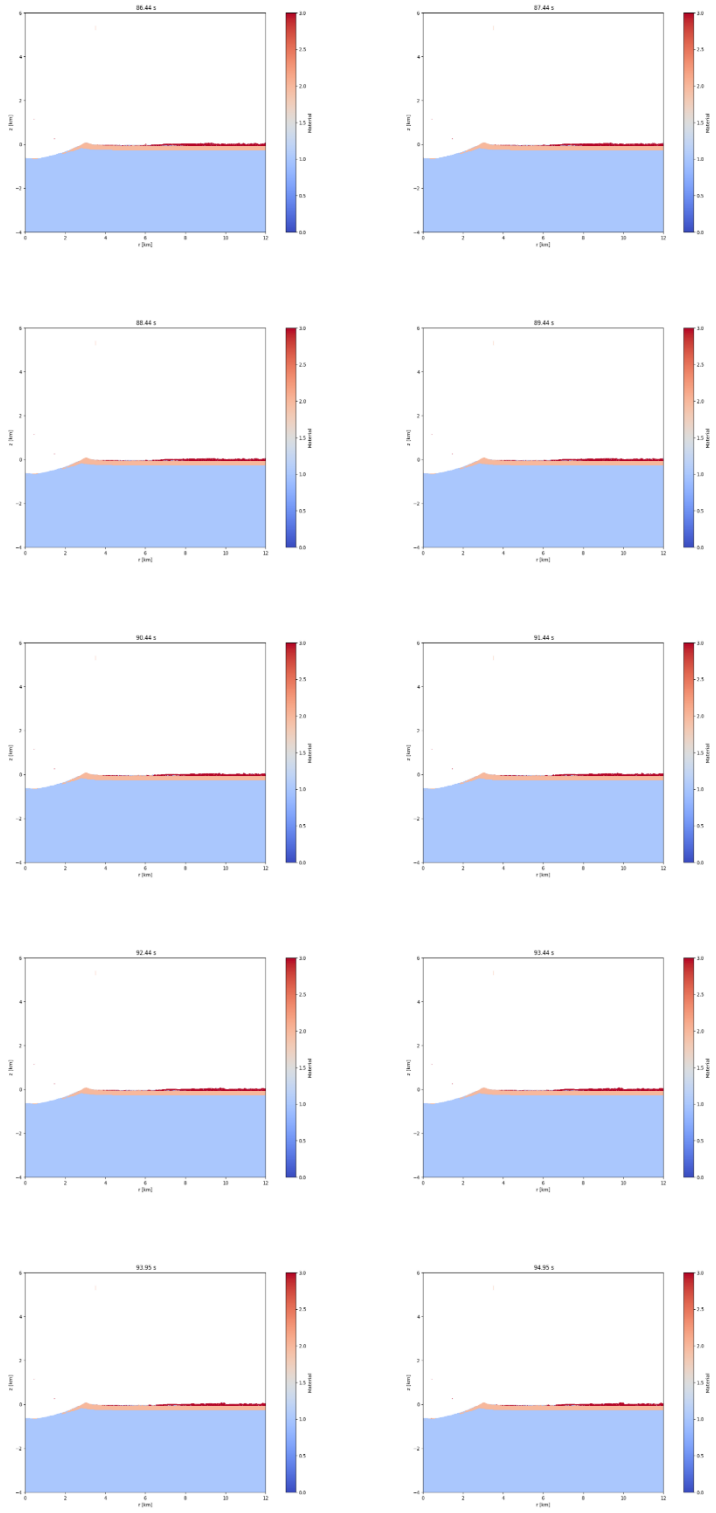
86.44 s
87.44 s
88.44 s
89.44 s
90.44 s
91.44 s
92.44 s
93.44 s
93.95 s
94.95 s

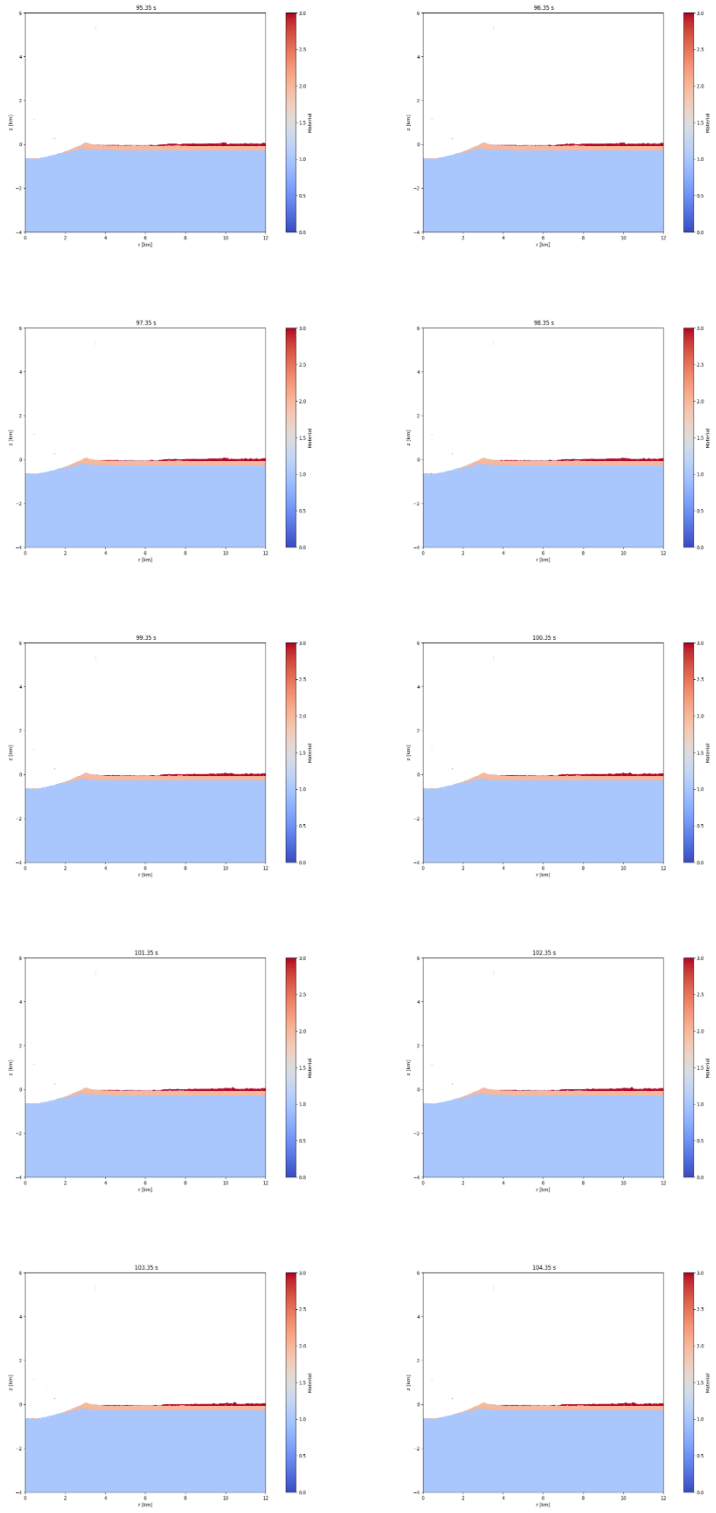
95.35 s
96.35 s
97.35 s
98.35 s
99.35 s
100.35 s
101.35 s
102.35 s
103.35 s
104.35 s

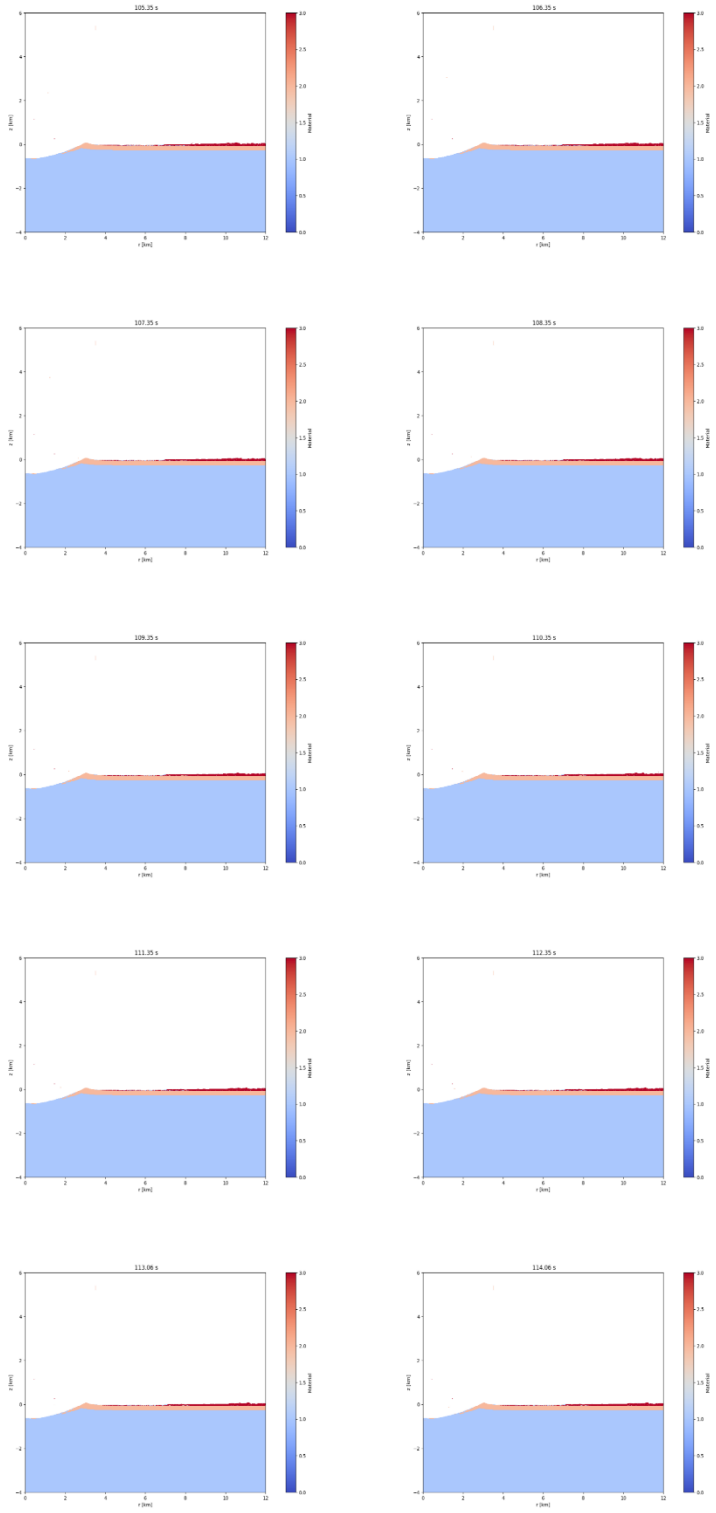
105.35 s
106.35 s
107.35 s
108.35 s
109.35 s
110.35 s
111.35 s
112.35 s
113.06 s
114.06 s

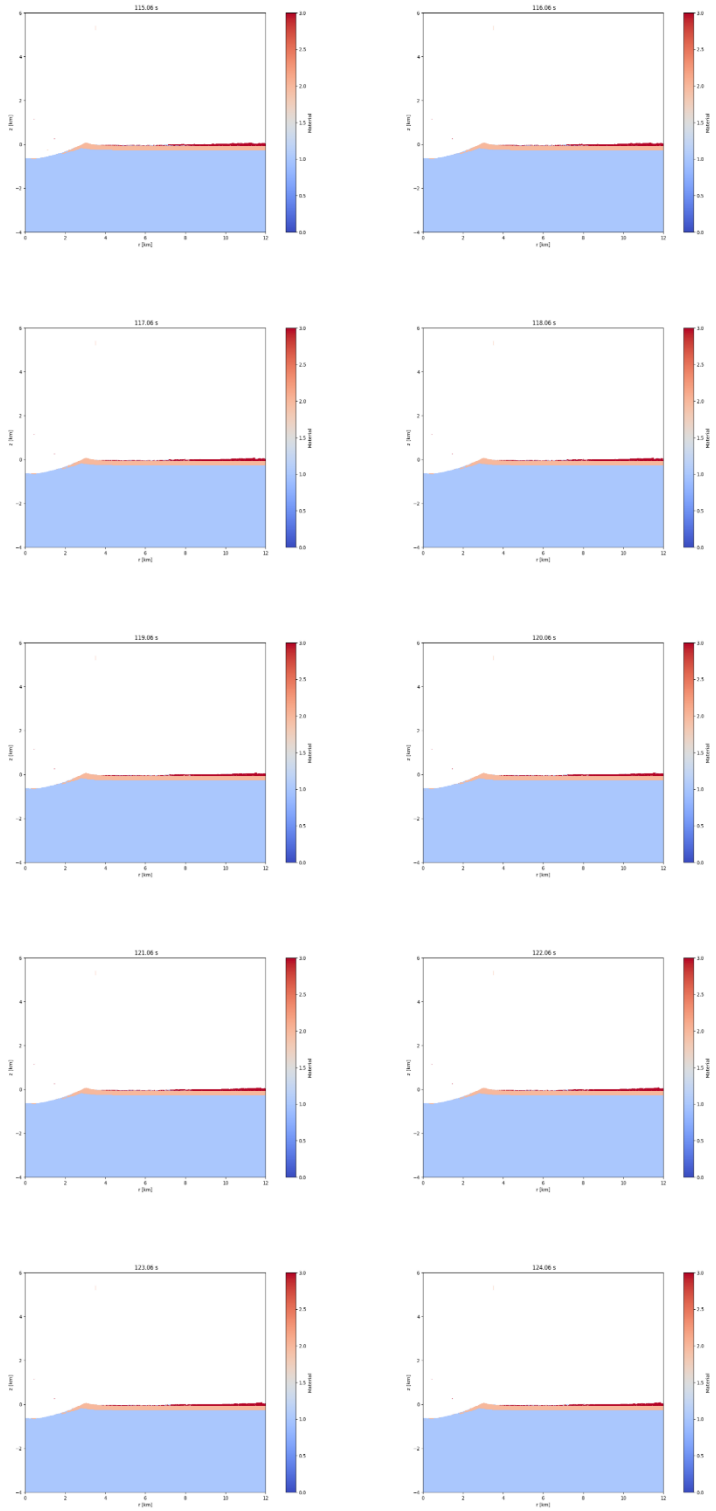
115.06 s
116.06 s
117.06 s
118.06 s
119.06 s
120.06 s
121.06 s
122.06 s
123.06 s
124.06 s

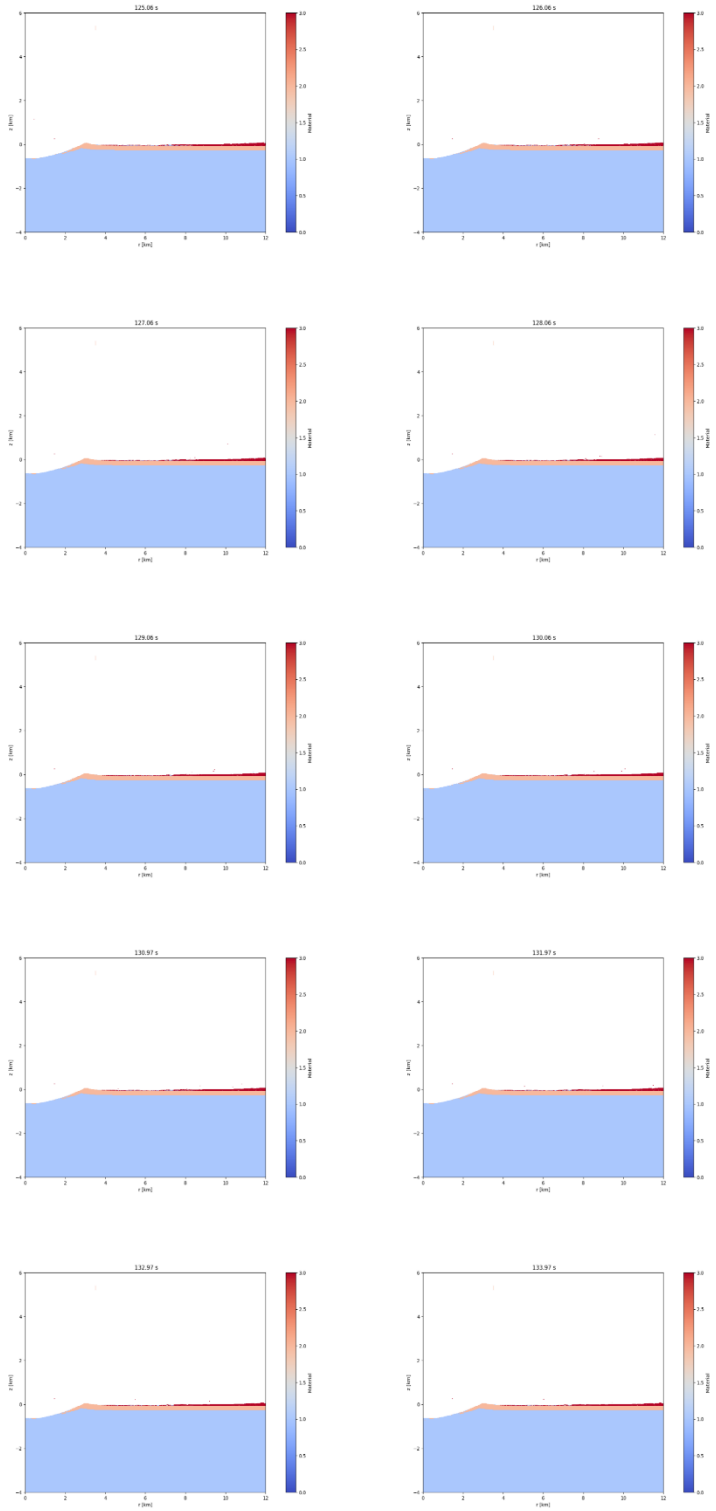
125.06 s
126.06 s
127.06 s
128.06 s
129.06 s
130.06 s
130.97 s
131.97 s
132.97 s
133.97 s

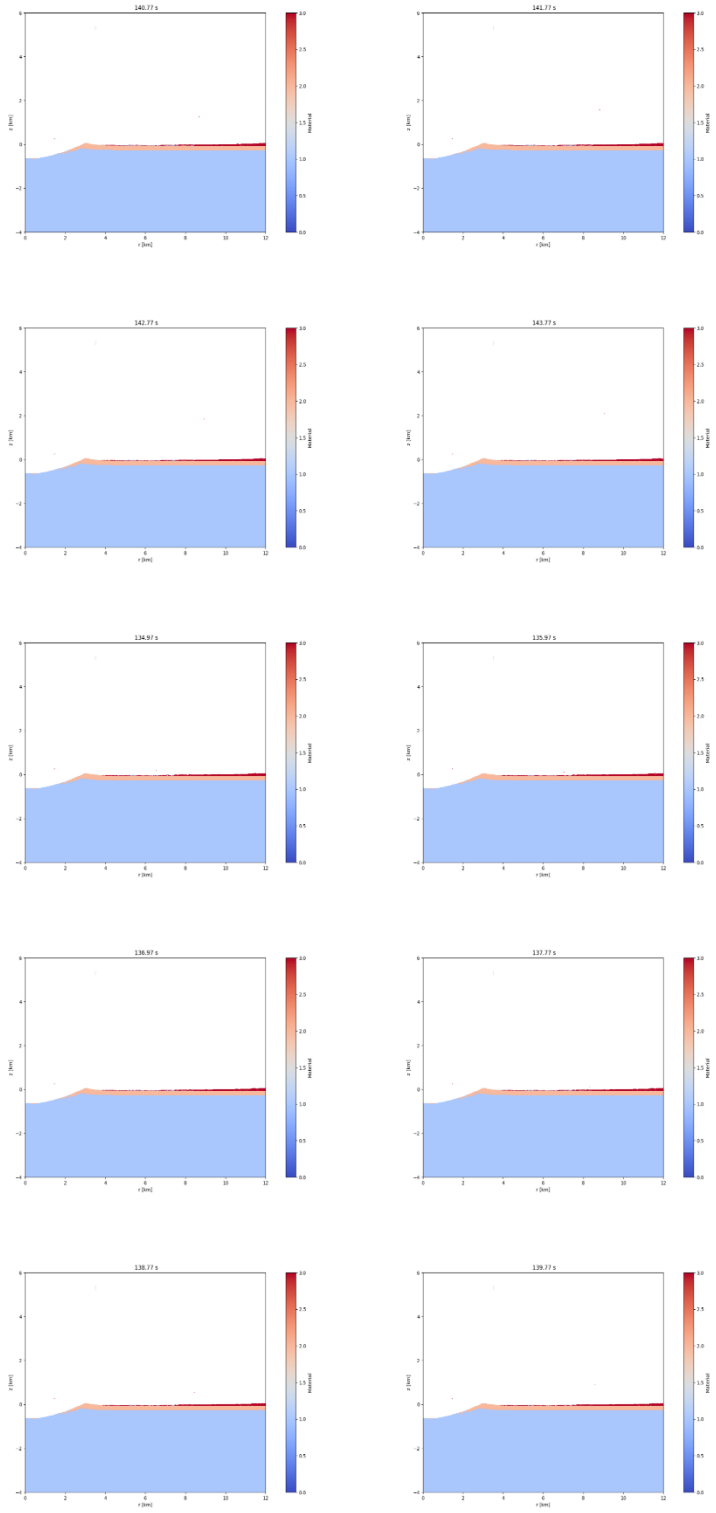
140.77 s
141.77 s
142.77 s
143.77 s
134.97 s
135.97 s
136.97 s
137.77 s
138.77 s
139.77 s

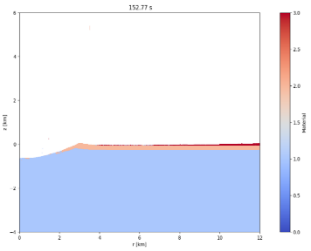
152.77 s

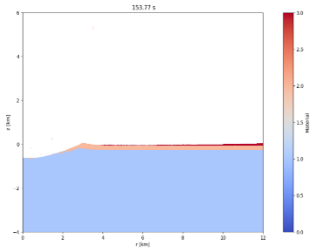
153.77 s

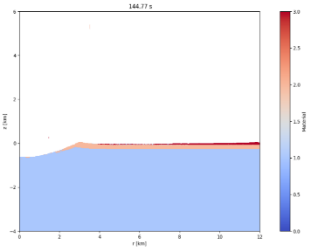
144.77 s

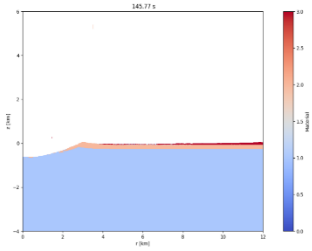
145.77 s

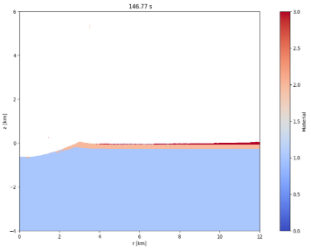
146.77 s

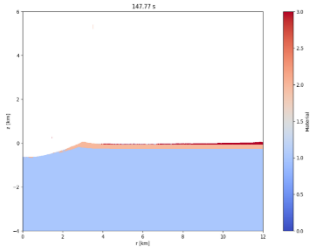
147.77 s

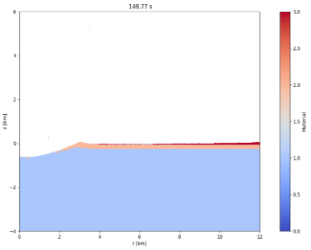
148.77 s

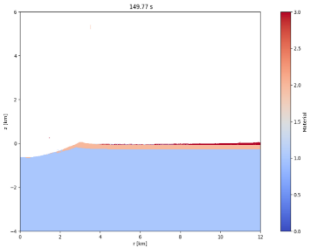
149.77 s

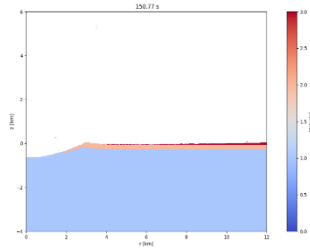
150.77 s

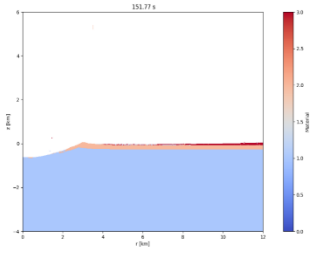
151.77 s

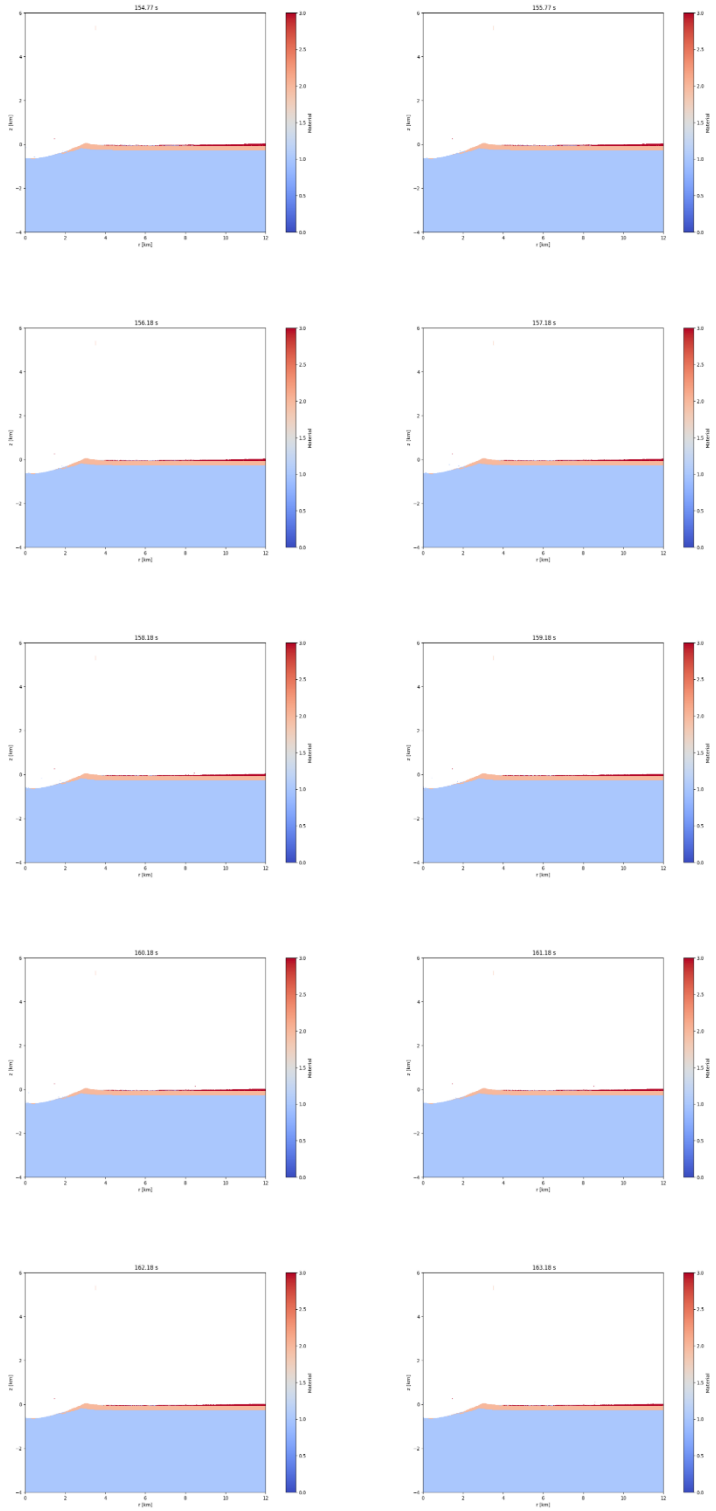
154.77 s
155.77 s
156.18 s
157.18 s
158.18 s
159.18 s
160.18 s
161.18 s
162.18 s
163.18 s

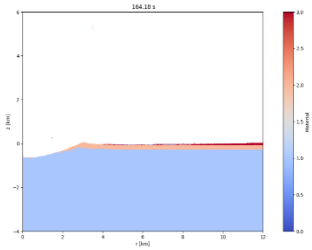
164.18 s
z [km]
r [km]
Material

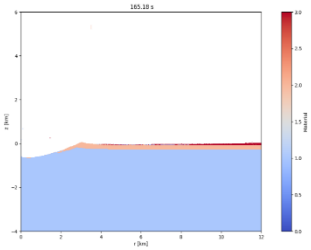
165.18 s
z [km]
r [km]
Material

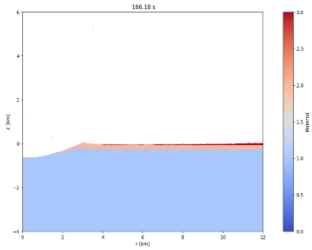
166.18 s
z [km]
r [km]
Material

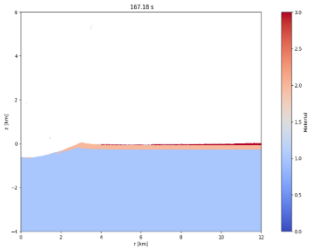
167.18 s
z [km]
r [km]
Material

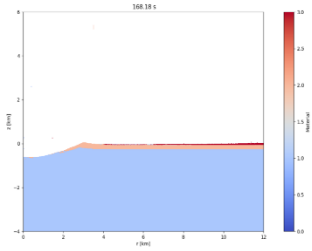
168.18 s
z [km]
r [km]
Material

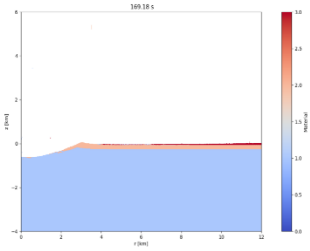
169.18 s
z [km]
r [km]
Material

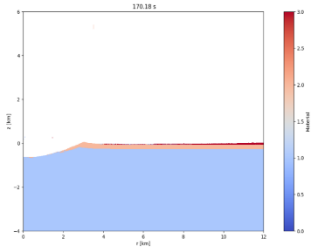
170.18 s
z [km]
r [km]
Material

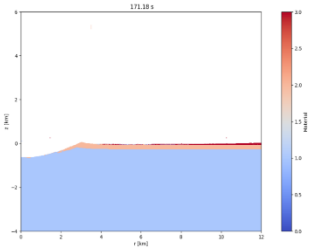
171.18 s
z [km]
r [km]
Material

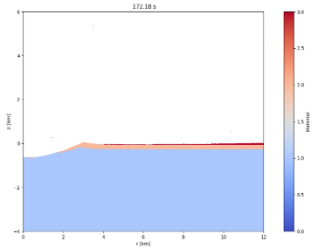
172.18 s
z [km]
r [km]
Material

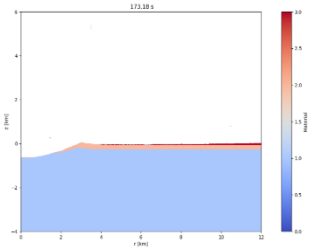
173.18 s
z [km]
r [km]
Material

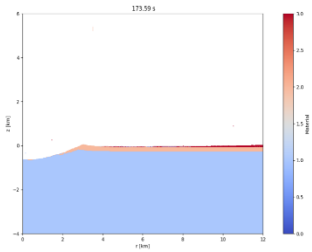
173.59 s
z [km]
r [km]
Material

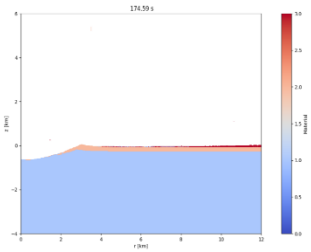
174.59 s
z [km]
r [km]
Material

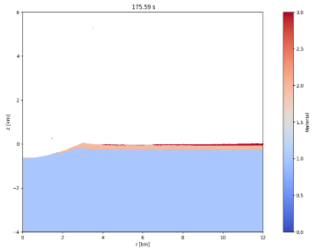
175.59 s
z [km]
r [km]
Material

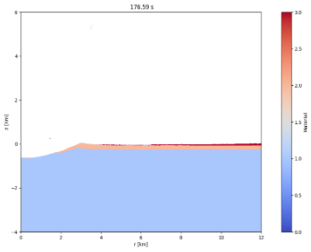
176.59 s
z [km]
r [km]
Material

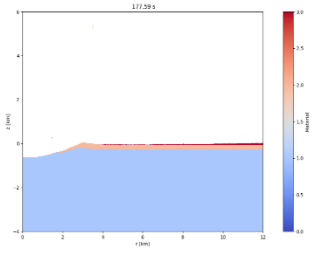
177.59 s
z [km]
r [km]
Material

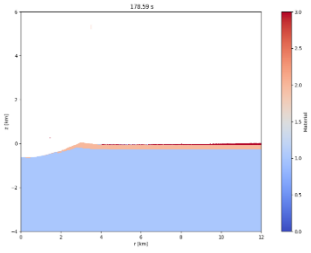
178.59 s
z [km]
r [km]
Material

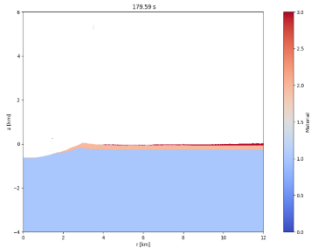
179.59 s
z [km]
r [km]
Material

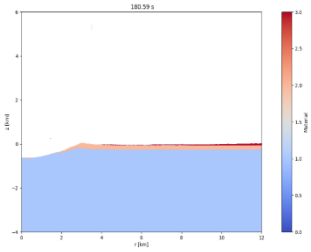
180.59 s
z [km]
r [km]
Material

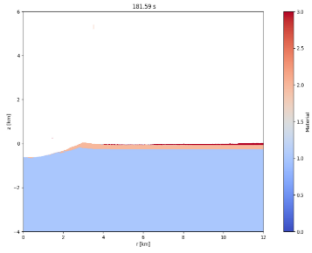
181.59 s
z [km]
r [km]
Material

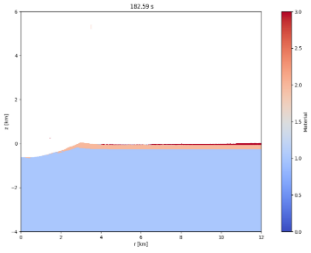
182.59 s
z [km]
r [km]
Material

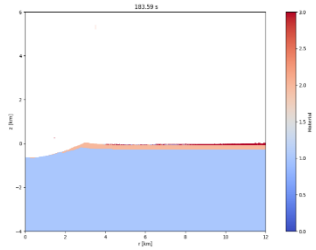
183.59 s
r [km]
z [km]
Material

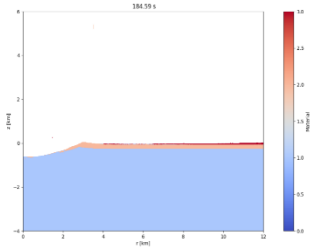
184.59 s
r [km]
z [km]
Material

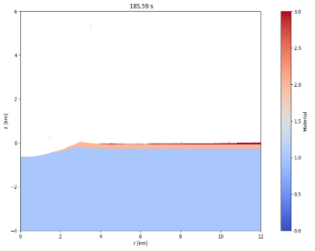
185.59 s
r [km]
z [km]
Material

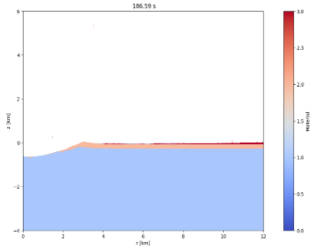
186.59 s
r [km]
z [km]
Material

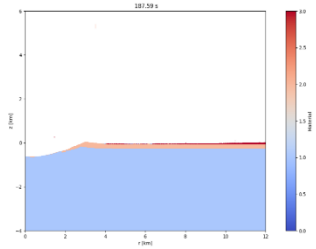
187.59 s
r [km]
z [km]
Material

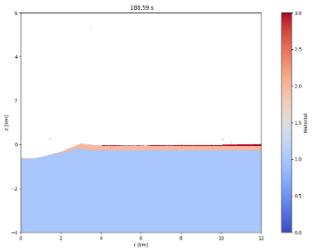
188.59 s
r [km]
z [km]
Material

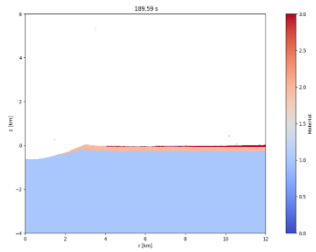
189.59 s
r [km]
z [km]
Material

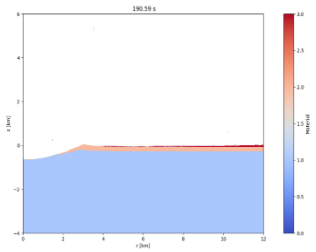
190.59 s
r [km]
z [km]
Material

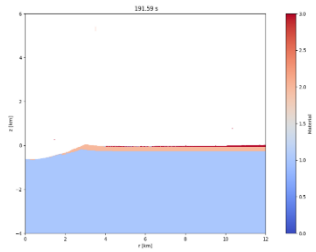
191.59 s
r [km]
z [km]
Material

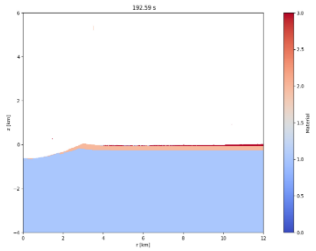
192.59 s
r [km]
z [km]
Material

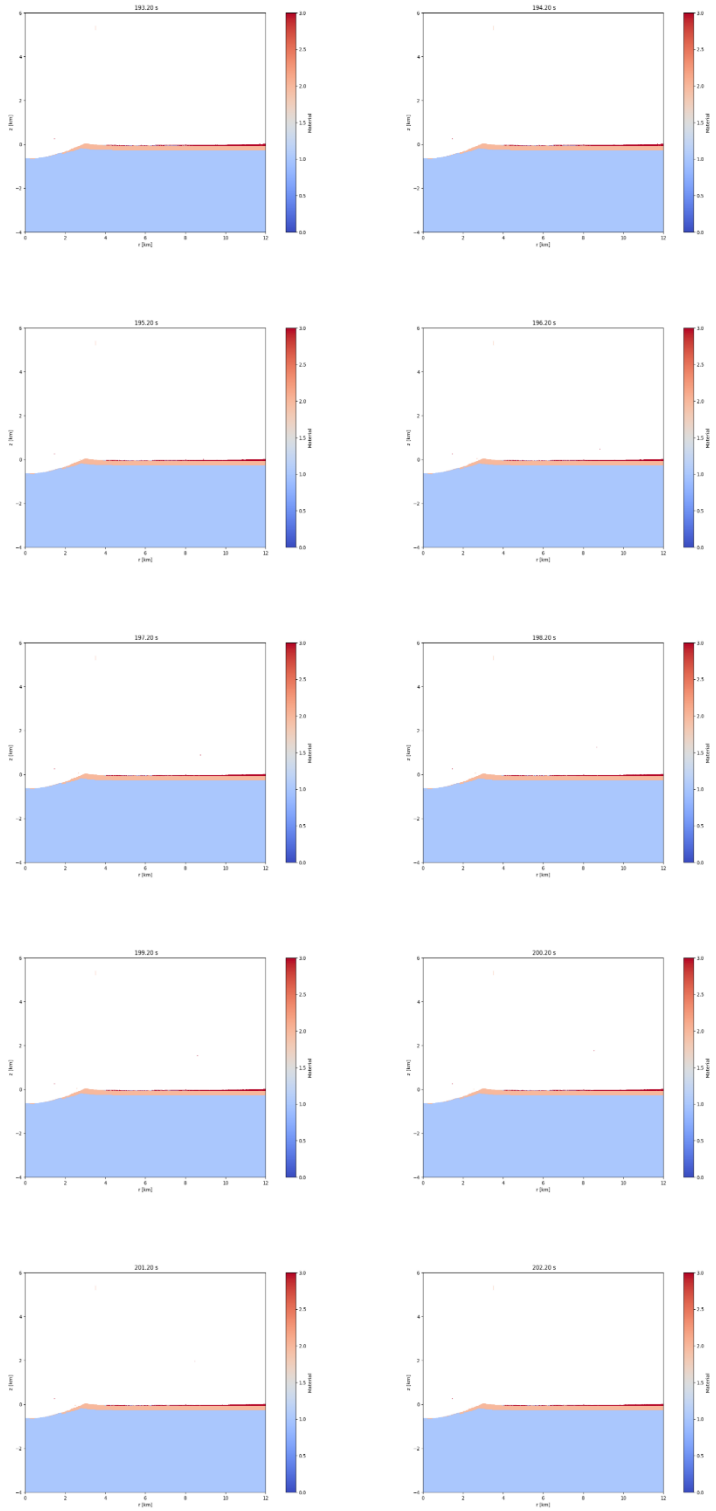
193.20 s
194.20 s
195.20 s
196.20 s
197.20 s
198.20 s
199.20 s
200.20 s
201.20 s
202.20 s

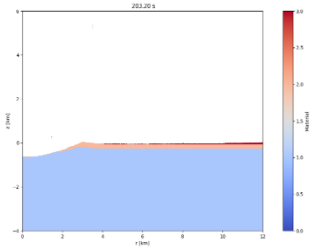
203.20 s
z [km]
r [km]
Material

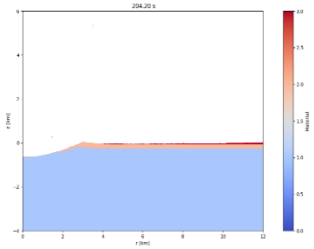
204.20 s
z [km]
r [km]
Material

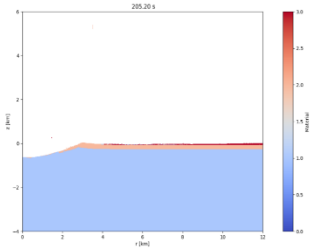
205.20 s
z [km]
r [km]
Material

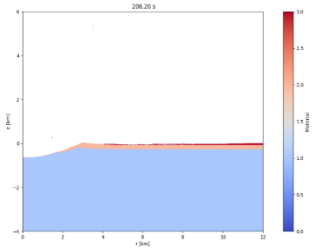
206.20 s
z [km]
r [km]
Material

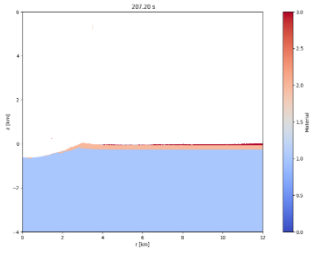
207.20 s
z [km]
r [km]
Material

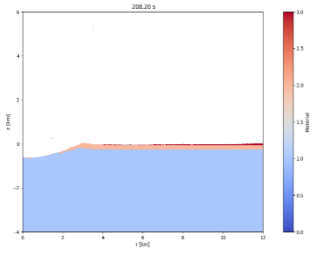
208.20 s
z [km]
r [km]
Material

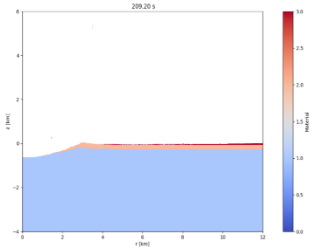
209.20 s
z [km]
r [km]
Material

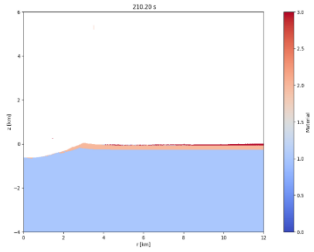
210.20 s
z [km]
r [km]
Material

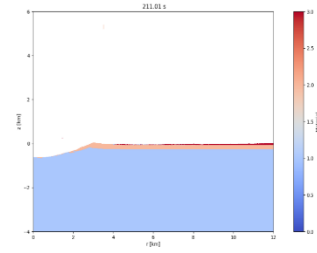
211.01 s
z [km]
r [km]
Material

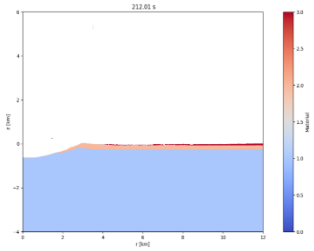
212.01 s
z [km]
r [km]
Material

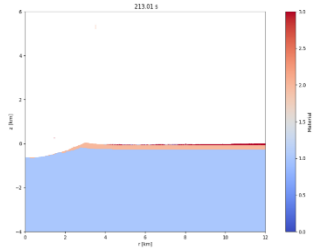
213.01 s
z [km]
r [km]
Material

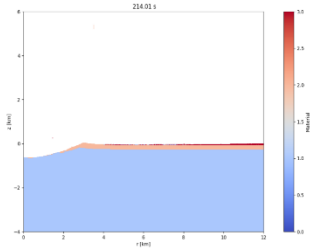
214.01 s
z [km]
r [km]
Material

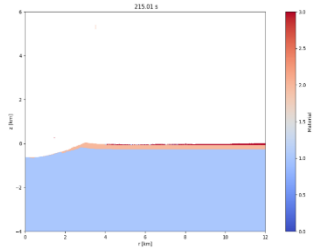
215.01 s
z [km]
r [km]
Material

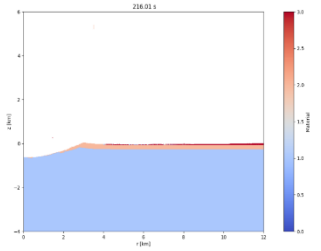
216.01 s
z [km]
r [km]
Material

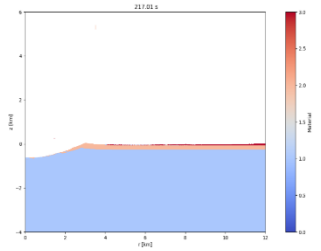
217.01 s
z [km]
r [km]
Material

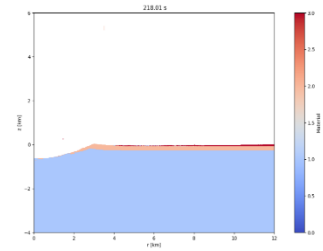
218.01 s
z [km]
r [km]
Material

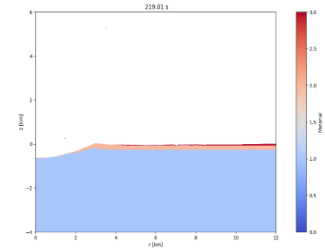
219.01 s
z [km]
r [km]
Material

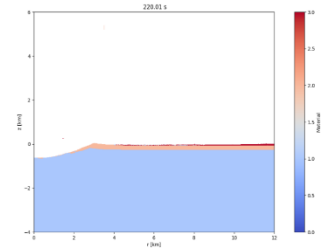
220.01 s
z [km]
r [km]
Material

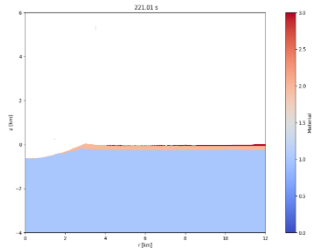
221.01 s
z [km]
r [km]
Material

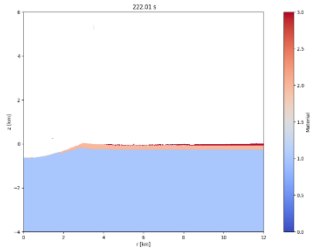
222.01 s
z [km]
r [km]
Material

2. *ROCK strength model parameters*

The rock strength model defines the yield strength Y as:

$$Y = Y_d D + Y_i(1. - D)$$

where D is a scalar measure of damage (0=intact; 1=damaged) that is computed by one of the damage models. The damaged material strength, Yd is defined by:

$$Y_d = \min\left(Y_{d0} + \mu_d p, Y_{dm}\right)$$

where p is pressure. The intact material strength, Y_i is defined by:

$$Y_i = Y_{i0} + \frac{\mu_i p}{1 + \frac{\mu_i p}{Y_{im} - Y_{i0}}}$$

The constants in these equations are defined by the iSALE input parameters below:

Constant	Input parameter	Description
Y_{i0}	YINT0	Cohesion of intact material
μ_i	FRICINT	Coefficient of internal friction for intact material
Y_{im}	YLIMINT	Limiting strength at high pressure for intact material
Y_{d0}	YDAM0	Cohesion of damaged material
μ_d	FRICDAM	Coefficient of internal friction for damaged material
Y_{dm}	YLIMDAM	Limiting strength at high pressure for damaged material

3. *Collins et al. (2004) damage model parameters*

The COLLINS damage model computes damage D resulting from both tensile and shear failure. The shear component to the damage is again a function of plastic strain:

$$D = \min(\frac{\epsilon_p}{\epsilon_f}, 1)$$

where ϵ_f , the plastic strain at failure, is computed from three piecewise linear functions of pressure:

$$\epsilon_f = \max(0.01, 0.01 + 0.04\frac{p}{p_{bd}} \qquad for\ p < p_{bd}$$

$$\epsilon_f = 0.05 + 0.05\frac{p - p_{bd}}{p_{bp} - p_{bd}} \qquad for\ p_{bd} < p < p_{bp}$$

$$\epsilon_f = 0.1 + 0.5\frac{p - p_{bp}}{p_{bp}} \qquad for\ p > p_{bp}$$

where $p_{bd}$and $p_{bp}$are the brittle-ductile and brittle-plastic transition pressures respectively. See Collins et al. (2004) for definitions of these terms. iSALE will choose these constants automatically if they are entered as -1. Alternatively, p_{bd} can be regarded as the pressure at which the failure strain is 5% and p_{bp} is the pressure at which the failure strain is 10%.

If the tensile failure model is activated (TENSILE=1), the most tensile principal elastic stress in the cell is computed and compared to the current tensile strength of the cell. The tensile strength is defined by:

$$Y = Y_{t0}(1 - D)$$

where D is the damage and Y_{t0} is the intact tensile strength.

If the tensile stress exceeds the tensile strength, the elastic stresses are reduced by the factor:

$$\frac{1 - D^n}{1 - D^{n-1}}$$

where the superscript *n* denotes the time level; i.e., D^{n-1} is the damage from the previous timestep. Tensile damage is accumulated by considering the growth of a single characteristic law in the cell, assuming that the flaw grows at the crack-growth speed c_g (m/s). The tensile damage in the cell is given formally by the equation:

$$\frac{dD^{1/3}}{dt} = \frac{c_g}{\min dx, dy}$$

where *dx* and *dy* are the cell dimensions. Note that iSALE currently assumes that the crack growth speed is 40% of the bulk sound speed in the cell, $c_g = 0.4c_B$. Hence, the only input parameter for the tensile failure model is y_{t0}.

Constant	Input parameter	Description
p_{bd}	BDTPRES	Brittle-ductile transition pressure (Pa) [-1 for auto set]
p_{bp}	BPTPRES	Brittle-plastic transition pressure (Pa) [-1 for auto set]
y_{t0}	YTENS0	Tensile strength of intact material (Pa) [positive number]

4. Porosity model parameters

The pressure p in a porous material is a function of the bulk density ρ, internal energy E, and distension α, which is the ratio of the density of the solid (matrix) material ρ_s to the bulk density ($\alpha = \rho_s/\rho$). Porosity ϕ is related to the distension by $\alpha = \frac{1}{1-\phi}$. iSALE calculates the thermodynamic state of a porous material by separating the compaction of pore space from the compression of the solid component (Herrmann, 1969). Specifically, it adopts the approach of Carroll and Holt (1972), where the pressure in the porous material is given by the pressure in the solid material P_s divided by the distension:

$$P = f(\rho, E, \alpha) = \frac{1}{\alpha} P_s(\alpha\rho, E) = \frac{1}{\alpha} P_s(\rho_s, E)$$

which Holsapple (2008) showed is thermodynamically consistent. An advantage of this formulation is that the same equation of state (tables or formulae) can be used to compute the pressure in the solid component of a porous material and the pressure in a fully-consolidated material of the same composition. The only additional requirement to compute the thermodynamic state of a porous material is to derive the distension α from another state variable—the so-called compaction function.

In contrast to previous definitions of the compaction function, where the distension was defined as a function of pressure (Herrmann, 1969; Kerley, 1992, $p - \alpha$ model,), the compaction model used in iSALE, referred to as the $\epsilon - \alpha$ model, relates the distension to volumetric strain ϵ_v (Wünnemann et al., 2006; Collins et al., 2011). The full compaction model of Wünnemann et al. (2006); Collins et al. (2011) comprises four regimes that describe the compression of a pristine

porous material up to, and beyond, its fully consolidated state: elastic compaction, exponential compaction, power-law compaction, and compression.

Elastic compaction: $0 > \epsilon > \epsilon_e \qquad \alpha = \alpha_0$

Exponential compaction: $\epsilon_e > \epsilon > \epsilon_x \qquad \alpha = \alpha_0 e^{k(\epsilon - \epsilon_e)}$

Power-law compaction: $\epsilon_x > \epsilon > \epsilon_c \qquad \alpha = 1 + (\alpha_x - 1)(\frac{\epsilon_c - \epsilon}{\epsilon_c - \epsilon_x})^2$

Compression: $\epsilon_c > \epsilon \qquad \alpha = 1$

However, rather than compute α directly from these equations, we compute the compaction rate $\frac{d\alpha}{d\epsilon}$ in each regime and then update α using the relationship:

$$\alpha_{n+1} = \alpha_n + \frac{d\alpha}{d\epsilon}\frac{d\epsilon}{dt}\Delta t$$

The main portion of the compaction function is the exponential compaction regime, which occurs for volumetric strains between ϵ_e and ϵ_x. In this regime, the rate of compaction is:

$$\frac{d\alpha}{d\epsilon_v} = k\alpha = k\alpha_0 e^{k(\epsilon_v - \epsilon_e)}$$

where α_0 is the initial porosity and k is a parameter that accounts for the different compaction behavior of different materials and types of porosity. $k = 1$ corresponds to the idealized case where all pore space is crushed out before the matrix starts to compress; $k < 1$, if matrix compression occurs concurrently with pore-space compaction. For all materials studied so far, k is very close to

1, which is indirect support for this form of the compaction function. Note that compressive strain is negative in this definition.

The exponential compaction regime transitions into the power-law compaction regime at a volumetric strain of ϵ_x and a distension of α_x . In this regime, compaction is less rapid (as a function of volume strain) than in the exponential compaction regime, and transitions smoothly into the final compression regime at the volumetric strain where all porosity is compacted out (ϵ_c). The compaction rate in the power-law compaction regime is:

$$\frac{d\alpha}{d\epsilon_v} = 2(1-\alpha_x)\frac{\epsilon_c - \epsilon_v}{(\epsilon_c - \epsilon_x)^2}$$

In the compression regime, for volume strains $\epsilon_v \leq \epsilon_c$, the distension is 1—porosity is zero—and the compaction rate is zero.

5. *The Tillotson equation of state*

Another empirical equation of state, specifically designed for high-velocity impact computations and hence suitable for a larger pressure range, was developed in 1962 by J. H. Tillotson. The equation was designed to duplicate the linear shock-particle velocity relation at low pressures and to extrapolateto the Thomas-Fermi limit at high pressures (Tillotson, 1962). This equation of state also has parameters that allow it to describe approximately the unloading of shocked material into the vapour phase.

The Tillotson equation has two different forms, depending on whether the material is compressed to higher density than its zero-pressure form or expanded to lower density. The form used in the compressed region ($\rho/\rho_0 \geq 1$) and for cold expanded states where the energy density is less than the energy of incipient vaporization, $E < E_{iv}$, is

$$P_c = \left[a + \frac{b}{(E/(E_0\eta^2) + 1)}\right]\rho E + A\mu + B\mu^2$$

where$\eta = \frac{\rho}{\rho_0}, \mu = \eta - 1$ (note the different definitions here compared to the Mie-Grüneisen equation of state) and a, b, A, B, and E_0 are the Tillotson parameters. Note also that E_0 is not the initial energy density of the substance: it is merely a parameter that is often close to the vaporization energy. The initial energy density E must actually be zero to ensure that $P = 0$ in the initial state. Note that a low-density pressure cutoff in cold expanded states for $\eta < 0.8$ to 0.95 must be applied, as discussed earlier.

The parameter a is usually chosen to equal 0.5 to give the correct high-pressure limit. Note that at high pressure and temperature the pressure tends towards aρE, and a = 0.5 is not what would be expected from the perfect gas equation of state. However, a = 0.5 has been found to fit observational data better.

The linear shock-particle velocity model, derived from observational results from shock-wave experiments, relates the shock-wave velocity U to the particle velocity u_p by:

$$U = C + Su_p$$

The two constants C and S can be expressed in terms of the Tillotson parameters by

$$C = \sqrt{A/\rho_0}$$

(A is thus equivalent to K_0) and

$$S = \frac{1}{2}[1 + \frac{B}{A} + \frac{(a+b)}{2}]$$

In the expanded state, $\eta \leq 1$, when the internal energy exceeds the energy of complete vaporization $E > E_{cv}$, the pressure is given by:

$$P_h = a\rho E + [\frac{b\rho E}{\left(\frac{E}{(E_0\eta^2)}\right) + 1)} + A\mu e^{-\beta\mu}]e^{-\alpha\mu^2}$$

where α and β are constants that control the rate of convergence of this equation to the perfect gas law.

In order to make the transition between the two regimes smooth it has been found that in the partial vaporization regime, when $\frac{\rho}{\rho_0} < 1 \; and \; E_{iv} < E < E_{cv}$, the pressure is best computed from a hybrid formula:

$$P_m = \left(\frac{E - E_{iv}}{E_{cv} - E_{iv}}\right) P_h + (\frac{E_{cv} - E}{E_{cv} - E_{iv}})P_c$$

where P_h is computed from the expanded (or hot) Tillotson equation and P_c is computed from the

compressed Tillotson equation.

With a bit of algebra, an explicit relationship for the square of the sound speed can also be derived for the Tillotson EoS. In the compressed region:

$$c_c^2 = \frac{\partial P_c}{\partial \rho} = \frac{\partial P_c}{\partial \rho}|_E + \frac{\partial P_c}{\partial E}|_\rho \frac{\partial E}{\partial \rho}|_{P_c}$$

$$\frac{\partial P_c}{\partial \rho}|_E = \frac{1}{\rho_0}(A + 2B\mu) + E(a + b\psi + \frac{2bE}{E_0\eta^2}\psi^2$$

where

$$\psi = \frac{1}{\frac{E}{E_{0\eta^2}} + 1}$$

$$\frac{\partial P_c}{\partial E}|_\rho = \rho(a + b\psi - \frac{bE}{E_0\eta^2}\psi^2$$

and

$$\frac{\partial E}{\partial \rho}|_{P_c} = \frac{P_c}{\rho^2}$$

In the expanded region:

$$c_h^2 = \frac{\partial P_h}{\partial \rho} = \frac{\partial P_h}{\partial \rho}|_E + \frac{\partial P_h}{\partial E}|_\rho + \frac{\partial E}{\partial \rho}|_{P_h}$$

$$\frac{\partial P_h}{\partial \rho}|_E = aE + bE\psi\left\{1 + 2\left(\frac{\alpha}{\mu\eta} + \frac{E}{E_0\eta^2}\psi\right)\right\} e^{-\alpha/\mu^2} + A/\rho_0\left\{1 + \frac{\mu}{\eta^2\left(\beta + 2\frac{\alpha}{\mu}\right)}\right\} e^{-\alpha/\mu^2} e^{-\beta/\mu}$$

$$\frac{\partial P_h}{\partial E}|_\rho = \rho(a + b\psi\left(1 - \frac{E}{E_0\eta^2}\psi\right))-\alpha/\mu^2$$

and

$$\frac{\partial E}{\partial \rho}|_{P_h} = \frac{P_h}{\rho^2}$$

And in the transition region:

$$c_m^2 = \frac{\partial P_m}{\partial \rho} = \frac{\partial P_m}{\partial \rho}|_E + \frac{\partial P_m}{\partial E}|_\rho + \frac{\partial E}{\partial \rho}|_{P_m}$$

$$\frac{\partial P_m}{\partial \rho}|_E = \left(\frac{E - E_{iv}}{E_{cv} - E_{iv}}\right)\frac{\partial P_h}{\partial \rho}|_E + \left(\frac{E_{cv} - E}{E_{cv} - E_{iv}}\right)\frac{\partial P_c}{\partial \rho}|_E$$

$$\frac{\partial P_m}{\partial E}|_\rho = \left(\frac{E - E_{iv}}{E_{cv} - E_{iv}}\right)\frac{\partial P_h}{\partial E}|_\rho + \left(\frac{E_{cv} - E}{E_{cv} - E_{iv}}\right)\frac{\partial P_c}{\partial E}|_\rho + \frac{P_h - P_c}{E_{cv} - E_{iv}}$$

$$\frac{\partial E}{\partial \rho}|_{P_m} = \frac{P_m}{\rho^2}$$

6. ANEOS

Modern equations of state use increasingly complex descriptions that rely on different physical approximations and equations in different domains of validity. The best known example of these equations of state is ANEOS (Thompson and Lauson, 1972; Melosh, 2007), a semi-analytical model now used in a number of shock codes, including iSALE. In ANEOS pressures, temperatures, and densities are derived from the Helmholtz free energy F and are, hence, thermodynamically consistent:

$$p = \rho^2 \frac{\partial F}{\partial \rho}$$

$$S = -\frac{\partial F}{\partial T}$$

$$E = F + TS$$

The Helmholtz free energy is separated into three additive terms: the "cold" part, F_c, which is controlled by interatomic forces only and defines the state variables along the zero-Kelvin isotherm; the "thermal" part, F_t, created by atomic/molecular vibrations and/or their thermal motion; and the "electronic" part, F_e, for the high-temperature range where ionization and electronic gas behavior dominates:

$$F = F_c(\rho) + F_t(\rho, T) + F_e(\rho, T)$$

Consequently, the pressure and specific internal energy (which are derivatives of *F*) can also be represented as sums of their cold, thermal and electronic terms:

$$p = p_c(\rho) + p_t(\rho, T) + p_e(\rho, T)$$

$$E = E_c(\rho) + E_t(\rho, T) + E_e(\rho, T)$$

The cold pressure and energy are related by:

$$p_{c=\rho^2 \frac{E_c}{\partial \rho}}$$

For pressures below about 1000 GPa, the electronic components are not very important. Explicit treatment of melt and vapor is included in ANEOS. Although clearly superior to prior analytical equations of state, the original ANEOS has several limitations, such as the treatment of gases as monoatomic species, which causes it to overestimate the liquid-vapor phase curve and critical point of most complex materials. Complex materials are still difficult to model, especially when they involve several geologically relevant solid-solid phase transitions. An updated version of ANEOS is now available as part of the iSALE package, which includes, among other things, the treatment of biand tri-atomic molecular gases (Melosh, 2007). However, it does not address the problem of different complex molecules present in the vapor phase.

Table 4.1: ANEOS-derived tables provided with iSALE,

Filename	Description	Version	Sol-Liq	Sol-Sol	Ion. model	Reference
granite	?	2000	?	?	Thomas-Fermi	Unknown
granit1	Granite no mol.; low p. phase	2000	YES	NO	Thomas-Fermi	Unknown
granit2	Granite no molecules	2000	NO	YES	Thomas-Fermi	Pierazzo et al. (1997)
dunite_	Forsterite with molecules	2000	NO	YES	Thomas-Fermi	Modified from Benz et al. (1989); see Melosh (2000)
quarzit	SiO_2 with molecules	2000	NO	YES	Thomas-Fermi	Melosh (2007)
calcite	Calcite with molecules	2000	YES	NO	Thomas-Fermi	Modified from Pierazzo et al. (1998)
basalt_	Basalt with molecules	2000	NO	YES	Thomas-Fermi	Pierazzo et al. (2005)
iron___	Iron	2000	NO	YES	Thomas-Fermi	Corrected from Thompson and Lauson (1972)
water__	Water no molecules	2000	YES	NO	Thomas-Fermi	Turtle and Pierazzo (2001)

Table 4.2: ANEOS input files provided with iSALE,

Filename	Description	Version	Sol-Liq	Sol-Sol	Ion. model	Reference
granlpp	Granite (low p. phase; no mol.)	2000	YES	NO	Saha	From Boris Ivanov
granite	Granite (without molecules)	2000	NO	YES	Saha	Updated from Pierazzo et al. (1997)
dunite_	Forsterite with molecules	2007	NO	YES	Saha	Updated from Benz et al. (1989)
quarzit	SiO_2 with molecules	2007	NO	YES	Saha	Modified from Melosh (2007)
calcite	Calcite with molecules	2000	YES	NO	Saha	Unknown; based on Pierazzo et al. (1998)
basalt_	Basalt with molecules	2007	NO	YES	Saha	Pierazzo et al. (2005)
ice____	Water ice with molecules	2007	YES	NO	Saha	Unknown; based on Turtle and Pierazzo (2001)

ANEOS input parameters for several materials of geologic interest have been developed in the recent years, but much more work is still needed. Included with iSALE are a number of equation of state tables, derived using previous versions of ANEOS, and files containing input parameters for use with the new version of ANEOS that part of the iSALE repository. Table 4.1 lists the ANEOS-derived EoS tables. Table 4.2 lists the ANEOS input files. See the option ANETABLE for how to select the appropriate equation of state table/inputs. A limitation of ANEOS is that it treats high-pressure phase transitions as a modification of only the cold part of the Helmholtz free energy (Thompson and Lauson, 1972). The low- and high-pressure phases therefore depend on temperature in the same way. This implies that the pressure at which the phase transition occurs depends only weakly on temperature, which is contrary to the observed temperature-dependence of the solid-state phase boundaries in quartzite, for example (Melosh, 2007). The nearly fixed-pressure phase transformation also prevents ANEOS from reliably locating the liquid/solid phase boundary, implying that the liquid and solid states cannot be distinguished when a high pressure phase transformation is introduced, and hence that the latent heat of melting cannot be accounted for. Since the representation of liquid/solid phase transitions in ANEOS is problematic, particularly when solid-state phase transitions exist, iSALE uses a separate equation to determine the melt temperature (solidus) as a function of pressure.

7. Gravity model

Note: The image below (Robbins et al., 2011) displays a central uplift due to previous interpretation of the crater nature. However, the current understanding of the Wetumpka crater assumes the absence of a central uplift. The figure is shown with the intention to illustrate the density variation with depth within the crater fill.

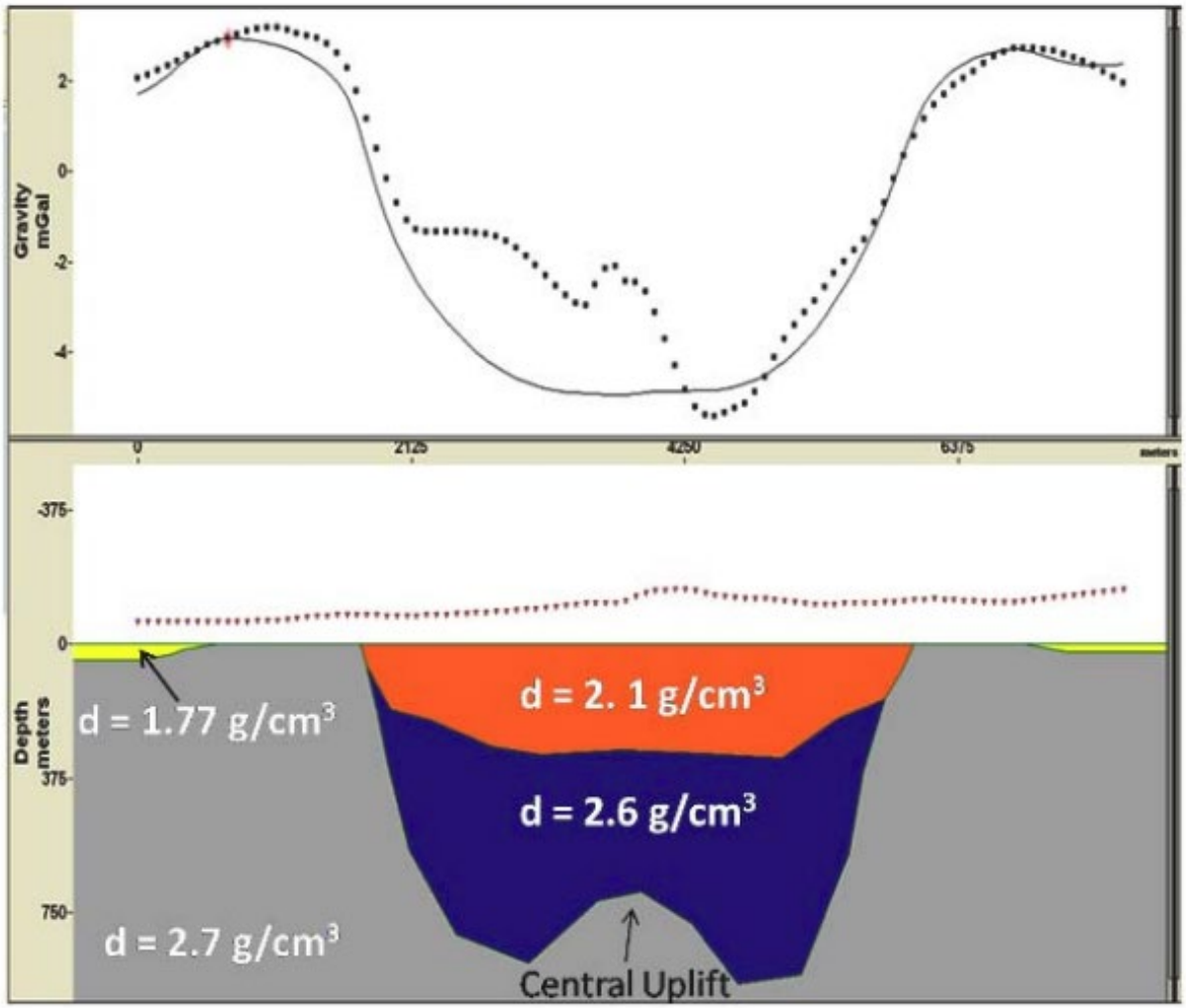

The yellow layer represents unconsolidated Quaternary sediments and Cretaceous sedimentary units. The orange unit represents slumped sedimentary target units and unconsolidated crater in-fill. The blue layer represents a brecciated unit formed within the basement rocks by the impact. The gray unit represents Piedmont rocks and continental basement. Density values representative of the lithologies are denoted. Dots indicate surface elevation. Model does not extend to the surface due to gravity corrections. Upper graph: Black dots indicate observed gravity. Black line indicates modeled gravity.

8. *Simulations*

Simulation	Time steps (seconds)	CPPR	GRDSPC	Velocity	Basement	Thickness (m)	# of cells	Strength Model	Damage model
60m	174.3	32	6.25	20	granite	2987	478	ROCK	Collins
125m	94.2	32	6.25	20	granite	2925	468	ROCK	Collins
60m_test2	152.4	32	6.25	20	granite	2987	478	ROCK	Collins
125m_test2	153.9	32	6.25	20	granite	2925	468	ROCK	Collins
60m_test3	105.5	32	6.25	20	granite	2987	478	ROCK	Collins
125m_test3	88.7	32	6.25	20	granite	2925	468	ROCK	Collins
60m_test4	154.8	32	6.25	20	granite	2987	478	ROCK	Collins
125_test4	105.8	32	6.25	20	granite	2925	468	ROCK	Collins
60m_test5	183.3	32	6.25	20	granite	2987	478	ROCK	Collins
125m_test5	160.2	32	6.25	20	granite	2925	468	ROCK	Collins
60m_test6	168.5	32	6.25	20	granite	2987	478	ROCK	Collins
125m_test6	159.3	32	6.25	20	granite	2925	468	ROCK	Collins
60m_test7	65.6	32	6.25	20	granite	2950	472	ROCK	Collins
125m_test7	51.9	32	6.25	20	granite	2888	462	ROCK	Collins
60m_test8	74.7	32	6.25	20	granite	2863	458	ROCK	Collins
125m_test8	66.8	32	6.25	20	granite	2800	448	ROCK	Collins
60m_test9	131.5	32	6.25	20	granite	2950	472	ROCK	Collins
125m_test9	145.3	32	6.25	20	granite	2950	472	ROCK	Collins
60m_test10	87.3	32	6.25	20	granite	2950	472	ROCK	Collins
125m_test10	108.6	32	6.25	20	granite	2950	472	ROCK	Collins
60m_test11	97.2	32	6.25	20	granite	2950	472	ROCK	Collins
125m_test11	90.3	32	6.25	20	granite	2950	472	ROCK	Collins
60m_test12	107.1	32	6.25	20	granite	2950	472	ROCK	Collins
125m_test12	95.2	32	6.25	20	granite	2950	472	ROCK	Collins
60m_test13	99.2	32	6.25	20	granite	2950	472	ROCK	Collins
125m_test13	82.8	32	6.25	20	granite	2950	472	ROCK	Collins
60m_test14	108.8	32	6.25	20	granite	2950	472	ROCK	Collins
125m_test14	102.7	32	6.25	20	granite	2950	472	ROCK	Collins
60m_test18	175.1	32	6.25	12	granite	2950	472	ROCK	Collins
125m_test18	174.8	32	6.25	12	granite	2950	472	ROCK	Collins
60m_test19	145.1	32	6.25	12	granite	2950	472	ROCK	Collins
125m_test19	215.6	32	6.25	12	granite	2950	472	ROCK	Collins
60m_test20	181.5	32	6.25	12	granite	2950	472	ROCK	Collins
125m_test20	160.9	32	6.25	12	granite	2950	472	ROCK	Collins
60m_test21	191.9	32	6.25	12	granite	2950	472	ROCK	Collins
125m_test21	148.1	32	6.25	12	granite	2950	472	ROCK	Collins
60m_test22	187.5	32	6.25	12	granite	2950	472	ROCK	Collins
125m_test22	239.9	32	6.25	12	granite	2950	472	ROCK	Collins
60m_test23	173.6	32	6.25	12	granite	2950	472	ROCK	Collins
125m_test23	212.7	32	6.25	12	granite	2950	472	ROCK	Collins

Damage	Sediment layer	Thickness	# of cells	Porosity	Strength Model	Damage model	Damage
0	quartzite	75	12	off	ROCK	Collins	0
0	quartzite	75	12	off	ROCK	Collins	0
0	quartzite	75	12	off	ROCK	Collins	1
0	quartzite	75	12	off	ROCK	Collins	1
0	quartzite	75	12	off	ROCK	Collins	1
0	quartzite	75	12	off	ROCK	Collins	1
0	quartzite	75	12	off	ROCK	Collins	0
0	quartzite	75	12	off	ROCK	Collins	0
0	quartzite	75	12	off	ROCK	Collins	1
0	quartzite	75	12	off	ROCK	Collins	1
0	quartzite	75	12	off	ROCK	Collins	0
0	quartzite	75	12	off	DRPR	Collins	0
0	quartzite	112.5	18	off	ROCK	Collins	1
0	quartzite	112.5	18	off	ROCK	Collins	1
0	quartzite	200	32	off	ROCK	Collins	1
0	quartzite	200	32	off	ROCK	Collins	1
0	quartzite	112.5	18	ON	ROCK	Collins	1
0	quartzite	112.5	18	ON	ROCK	Collins	1
0	quartzite	200	32	ON	ROCK	Collins	1
0	quartzite	200	32	ON	ROCK	Collins	1
0	wet tuff	112.5	18	ON	ROCK	Collins	0
0	wet tuff	112.5	18	ON	ROCK	Collins	0
0	wet tuff	200	32	ON	ROCK	Collins	0
0	wet tuff	200	32	ON	ROCK	Collins	0
0	quartzite	300	48	ON	ROCK	Collins	1
0	quartzite	300	48	ON	ROCK	Collins	1
0	wet tuff	300	48	ON	ROCK	Collins	0
0	wet tuff	300	48	ON	ROCK	Collins	0
0	quartzite	112.5	18	ON	ROCK	Collins	1
0	quartzite	112.5	18	ON	ROCK	Collins	1
0	quartzite	200	32	ON	ROCK	Collins	1
0	quartzite	200	32	ON	ROCK	Collins	1
0	quartzite	300	48	ON	ROCK	Collins	1
0	quartzite	300	48	ON	ROCK	Collins	1
0	wet tuff	112.5	18	ON	ROCK	Collins	0
0	wet tuff	112.5	18	ON	ROCK	Collins	0
0	wet tuff	200	32	ON	ROCK	Collins	0
0	wet tuff	200	32	ON	ROCK	Collins	0
0	wet tuff	300	48	ON	ROCK	Collins	0
0	wet tuff	300	48	ON	ROCK	Collins	0

Comments:
Shear parameters set 10x lower than granite/ shear damage set to -1
Shear parameters set 10x lower than granite/ shear damage set to -1
YLIMINT/YLIMDAM/YDAM All set 10 x lower than granite - Normal cohesion/ shear damage set to -1
YLIMINT/YLIMDAM/YDAM All set 10 x lower than granite - Normal cohesion/ shear damage set to -1
YLIMINT/YLIMDAM/YDAM/YINT0 All set 10 x lower than granite/ shear damage set to -1
YLIMINT/YLIMDAM/YDAM/YINT0 All set 10 x lower than granite/ shear damage set to -1
YLIMINT/YLIMDAM/YDAM/YINT0 All set 10 x lower than granite/ shear damage 10x lower than granite
YLIMINT/YLIMDAM/YDAM/YINT0 All set 10 x lower than granite/ shear damage 10x lower than granite
YLIMINT/YLIMDAM/YDAM All set 10 x lower than granite - Normal cohesion/ shear damage set to -1
YLIMINT/YLIMDAM/YDAM All set 10 x lower than granite - Normal cohesion/ shear damage set to -1
YDAM=0 (FROM WINKLER et al., 2018)/YLIMINT and YLIMDAM set to 10x lower than granite/Shear damage set to 10x lower than granite/normal cohesion
YDAM=0 (FROM WINKLER et al., 2018)/YLIMINT and YLIMDAM set to 10x lower than granite/Shear damage set to 10x lower than granite/normal cohesion
Shear damage set to 10x lower than granite / normal cohesion
Shear damage set to 10x lower than granite / normal cohesion
Shear damage set to 10x lower than granite / normal cohesion
Shear damage set to 10x lower than granite / normal cohesion
Material vS18:S38alues changed: Granite (cohesion and fric coef intact material) Quartzite (fric coeff damaged material considering 40 degrees=0.69).
Material values changed: Granite (cohesion and fric coef intact material) Quartzite (fric coeff damaged material considering 40 degrees=0.69).
Material values changed: Granite (cohesion and fric coef intact material) Quartzite (fric coeff damaged material considering 40 degrees=0.69).
Material values changed: Granite (cohesion and fric coef intact material) Quartzite (fric coeff damaged material considering 40 degrees=0.69).
Material values changed: Granite (cohesion and fric coef intact material)
Material values changed: Granite (cohesion and fric coef intact material)
Material values changed: Granite (cohesion and fric coef intact material)
Material values changed: Granite (cohesion and fric coef intact material)
Material values changed: Granite (cohesion and fric coef intact material) Quartzite (fric coeff damaged material considering 40 degrees=0.69).
Material values changed: Granite (cohesion and fric coef intact material) Quartzite (fric coeff damaged material considering 40 degrees=0.69).
Material values changed: Granite (cohesion and fric coef intact material)
Material values changed: Granite (cohesion and fric coef intact material)
Material values changed: Granite (cohesion and fric coef intact material) Quartzite (fric coeff damaged material considering 40 degrees=0.69).
Material values changed: Granite (cohesion and fric coef intact material) Quartzite (fric coeff damaged material considering 40 degrees=0.69).
Material values changed: Granite (cohesion and fric coef intact material) Quartzite (fric coeff damaged material considering 40 degrees=0.69).
Material values changed: Granite (cohesion and fric coef intact material) Quartzite (fric coeff damaged material considering 40 degrees=0.69).
Material values changed: Granite (cohesion and fric coef intact material) Quartzite (fric coeff damaged material considering 40 degrees=0.69).
Material values changed: Granite (cohesion and fric coef intact material) Quartzite (fric coeff damaged material considering 40 degrees=0.69).
Material values changed: Granite (cohesion and fric coef intact material)
Material values changed: Granite (cohesion and fric coef intact material)
Material values changed: Granite (cohesion and fric coef intact material)
Material values changed: Granite (cohesion and fric coef intact material)
Material values changed: Granite (cohesion and fric coef intact material)
Material values changed: Granite (cohesion and fric coef intact material)

9. Brazilian test compiled results

Brazilian test compiled results

Results Table 1	Specimen label	Maximum Load (N)	Yield Strength (Offset 0.2 %) (MPa)	Compressive Strength (MPa)
1	Brazilian 1	4291.82	25.11	32.48
2	Brazilian 2	5476.23	24.36	41.45
3	Brazilian 3	4933.54	23.35	39.88
4	Brazilian 4	5708.45		46.29
5	Brazilian 5	4842.23	22.31	40.1
6	Brazilian 6	4046.44	20.14	30.63
7	Brazilian 7	5203.62	25.91	41.47
8	Brazilian 8	4996.42	22.45	37.18
Mean		4937.34	23.38	38.69
Standard deviation		557.91223	1.9526	5.10394
Minimum		4046.44	20.14	30.63
Maximum		5708.45	25.91	46.29
Range		1662.01	5.77	15.67

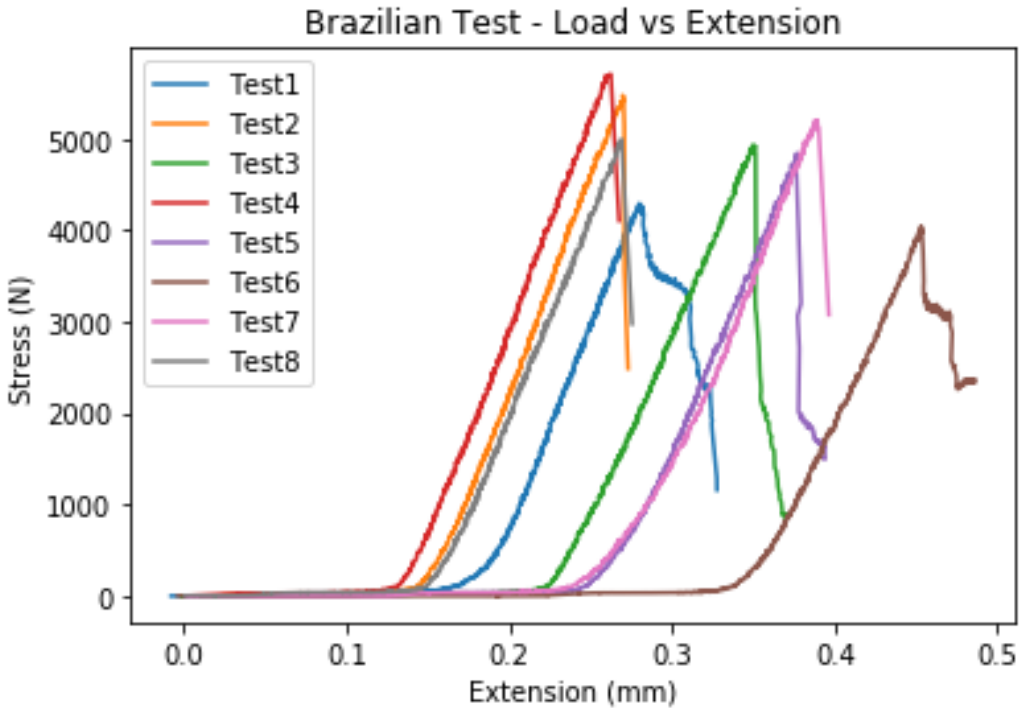

10. Compression test compiled results

Compression test compiled results

Results Table 1

	Specimen label	Maximum Load (N)	Yield Strength (Offset 0.2 %) (MPa)	Compressive Strength (MPa)
1	Compression 1	5888.1		45.19
2	Compression 2	6984.9	50.13	56.56
3	Compression 3	7531.9	60.66	61.57
4	Compression 4	7220.31	53	58.93
5	Compression 5	6368.84	48.25	51.98
6	Compression 6	5347.46	32.34	43.71
7	Compression 7	4892.76	34.83	39.68
8	Compression 8	6275.4	40.19	50.73
Mean		6313.71	45.63	51.04
Standard deviation		917.66834	10.24732	7.76009
Minimum		4892.76	32.34	39.68
Maximum		7531.9	60.66	61.57
Range		2639.14	28.31	21.89